

Copyright
by
Geoffrey Patrick Luke
2013

The Dissertation Committee for Geoffrey Patrick Luke Certifies that this is the approved version of the following dissertation:

**FUNCTIONAL AND MOLECULAR PHOTOACOUSTIC IMAGING
FOR THE DETECTION OF LYMPH NODE METASTASIS**

Committee:

Stanislav Emelianov, Supervisor

Konstantin Sokolov

Ahmed Tewfik

John Pearce

Jeffrey Myers

**FUNCTIONAL AND MOLECULAR PHOTOACOUSTIC IMAGING
FOR THE DETECTION OF LYMPH NODE METASTASIS**

by

Geoffrey Patrick Luke, B.S.C.E.; M.S.E.E.

Dissertation

Presented to the Faculty of the Graduate School of

The University of Texas at Austin

in Partial Fulfillment

of the Requirements

for the Degree of

Doctor of Philosophy

The University of Texas at Austin

December 2013

Dedication

This is for Porter. I hope that I can always set a good example and teach you that the most difficult tasks are usually the most fulfilling.

Acknowledgements

First and foremost, I would like to thank Stas and the guidance he has given me. He has always kept my best interests in mind and offered me every tool needed to succeed. He clearly values mentorship, a skill which is too often dismissed in the world of academia. In addition to Stas's instruction, I would like to acknowledge the contributions to this project by Kostia. His close collaboration and countless discussions have certainly helped to steer my research and understand the results. I would also like to thank the rest of my committee members – Professors John Pearce, Jeffrey Myers, and Ahmed Tewfik – for their insightful feedback and support throughout the entire process.

I would like to thank all the members of the Ultrasound Imaging and Therapeutics Research Laboratory for all the interesting discussions throughout my time at The University of Texas. My favorite part of earning my PhD has been the intriguing conversations that illuminated results or prompted more investigations.

Last, but certainly not least, I would like to thank my family. Kim has been more than supportive throughout this entire process. She has been understanding of the sacrifices we have both made to pursue this dream and she has encouraged me every step of the way. I would also like to acknowledge Kevin, Sarah, and my mother and father. They have always taught me to believe I can achieve whatever I put my mind to. Finally, I would like to thank Porter. Being a parent is the most difficult and rewarding thing I have had to do. In addition, Porter has been the best motivation to finish my degree in a timely manner.

FUNCTIONAL AND MOLECULAR PHOTOACOUSTIC IMAGING FOR THE DETECTION OF LYMPH NODE METASTASIS

Geoffrey Patrick Luke, Ph.D.

The University of Texas at Austin, 2013

Supervisor: Stanislav Emelianov

Accurate detection of the spread of cancer is critical for planning the best treatment strategy for a patient. Currently, an invasive sentinel lymph node biopsy is commonly used to detect metastases after a primary tumor is detected. This procedure results in patient morbidity, requires weeks of waiting, and is prone to sampling error. This dissertation presents new developments in an emerging biomedical imaging modality – photoacoustic imaging – and their application to improving the detection of metastases in the lymphatic system in a metastatic mouse model of squamous cell carcinoma of the oral cavity. Label-free spectroscopic photoacoustic imaging is demonstrated to detect hypoxia that results from the development of sub-millimeter cancer foci in the lymph node. In order to improve the sensitivity to micrometastases, molecularly-activated plasmonic nanosensors which are targeted to the epidermal growth factor receptor are introduced. The nanosensors are demonstrated to detect metastases consisting of only a few tens of cells. Improvements to spectroscopic photoacoustic imaging are then demonstrated by selecting imaging wavelengths based on the spectral properties of the optical absorbers. Finally, a new contrast agent – silica-coated gold nanoplates – are used to map the sentinel lymph node with high contrast. The final result is a set of tools that can be used to noninvasively detect micrometastases and improve molecular photoacoustic imaging.

Table of Contents

List of Figures	x
Chapter 1: Introduction	1
1.1 Molecular Imaging Modalities	3
1.1.1 Positron Emission Tomography and Single Photon Emission Computed Tomography	3
1.1.2 Magnetic Resonance Imaging	5
1.1.3 Optical Imaging	7
1.1.4 Ultrasound Imaging	9
1.1.5 Photoacoustic Imaging	11
1.1.6 A Qualitative Comparison of Biomedical Imaging Modalities ..	20
1.2 Molecular Targets in Tumors	21
1.3 Cancer Staging and Lymphatic Imaging	23
1.3.1 Cancer Staging	23
1.3.2 Sentinel Lymph Node Biopsy	23
1.3.3 Imaging of Cancer in the Lymphatics	24
1.4 Research Goals	26
1.5 References	30
Chapter 2: Label-Free Detection of Lymph Node Metastasis with Functional Spectroscopic Photoacoustic Imaging	42
2.1 Introduction	42
2.2 Materials and Methods	44
2.3 Results and Discussion	46
2.4 Conclusions	48
2.5 References	52
Chapter 3: Detection of Micrometastases with Spectroscopic Photoacoustic Imaging of Molecularly-activated Plasmonic Nanosensors	54
3.1 Introduction	54
3.2 Materials and Methods	55

3.2.1 Nanoparticle Synthesis.....	55
3.2.2 Animal Studies.....	57
3.2.3 Photoacoustic and Ultrasound Imaging.....	58
3.2.4 Statistical Analysis.....	59
3.2.5 Histology and Optical Imaging.....	60
3.3 Results and Discussion.....	60
3.4 Conclusions.....	65
3.5 References.....	72
Chapter 4: Optimization of Wavelength Selection for Spectroscopic Photoacoustic Imaging.....	76
4.1 Introduction.....	76
4.2 Materials and Methods.....	78
4.2.1 Wavelength Selection Algorithm.....	78
4.2.2 Simulations.....	80
4.2.3 Phantom Study.....	81
4.2.4 In Vivo Study.....	83
4.3 Results and Discussion.....	84
4.3.1 Simulations.....	84
4.3.2 Phantom Validation.....	87
4.3.3 <i>In vivo</i> Imaging.....	88
4.4 Conclusions.....	91
4.5 References.....	101
Chapter 5: Single-Wavelength Lymph Node Mapping with Silica-Coated Gold Nanoplates.....	104
5.1 Introduction.....	104
5.2 Materials and Methods.....	106
5.2.1 Synthesis of Silica-Coated Gold Nanoplates.....	106
5.2.2 Characterization of Silica-Coated Gold Nanoplates.....	108
5.2.3 Cytotoxicity of Si-AuNPs.....	108
5.2.4 Photothermal Stability.....	109

5.2.5 In Vivo Sentinel Lymph Node Mapping	109
5.3 Results and Discussion	110
5.3.1 Silica-Coated Gold Nanoplate Synthesis and Characterization	110
5.3.2 Cytotoxicity of Silica-Coated Gold Nanoplates	111
5.3.3 Photothermal Stability of Silica-Coated Gold Nanoplates	111
5.3.4 <i>In Vivo</i> Sentinel Lymph Node Mapping	112
5.4 Conclusions.....	114
5.5 References.....	121
Chapter 6: Conclusions and Future Outlook.....	124
6.1 Summary	124
6.2 The Impact of Molecular Imaging of Micrometastases.....	125
6.2.1 Preclinical Implications	125
6.2.2 The Clinical Future	126
6.3 Beyond Diagnostics: Image-Guided Therapy.....	127
6.4 Improved Molecular Imaging with Optimized Nanoparticle Contrast Agents	128
6.5 References.....	130
Appendix A: A Metastatic Mouse Model of Squamous Cell Carcinoma of the Oral Cavity for Photoacoustic Imaging	132
A.1 Introduction.....	132
A.2 Tumor Inoculation and growth	133
A.3 Ultrasound and Spectroscopic Photoacoustic Imaging of the Cervical Lymph Nodes.....	134
A.4 Bioluminescence Imaging.....	135
A.5 Histological Validation	136
A.6 References.....	137
References.....	138

List of Figures

- Figure 1.1 a) A block diagram of a typical photoacoustic imaging system, b) the absorption spectra of common endogenous tissue components with the optical window depicted, and c) absorption spectra of four contrast agents that span the optical window.28
- Figure 1.2 A qualitative map showing the ability of biomedical imaging modalities to provide anatomical, functional, and molecular information.....29
- Figure 1.3 A graph showing the approximate resolution and imaging depth achieved with biomedical imaging modalities.....30
- Figure 2.1 a, d, g, j, m) Combined US and sPA images showing lymph nodes from five mice (outlined in yellow) and the surrounding oxygenated (red) and deoxygenated (blue) blood, b, e, h, k, n) parametric SO_2 maps showing the level of oxygenation throughout the same two-dimensional slice (scale bar = 1 mm), and c, f, i, l, o) H&E stains of a lymph node from each mouse (scale bar = 500 μm). Images correspond to a mouse without SLN metastases (a-c), a mouse with metastasis near the SLN (d-f), and three mice with increasing spread of metastases throughout the SLN (g-i), (j-l), and (m-o).....50
- Figure 2.2 a-g) Combined US and sPA images of two-dimensional slices spanning a 2.4-mm three-dimensional volume containing a single metastatic lymph node. h-j) A parametric SO_2 map shows that lymph node is hypoxic throughout much of its volume.51

Figure 2.3 a) Lymph nodes with metastases (N = 8 nodes) exhibited statistically significant decreases in SO_2 when compared to either normal nodes (N = 17 nodes, $p = 0.0029$) or nodes with nearby metastases (N = 6 nodes, $p = 0.012$). b) A histogram of the SO_2 in the pixels in the LN of a metastatic node (red) shows a significantly different distribution than a normal node (black). c) An ROC curve shows the predictive power of lymph node SO_2 as an indicator of metastasis (red). The black dashed line corresponds to random chance. d) The lymph node SO_2 correlates negatively with metastasis size.51

Figure 3.1 (a) In each two-dimensional plane PA images are acquired using excitation wavelengths spanning 680 nm to 860 nm in steps of 20 nm. (b) Each pixel is compared to one of three optical spectra: oxygenated hemoglobin, deoxygenated hemoglobin, and activated MAPS; the dashed lines represent the expected spectra, while the colored boxes are the measured PA signals. (c) The transducer is scanned in the elevational direction to acquire a set of coregistered (d) sPA and (e) US images. Each of the slices is combined to create three dimensional (f) sPA, (g) US, and (h) combined sPA and US images. Scale bars are 1 mm.66

Figure 3.2 (a) A schematic of the EGFR-targeted MAPS; relative dimensions of antibody molecules and a gold nanoparticle (AuNPs) are preserved. (b) Hyperspectral darkfield microscopy was used to obtain optical spectra from unlabeled cells (blue), MAPS dispersed in extracellular space (green), and cells labeled with MAPS (violet). Dark-field optical images (c, d, and e; scale bar is 10 μm) and cartoon (f, g, and h) show: (c and f) cancer cells in the absence of gold nanoparticles; (d and g) cells in the presence of non-specific AuNPs; and (e and h) cells labeled with MAPS. Unlabeled cells have a characteristic bluish white appearance due to intrinsic light scattering properties (c) while a greenish haze is evident in the presence of non-specific AuNPs which strongly scatter green light (d). Molecular specific interactions between MAPS and EGFR-overexpressing cancer cells lead to receptor-mediated endocytosis which results in aggregation of the MAPS and strong changes in their optical properties (e). The colored boxes in (c-e) identify the regions from which the same-color spectral curves are displayed in (b).67

Figure 3.3 (a) Three-dimensional US image of a mouse with an overlaid cartoon of the primary tumor in the tongue and micrometastases in the cervical lymph nodes. The inset shows a two-dimensional cross section of the US image with a lymph node seen as the dark, hypoechoic oval. (b) A representative bioluminescence image confirms the presence of FaDu cells in the primary tumor and in the lymphatic system. Representative overlaid US and sPA images of: a tumor-bearing mouse with a lymph node metastasis two hours after a peritumoral injection of either (c) EGFR-targeted MAPS or (d) control RG16-conjugated AuNPs and (e) a normal mouse two hours after a submucosal injection of EGFR-targeted MAPS. Oxygenated (sPA_{HbO_2}) and deoxygenated (sPA_{Hb}) hemoglobin is depicted in red and blue, respectively, while the presence of cancer cells labeled with MAPS (sPA_{MAPS}) is depicted in yellow; anatomical location of a cervical lymph node is outlined by a dashed white line. Note, a strong sPA_{MAPS} signal in tumor-bearing mice injected with EGFR-targeted MAPS. A three-dimensional reconstruction of (f) the US images with the SLN volume segmented from the two-dimensional US images (cyan), and (g) the same image as (f) with the overlaid three-dimensional sPA image showing the volumetric distribution of sPA_{Hb} , sPA_{HbO_2} , and sPA_{MAPS} signals. All scale bars are 1 mm.....68

- Figure 3.4 Statistical analysis of sPA imaging. The LNs were split into three categories for analysis: 1) LNs containing metastases in mice injected with EGFR-targeted MAPS (n = 7), 2) LNs in mice injected with RG16-conjugated AuNPs (n = 7), and 3) LNs without metastasis in mice with or without a primary tumor injected with EGFR-targeted MAPS (n = 8). The metastatic lymph nodes in tumor-bearing mice exhibit a statistically significant increase in the sPA_{MAPS} signal.69
- Figure 3.5 Combined US and sPA image of a two-dimensional cross section containing two lymph nodes (center), and 4x enlarged sPA images of a region on the border of the left lymph node (left) and right lymph node (right) (a) before, (b) 25, (c) 45, (d) 65, (e) 85, (f) 105, and (g) 125 minutes after the injection of MAPS. The steadily growing region of activated MAPS in the right lymph node indicates that MAPS are gradually being delivered to and are interacting with cancer cells on the border of the lymph node. Scale bars are 1 mm.70
- Figure 3.6 (a,b) H&E staining of lymph nodes from mice with positive bioluminescent signal in lymph nodes shows the subcapsular formation of micrometastases near an afferent lymph vessel. (c) The morphology of a lymph node from a normal mouse is shown for reference. (d,e) At high magnification, the irregular shape and large nuclei indicate presence of cancer cells in H&E sections. (f) A normal population of lymphatic cells is seen in normal mice. Immunohistochemical staining shows (g-h) elevated expression of EGFR in the micrometastases and (i) negligible EGFR expression in normal nodes. Scale bars are 50 μ m.71

- Figure 4.1 a) Representative constructed optical absorption spectra used for algorithm analysis before (solid lines) and after (dashed lines) 50% wavelength-dependent attenuation, and b) a typical attenuation curve with relative changes in laser fluence ranging from 0% to 100%. ...92
- Figure 4.2 a,b) Photographs showing the imaging phantom consisting of pipettes containing ICG dye and silica-coated gold nanorods embedded in a gelatin phantom, c) a representative PA image acquired at 880 nm, d) the same image as in c) with the location of the pipette (dashed circle) and the region of interest used for further analysis (white box) indicated, e) the PA spectra of ICG and silica-coated gold nanorods which were used for spectral unmixing in this experiment, f) PA images of the region of interest of each pipette acquired with an excitation wavelength of 880 nm, and g) the spectrally unmixed sPA images of the same region of interest using PA images from all 146 optical wavelengths. Scale bars are 1 mm.93
- Figure 4.3 a) A three-dimensional ultrasound image of a mouse depicting the dye injection site and imaging plane (red box) and b) overlaid ultrasound and sPA image showing oxyhemoglobin and deoxyhemoglobin (red and blue, respectively) and MMPSense dye (green).94
- Figure 4.4 a) A scatter plot showing an inverse correlation between σ_{\min} and the RMS error in the concentration estimation, and b) a comparison between three wavelength selection strategies shows the developed algorithm performs significantly better.95

Figure 4.5 a) The average shift in the selected wavelengths after the absorption spectra have been distorted by wavelength-dependent attenuation, and b) a scatter plot of the error in the concentration estimation resulting from these changes in attenuation in the absence of noise.96

Figure 4.6 a) The relative concentrations of ICG and silica-coated gold nanorods can be accurately estimated from PA images acquired at wavelengths selected by the developed algorithm even when as few as 2 wavelengths are used (solid line). Adding a 3-mm layer of attenuating gelatin leads to a slight over-estimation of the nanorods concentration (dashed line). b) When evenly-spaced wavelengths are used, the concentration estimate becomes unstable when a small number of wavelengths are used (solid line), and this effect becomes more pronounced when the attenuating layer is added (dashed line). c) The developed algorithm (blue lines) produces much more reliable estimates of concentration than even spacing (black lines) in all inclusions. The 0% and 100% lines act as controls since the absorption spectra were derived from these signals.97

Figure 4.7 Plot demonstrating that σ_{\min} decreases as wavelengths are removed. This decrease is much less drastic and much more predictable when σ_{\min} selection is used (solid line) than when evenly spaced wavelengths are used (dashed line).98

Figure 4.8 The RMS error of the absorber concentrations estimated from between 3 and 30 wavelengths. The wavelengths were selected using either even spacing (dashed line) or σ_{\min} selection (solid line).....98

Figure 4.9	a) The spectra of the three absorbers with the three selected wavelengths using even spacing (triangles) and σ_{\min} selection (circles), and the sPA images generated from the evenly spaced wavelengths and from the σ_{\min} -selected wavelengths. Scale bars = 1 mm.	99
Figure 4.10	a) The spectra of the three absorbers with the six selected wavelengths using even spacing (triangles) and σ_{\min} selection (circles), and the sPA images generated from the evenly spaced wavelengths and from the σ_{\min} -selected wavelengths. Scale bars = 1 mm.	100
Figure 5.1	a) Experimental setup to study the stability of AuNPs and Si-AuNPs, and b) experimental setup for in vivo studies. The pulsed laser induces localized heating near the Si-AuNPs which results in the generation of acoustic waves centered at the Si-AuNPs (b, inset).....	115
Figure 5.2	a) Schematic showing the synthesis of Si-AuNPs. b) UV-Vis-NIR spectra of NPs before (green) and after silica coating (black). c) A TEM image of AuNPs shows an even size distribution (scale bar = 200 nm). d) A TEM image of Si-AuNPs (scale bar = 100 nm).	116
Figure 5.3	An MTS assay shows no significant cytotoxicity of Si-AuNPs at concentrations with optical extinction coefficients up to 20 cm ⁻¹ in comparison to control.	117
Figure 5.4	UV-Vis-NIR spectra showing the degradation of PEGylated AuNPs and Si-AuNPs to a,b) pulsed laser irradiation at 10 mJ/cm ² and c,d) continuous wave laser irradiation at 1.3 W/cm ² . The pulsed laser caused significant changes in the morphology of PEGylated AuNPs (a, inset) while Si-NPs with a 20-nm layer of silica showed few changes in shape (b, inset). Scale bars = 100 nm.....	118

Figure 5.5	<p>a) Overlaid USPA images of a 2-D slice containing the SLN before the injection of Si-AuNPs. The endogenous PA signal is below the noise floor of the system. b) A US image 4 hours after the injection of Si-AuNPs with the SLN identified. c) The same US image as in b) with the PA image overlaid shows a strong PA signal throughout the SLN. d) A 3-D US image with a quadrant removed shows the anatomy surrounding the SLN. e) A 3-D PA image acquired 4 hours after the injection of Si-AuNPs overlaid on the US image shows the distribution of Si-AuNPs in the SLN and reveals an afferent lymph vessel (arrow). Scale bars = 1 mm.</p>	119
Figure 5.6	<p>a-d) Combined USPA images of a 2-D slice immediately following the injection of Si-AuNPs. After being quickly delivered to the SLN, the signal slowly spreads throughout the node. e) the average PA signal (black) and volume of the lymph node that contained detectable PA signal (blue) in the SLN increase steadily over the course of 165 minutes after the injection. Scale bars = 1 mm.</p>	120
Figure 6.1	<p>A combined US/PA image of a mouse with EGFR-targeted CuS nanoparticles in the lymph node before (a) and after (b) 2 minutes of exposure to 1064 nm continuous wave laser irradiation. The PA signal in the lymph node (c) increases as the temperature rises.</p>	129
Figure 6.2	<p>The error in unmixing a contrast agent from blood depends on the spectrum of the contrast agent. A peak absorption near 800 nm is best for the given spectral range.</p>	130

Chapter 1: Introduction

At the turn of the twenty-first century, over one hundred years of cancer research had yielded very little understanding of the insidious disease. The limited knowledge of the underlying mechanisms of the formation and spread of tumors led to primitive and largely ineffective treatment strategies in which quickly-dividing cells are indiscriminately killed or large sections of the tissue surrounding a tumor is surgically removed. While early successes in limited cases (i.e., childhood leukemia) were promising for these radical therapies, oncologists were unable to generalize these results to many other types of cancer.

In the 1990s, scientists focused on creating a biological understanding of tumorigenesis. The decade culminated with the publication of a seminal review paper by Douglas Hanahan and Robert Weinberg, “The Hallmarks of Cancer.”¹ In this paper, the authors argue that a malignant tumor develops only after a series of mutations have led to a specific set of six characteristics: 1) self-sufficiency in growth signals, 2) insensitivity to anti-growth signals, 3) ability to invade tissue and metastasize, 4) limitless replicative potential, 5) sustained angiogenesis, and 6) the ability to evade apoptosis. In 2011, Hanahan and Weinberg published a follow up to “The Hallmarks of Cancer.” In it, they identify four additional characteristics that cancer cells exhibit: 7) ability to reprogram cellular metabolism, 8) avoidance of immune destruction, 9) instability in the genome, and 10) ability to induce an inflammatory response.² Despite the dozens of types of cancer and innumerable mutations which cells can undergo, this short list of phenotypes has given scientists a toolbox to analyze signaling pathways, design new therapeutics, and develop criteria for accurate diagnosis.

In the thirteen years since Hanahan and Weinberg published their seminal review, our understanding – and treatment – of cancer has increasingly focused on the gene mutations and molecular expressions that lead to the uncontrolled growth of tumor cells. This has initiated a break from the old paradigm in which increasingly severe treatments and drug mixtures take cancer patients to the brink of death in hopes of destroying all malignant cells. While the transition has been slow, it is becoming apparent that an individualized approach needs to be taken to make significant advances in the treatment and maintenance of cancer.

Biomedical imaging has adapted in conjunction with the individualized treatment approach. This is evidenced by the emergence of molecular imaging. Molecular imaging seeks to noninvasively identify the molecular expressions that are relevant to diagnosis and treatment of disease.³ A variety of imaging modalities have been used to visualize molecular expressions, measure important physiological parameters, and identify therapeutic targets, including optical imaging,⁴ positron emission tomography (PET),⁵ ultrasound (US) imaging,⁶ and photoacoustic (PA) imaging.⁷ The end goal of molecular imaging of cancer is to noninvasively detect and fully characterize a tumor, to allow a physician to chart the best course of treatment, and to visualize the tumor's response to therapy. While scientists and engineers have made steady progress towards this goal, there are many limitations to existing imaging technologies which need to be overcome. This chapter focuses on the current state of the art and provides a perspective on the future of molecular imaging in cancer with an emphasis on imaging of the lymphatic system.

1.1 MOLECULAR IMAGING MODALITIES

Biomedical imaging modalities are capable of generating images that span three broad categories: 1) anatomical, 2) functional, and 3) molecular. Anatomical images provide a window beneath the skin's surface. Contrast is driven by the physical properties of the tissue (e.g., density or amount of water in the tissue). Anatomical images are particularly useful for observing changes in or damage to tissues, identifying tissue boundaries, or providing context to functional and molecular images. Functional images give insight into the behavior of the tissue. As the name implies, it seeks to determine whether or not the tissue is functioning normally. For example, by observing blood oxygenation in a tumor, the likelihood of metastasis can be predicted.⁸ Finally, molecular imaging allows us to observe the protein expressions that drive cellular behavior. It helps answer the question of how or why a tumor has developed. Furthermore, it can be used to identify molecular targets for therapy.³

The following sections explain in detail the physics of the predominant molecular imaging modalities. In addition, contrast agents (which are necessary for molecular specificity) will be discussed. Because the bulk of this dissertation is focused on the improvement and application of photoacoustic (PA) imaging, a more in-depth discussion of the modality will be presented.

1.1.1 Positron Emission Tomography and Single Photon Emission Computed Tomography

Positron emission tomography³ and single photon emission computed tomography (SPECT) are collectively known as nuclear imaging techniques. They each rely on the injection of a radioactive compound and passive sensing of the emitted gamma rays. By sensing the gamma rays at multiple locations around the body, the source of the emissions can be localized.

Physics and Image Formation

In PET imaging, a radionuclide which is injected into the bloodstream undergoes positron emission decay.⁵ Upon interaction with an electron, the positron is annihilated and a pair of gamma rays (each traveling opposite directions) are emitted. The gamma rays are detected with photomultiplier tubes (PMTs) arranged in a cylinder and timing circuitry is used to discard single photons. The origin of the emission can be assumed to have occurred somewhere on the line between the two detecting PMTs. Once enough gamma rays are recorded, a map of the annihilation events can be obtained by applying a statistical reconstruction algorithm.⁹

Single photon emission computed tomography, on the other hand, only senses one photon at a time. This is because the contrast agents directly emit gamma rays instead of relying on positrons annihilation. A gamma camera collects the incident photons and is rotated about the body to obtain a tomographic dataset. Similar computed tomography approaches are used to reconstruct the volumetric distribution of the radionuclide.¹⁰

The wavelength of the emitted gamma rays is in the picometer range, suggesting that PET and SPECT would exhibit extremely high resolution. However, limitations in the safe dose of the radioactive concentrations degrade the resolution in practice. Because relatively few gamma rays are emitted during imaging, large detectors are used to improve sensitivity. This leads to resolution on the order of 1-10 mm.

Contrast Agents

The contrast agents for PET imaging require a cyclotron for synthesis and have a relatively short half-life. This restricts the use of PET to regions with relatively large populations. Fluorodeoxyglucose (FDG) is the most common contrast agent for PET.¹¹ The molecule acts as an analog for glucose; however, it cannot be fully metabolized by cells. Therefore it tends to accumulate in cells with high metabolism, especially those

undergoing glycolysis instead of oxidative phosphorylation. Cancer cells are well known to exhibit high levels of glycolysis¹² and tend to selectively uptake FDG. Therefore, FDG is commonly used in conjunction with PET to find local and distance metastases in a variety of cancer patients.⁵ Other emerging contrast agents, including 3'-deoxy-3'-¹⁸F-fluorothymidine,¹³ ¹⁸F-fluoride,¹⁴ and ¹⁸F-fluoromisonidazole,¹⁵ have also shown promise for tumor detection and characterization.¹⁶ In addition to being able to detect PET tracers, SPECT can also be used to image radioactively-labeled antibodies for the specific detection of tumors.¹⁷ In fact, many such formulations are currently being used in the clinic.

In general, the utility of nuclear imaging is determined by the imaging probes. It is expected that probes will continue to become more-and-more specific and be used in a broad range of cancer applications. Currently, its ability to provide whole-body scans with high sensitivity makes it an indispensable tool in the clinic.

1.1.2 Magnetic Resonance Imaging

Magnetic resonance imaging (MRI) has emerged in recent decades as an incredibly powerful imaging modality capable of generating excellent anatomical, functional, and molecular images.¹⁸ Indeed, contrast in MRI is versatile and can be driven by fat or water content, blood flow, or magnetic contrast agents.

Physics and Image Formation

Magnetic resonance imaging relies on the nuclear magnetic resonance that arises when tissue is placed in a strong magnetic field. The hydrogen atoms cause water molecules to align with the magnetic field and precess at a specific frequency known as the Larmor frequency.

Spatial location is encoded by applying gradients in the magnetic field. Since the Larmor frequency depends on the strength of the magnetic field, these gradients lead to spatial variations in the rate at which the water molecules spin. A radiofrequency (RF) electromagnetic pulse is applied to the patient with its frequency matched to the Larmor frequency in the spatial region of interest. This causes the polarization of those specific molecules to shift. After the RF pulse is applied, the molecules will slowly begin to relax back to be aligned with the magnetic field. As they relax, they emit a RF signal that is detected and used to form an image.

By altering the imaging sequence, a variety of contrast mechanisms can be exploited. For example, the spin-lattice (T_1) or spin-spin (T_2) relaxation times can be measured to differentiate fat from water, or the overall spin density can be measured to visualize the density of water molecules.

Contrast Agents

Magnetic resonance contrast agents work by shortening the relaxation times of the molecules. Thermal vibrations emanating from the magnetic metal ions in the contrast agents work to decrease the relaxation time of the spins by increasing the rate at which the spins transition from their high energy state to their low energy state.

Gadolinium is commonly used as a contrast agent in MRI. It is primarily used for angiography; it generates high contrast in the vasculature after a systemic injection.¹⁹ Gadolinium has thus far served as an enhancer of anatomical and functional contrast, rather than supplying molecular information. Superparamagnetic iron oxide (SPIO) nanoparticles have enabled molecular imaging with MRI. The small particles can extravasate from the leaky vasculature in a tumor and are easily conjugated to antibodies. This enables the imaging of angiogenesis^{20, 21} or cancer cell-surface receptors.^{22, 23}

Overall, MRI is at the forefront of the emerging field of molecular imaging. While it is not as well-established as nuclear imaging for the detection of disease-specific molecular markers, SPIO nanoparticles have continued to expand its influence. Although the high cost and long scan times associated with MRI may temper its ultimate impact.

1.1.3 Optical Imaging

A broad range of optical imaging techniques are being applied to cancer in preclinical and translational applications.^{4, 24} These techniques include diffuse optical tomography (DOT), fluorescent imaging, two-photon imaging, Förster resonance energy transfer (FRET) imaging, surface-enhanced Raman scattering (SERS), optical coherence tomography (OCT), and bioluminescence imaging. Most of these modalities have already made a tremendous impact in the preclinical domain and some are now starting to show clinical success. The remainder of this section will focus on fluorescent imaging, since it has shown the most promise for molecular imaging.

Physics and Image Formation

Contrast in the optical imaging modalities comes from a variety of phenomena. Fluorescent imaging, for example, relies on the excitation of a fluorophore by the absorption of an incident photon. After the excited molecule undergoes radiative relaxation, a photon with a longer wavelength is emitted. Two-photon imaging also relies on the excitation of a fluorophore, but it requires the simultaneous arrival of two photons with a long wavelength for excitation. In FRET imaging, two fluorophores are required, each with a distinct absorption wavelength. When separated by more than a few nanometers, each fluorophore behaves independently; two different wavelengths of light are emitted. However, when they are in close proximity, the absorbed energy from one fluorophore is transferred to the other and only a single wavelength of light is emitted.

Broadly speaking, there are two regimes of photon transport in tissue: ballistic and diffuse. In the ballistic regime, which is limited to approximately 1 mm of depth in tissue, photons are assumed to not have undergone multiple scattering events. Thus, the path of each photon can be reliably estimated. This allows for a conventional camera to acquire images with spatial resolution up to half a wavelength of light. Fluorescent imaging, two-photon imaging, and FRET imaging can all obtain high resolution images in cell culture or superficially in tissue.

Once the imaging depth exceeds 1 mm, however, the spatial resolution quickly decays. This is due to the fact that each photon undergoes multiple scattering events and the exact path cannot be resolved. This practically limits the imaging depth to a couple of centimeters and limits the resolution to the millimeter range.

Images are typically captured with conventional cameras with high sensitivity,²⁵ but tomographic methods²⁶ and modeling of light transport in tissue²⁷ can improve the accuracy of the reconstruction.

Contrast Agents

Fluorescent dyes are the workhorses of optical imaging.^{4, 24, 28} Their small size allows for intracellular labeling and a wide array of dyes enables multiplex imaging.²⁹ These dyes, however, are prone to photobleaching, which limits their utility; the signal can diminish quickly during sustained imaging.³⁰ Furthermore, complex chemistry is often required for molecular labeling of dyes.²⁸

Quantum dots have recently been proposed as an alternative to fluorescent dyes for molecular imaging.^{31, 32} They exhibit brightness and photostability that is 1-2 orders of magnitude greater than dyes.³¹ Furthermore, their surface is easily modified to enable

molecular imaging. Finally, their optical properties can be easily tuned to enable multiplex imaging.³³

Overall, the utility of molecular optical imaging is largely derived from the vast number of reporters currently available. Indeed, new targeted contrast agents are continually emerging for the detection of disease-specific molecular expressions. Despite the low resolution at clinically relevant depths, optical methods promise to play a significant role in the clinic when superficial imaging is required.

1.1.4 Ultrasound Imaging

Ultrasound (US) imaging is widely used in the clinic for a variety of applications because it is safe, inexpensive, and can be performed in real-time. Unlike other imaging modalities which rely on electromagnetic energy for the generation of images, US imaging utilizes acoustic energy. Therefore, its contrast is uniquely derived from variations in the tissue's acoustic impedance.

Physics and Image Formation

Ultrasound imaging begins with the transmission of an US wave, typically from an array of acoustic transducers, into the tissue. The wave can be steered or focused in the tissue by introducing small delays between activation of the individual transducer elements. Inhomogeneity in the acoustic impedance of the tissue results in small reflections of the acoustic wave. The backscattered waves are detected by the same US transducers that transmitted the initial acoustic wave. Because the speed of sound in tissue is relatively constant at 1540 m/s, the total distance the wave traveled – and thus the location of the scattering event – can be determined. Images are formed by summing the contribution of each transducer to each pixel. In pixels containing a strong scattering

event, the signal from the transducers will add constructively, leading to a large signal. In pixels with no scattering, the signals will cancel each other out, resulting in low signal.

The resolution of US imaging, which can be separated into the axial (depth) and lateral resolution, is limited by the bandwidth and, in the case of lateral resolution, the aperture of the transducer. In general, transducers with higher bandwidths and larger apertures will exhibit better resolution. However, there is a tradeoff between imaging depth and resolution. The attenuation of US in tissue is a function of the acoustic frequency; high frequencies are attenuated quicker than low frequencies. Therefore, the bandwidth of the signal necessarily decreases as a function of imaging depth. Transducers with center frequencies of 5-10 MHz are commonly used in the clinic to achieve imaging depths of several cm with spatial resolutions near 100 μm .

An interesting aspect of US images is their characteristic speckled appearance. While the speckle appears to be random noise, it is in fact deterministic; it does not change over time. The speckle pattern is due to interference from the random spatial distribution of small (i.e., less than the wavelength of sound) scatterers in the tissue. The effects of speckle can be mitigated by varying the angle of incidence of the transmitted US wave – a process known as spatial compounding. In practice, however, speckle is generally accepted to be part of the image and does not interfere with the ability of a trained observer to interpret the data.

Contrast Agents

Ultrasound contrast agents seek to exploit the source of contrast in US images: variations in acoustic impedance. The acoustic impedance in gasses is much lower than the impedance in tissue. Therefore, gaseous (e.g., perfluorocarbon) microbubbles are commonly used as US contrast agents.³⁴ These microbubbles are capped with a surfactant

layer (e.g., a lipid bilayer) and can be functionalized to target endothelial markers. Their large size, however, restricts their ability to exit the vasculature and target the tumor parenchymal cells. Recent advances have addressed this by formulating the agents as superheated nanodroplets and activating (i.e., vaporizing) them externally via high intensity US or optical excitation.^{35, 36}

In addition to creating a strong reflection at the liquid/gas boundary, microbubbles can also generate a nonlinear US signal that can be detected for improved localization of the agents. This is because the microbubbles resonate in acoustic fields. The resonant frequency depends on the bubble size and shell thickness/material. When excited at their resonant frequency, the microbubbles emit an acoustic wave which contains the harmonics of the frequency. Thus, high-pass filtering or advanced transmit receive algorithms can be used to isolate the signal emanating from the microbubbles.³⁷

While US imaging is widely used to collect a variety of anatomical and functional information, its impact on the field of molecular imaging has remained limited. This is primarily due to the lack of robust contrast agents which can escape the vasculature interact with molecules of interest. Although, this is likely to change, given the safety of the technique and the ongoing development of nano-sized contrast agents.

1.1.5 Photoacoustic Imaging

Photoacoustic (PA) imaging (also known as optoacoustic imaging) is a largely preclinical imaging modality whose development has rapidly expanded over the last decade. This hybrid technique, which combines optical and ultrasound physics, is based on the PA effect discovered by Alexander Graham Bell over a century ago.³⁸ When a material absorbs light, it can undergo thermoelastic expansion. When the exposure duration is short enough – such that both the heat and the pressure are confined to a small

volume – then a broadband acoustic wave is generated and radiates outward from the optical absorber. This wave is then detected with an ultrasound transducer and the time delay after the initial light pulse is used to form an image.

Physics and Image Formation

In order to detect a PA signal, three events must occur: 1) the optical energy must be absorbed in the medium being imaged, 2) this absorbed energy must be converted into a transient pressure, and 3) the pressure wave must travel to the surface of the medium to be detected by a transducer. If viscosity, shear elasticity, and acoustic inhomogeneities are neglected, these three physical phenomena can be described by a set of linear differential equations.³⁹ First, the temperature rise due to the absorbed optical energy is written as:

$$\frac{\partial T}{\partial t} = \frac{H - \chi \nabla^2 T}{\rho C_p} \quad (1.1)$$

where T is the temperature (K), H is the thermal energy converted per unit time (W/m^3), χ is thermal conductivity ($\text{W}/(\text{m}\cdot\text{K})$), ρ is the mass density (kg/m^3), and C_p is the specific heat capacity at constant pressure ($\text{J}/(\text{kg}\cdot\text{K})$). This temperature rise then results in an expansion of the tissue:

$$\nabla u = -\frac{p}{\rho v_s^2} + \beta T - \frac{\gamma H}{2nc_L \rho v_s^2}, \quad (1.2)$$

where u is the displacement of the tissue (m), p is the pressure (Pa), v_s is the speed of sound in tissue, β is the thermal coefficient of volume expansion (K^{-1}), γ is the electrostrictive coefficient (dimensionless), n is the optical index of refraction

(dimensionless), and c_L is the speed of light in a vacuum (m/s). This initial displacement and pressure rise results in an acoustic wave that travels away from the optically absorber. This can be described by the following equation of motion (which acts as a precursor to the wave equation):

$$\rho \frac{\partial^2 u}{\partial t^2} = -\nabla p. \quad (1.3)$$

At this point, a few assumptions can be made to simplify and combine these three equations. First, it can be assumed that the electrostriction is much less than the optical absorption. Then $\gamma \rightarrow 0$. If the duration of the laser pulse is short enough, then the effects of the thermal conductivity can be assumed to be negligible. This is called the “thermal confinement” condition. In this case, Equations 1.1-1.3 simplify to:

$$\left(\nabla^2 - \frac{1}{v_s^2} \frac{\partial^2}{\partial t^2} \right) p = -\frac{\beta}{C_p} \frac{\partial H}{\partial t}. \quad (1.4)$$

If the laser pulse duration is also short enough so that the pressure rise is restricted to the region of elevated temperature, a condition known as “stress confinement,” then the maximum PA pressure, p_0 , is proportional to the local laser fluence, F (J/m^2), the optical absorption coefficient, μ_a (m^{-1}), and the dimensionless Grüneisen parameter, Γ :

$$p_0 = \Gamma \mu_a F = \frac{\beta v_s^2}{C_p} \mu_a F. \quad (1.5)$$

The Grüneisen parameter is relatively constant in water-based tissue and the laser energy does not have high spatial variations. Therefore, the contrast in PA imaging is

dominated by the optical absorption of the tissue. In fact, if the distribution of F and Γ are known throughout the tissue and the initial pressure rise is accurately reconstructed from the received photoacoustic signals, then a quantitative estimate of μ_a can be obtained. In order to accurately reconstruct a PA image, the following steps must be taken.

First, the initial pressure distribution must be accurately reconstructed. This is typically done through a backprojection (also known as beamforming) approach, though the exact implementation depends on the transducer geometry.⁴⁰ In general, each transducer receives an acoustic wave at a certain time after the initial laser pulse. If the speed of sound is assumed to be constant in the tissue, the time delay between the laser pulse and the received acoustic wave is proportional to the distance between the transducer and the photoabsorber. Therefore, the signal in each spatial location can be represented as simply the sum of the acoustic signal acquired at each transducer, with the appropriate delay applied.

Next, the conversion of optical energy to acoustic pressure must be determined. This depends primarily on the Grüneisen parameter, Γ , in the environment surrounding the photo-absorbing molecules or particles.⁴¹ In water-based tissue, the Grüneisen parameter is relatively constant. The parameter, however, does vary as a function of temperature. While it does affect the ability to create quantitative PA images, it does open up the possibility for PA-based thermal imaging. Indeed, PA imaging presents a synergistic method for image guidance of photothermal therapy.⁴²⁻⁴⁴

Finally, the fluence distribution in the tissue must be estimated. For non-scattering media, this can simply be done by applying the Beer-Lambert Law:

$$F(z) = F_0 e^{-\mu_a z}, \quad (1.6)$$

where, z is the distance the light has traveled in the medium and F_0 is the initial fluence at the medium's surface. Tissue, however, also contains a large optical scattering coefficient, μ_s . The Beer-Lambert Law can still be used to estimate the fluence in tissue by replacing μ_a with an effective attenuation coefficient:

$$\mu_{eff} = \sqrt{3 \cdot \mu_a(\mu_a + \mu_s \cdot g)}, \quad (1.7)$$

where g is the anisotropy of scattering in the tissue. Of course, this is only an approximation and better estimates can be obtained.

In order to improve upon the Beer-Lambert Law, Monte Carlo simulations are often used to model the propagation of photons in tissue.²⁷ If the tissue is relatively homogenous or piecewise homogenous, then an accurate estimation of the fluence can be obtained with this method. The main drawbacks of Monte Carlo simulations are they are time consuming and large spatial variations in the optical properties (e.g., the optical absorption in a small blood vessel) can lead to significant errors.

In general, the spatial distribution of the optical absorption in the tissue can significantly affect the fluence. This complicates Equation 1.5. For the best estimate of μ_a , the absorption, the scattering, and the fluence must be solved for simultaneously at each point in space. These multiple unknowns mean that more than just a single image must be captured. Additional information can be obtained by changing the optical excitation wavelength, λ , or the initial laser fluence, F_0 .^{45, 46} However, given the randomized nature of light propagation in inhomogeneous media, quantitative PA imaging remains elusive.⁴⁵

Spectroscopic Photoacoustic Imaging

Spectroscopic PA (sPA) makes use of the fact that μ_a typically varies greatly as a function of optical wavelength, λ . Because the PA pressure is directly proportional to μ_a (Eq. 1.5), multiple PA images can be acquired using different excitation wavelengths, and local variations in amplitude can be used to estimate the optical absorption spectrum, $\mu_a(\lambda)$.⁴⁷ The spectrum can be compared to the known absorption spectra of tissue components or exogenous contrast agents to determine the relative concentrations of each component. This powerful technique enables, among other things, the measurement of oxygen saturation in blood, visualization of the deposition or activation of a contrast agent, or identification of melanoma.⁴⁷⁻⁵⁰

Equation 1.5 can be modified to incorporate the optical wavelength, λ . In practice, F can vary greatly depending on optical properties of tissue and λ . Furthermore, μ_a is a function of λ and each of N distinct absorbers in the region of interest will contribute to the overall absorption. Thus, Equation 1.5 becomes:

$$P(\lambda) = \Gamma F(\lambda) (\mu_{a_1}(\lambda) + \mu_{a_2}(\lambda) + \cdots + \mu_{a_N}(\lambda)). \quad (1.8)$$

The optical absorption can be related to the concentration of an absorber and the absorption cross section as follows:

$$\mu_{a_i}(\lambda) = C[i]\epsilon_{a_i}(\lambda), \quad (1.9)$$

where $C[i]$ is the concentration of the i^{th} absorber and $\epsilon_{a_i}(\lambda)$ is the molar absorption cross section of the i^{th} absorber at wavelength λ . Equation 1.9 is then expanded to:

$$P(\lambda) = \Gamma F(\lambda) (C[1]\varepsilon_{a_1}(\lambda) + C[2]\varepsilon_{a_2}(\lambda) + \cdots + C[N]\varepsilon_{a_N}(\lambda)). \quad (1.10)$$

The Grüneisen parameter is tissue-dependent and has little variation in water-based tissues at constant temperature. Therefore, it is often assumed to be constant. If the fluence at the absorber is known, then the optical absorption coefficient vector, $\mu_{\text{est}}(\lambda)$, can be estimated:

$$\mu_{\text{est}}(\lambda) = \frac{P(\lambda)}{\Gamma F(\lambda)}. \quad (1.11)$$

Then Eq. 1.10 can be simplified to a set of linear equations:

$$\boldsymbol{\mu}_{\text{est}} = \boldsymbol{\varepsilon} \mathbf{C}, \quad (1.12)$$

where $\boldsymbol{\mu}_{\text{est}}$ is a vector whose components correspond to the reconstructed absorption coefficient at each individual optical wavelength, $\boldsymbol{\varepsilon}$ is the absorption cross-section matrix whose rows correspond to optical wavelengths and columns are the normalized absorption cross section spectra of the optical absorbers (i.e., $\varepsilon_{ij} = \varepsilon_{a_j}(\lambda_i)$), and \mathbf{C} is a vector whose elements correspond to the relative concentration of each optical absorber. Note that the bold notation indicates a vector/matrix.

In order to solve Eq. 1.12 for the absorber concentrations, the number of optical wavelengths used to acquire images, M , must be greater than or equal to the number of absorbers, N . In the presence of noise, it is useful to have $M > N$, thus making Eq. 1.12 over-constrained. In this case, a least squared error estimate of \mathbf{C} can be found:

$$\mathbf{C} \approx \boldsymbol{\varepsilon}^+ \boldsymbol{\mu}_{\text{est}}, \quad (1.13)$$

where $\boldsymbol{\varepsilon}^+$ is the Moore-Penrose *pseudoinverse* of $\boldsymbol{\varepsilon}$, defined as⁵¹

$$\boldsymbol{\varepsilon}^+ = (\boldsymbol{\varepsilon}^T \boldsymbol{\varepsilon})^{-1} \boldsymbol{\varepsilon}^T. \quad (1.14)$$

This estimate of the concentrations has been used to simultaneously measure SO₂ and the concentration of a dye or nanoparticles *in vivo*.^{47, 52} Further modifications can be made to Eq. 1.13 to ensure the sum of the concentrations is 1 and negative concentrations (an artifact related to finite signal-to-noise ratio of the images or the presence of an absorber not included in absorption cross-section matrix) are avoided.^{47, 53}

Contrast Agents

Any biocompatible molecule or particle which exhibits a strong optical absorption is well suited to act as a contrast agent for PA imaging. Indeed, a large variety of contrast agents have been used, ranging from carbon nanotubes to indocyanine green dye to plasmonic nanoparticles.^{47, 54-61} These contrast agents have been used to enhance the photoacoustic signal in the vasculature, identify molecular expressions in tumors, visualize flow through the lymphatic system, and provide combined contrast for PA and US imaging.^{36, 57, 61-68}

Fluorescent dyes which are used for molecular optical imaging can also be used for photoacoustic imaging.^{57, 69} However, there is a compromise between the fluorescence and the PA signal. The percentage of the absorbed energy which is fluoresced – known as the quantum yield of a dye – is ideally maximized for optical imaging. Photoacoustic

imaging of dyes, however, relies on nonradiative relaxation of the molecules (i.e., the energy must be absorbed and not fluoresced). Therefore, dyes with low quantum yields are well-suited for PA imaging. While dyes are inexpensive and prevalent, they are typically small molecules (less than 1 nm) which leads to rapid clearance (often less than 5 minutes) from the bloodstream via the kidneys. While full clearance is desirable in a biomedical setting, the short lifespan of the dyes in circulation limits their utility. This shortcoming can be addressed by encapsulating the dye in a larger carrier, such as a liposome or micelle.⁵⁷

Plasmonic nanoparticles offer some distinct advantages over dyes for PA imaging. First, because of the plasmon resonance effect, a single nanoparticle can exhibit an optical absorption that is five orders of magnitude greater than a single dye molecule.⁷⁰ Second, the size of plasmonic nanoparticles can be easily tuned to between 5 nm and 200 nm. Third, the optical properties can be finely controlled by adjusting the size and shape of the particle.⁷¹ Fourth, the surface of a plasmonic nanoparticle can be easily modified to enhance circulation time or enable molecular targeting.^{72, 73} This unique set of benefits makes plasmonic nanoparticles well suited for a variety of applications.⁵⁴ Nanoparticles, however, do come with the caveat that they will not be easily translated into a clinical setting. This is due to the fact that gold nanoparticles larger than 5 nm have not been shown to fully clear the body. They tend to accumulate in the filtering organs, primarily the liver and spleen.⁷⁴ Although plasmonic nanoparticles are not cytotoxic, the long term effects of their accumulation are not yet known.^{61, 75} In the meantime, they provide an excellent platform for preclinical molecular PA imaging studies.

1.1.6 A Qualitative Comparison of Biomedical Imaging Modalities

Every biomedical imaging modality has the ability to provide information in all three categories to varying degrees. A qualitative map showing the relative quality anatomical, functional, and molecular images generated by prominent clinical and preclinical imaging modalities is shown in Figure 1.2. The uniqueness of each modality on the chart shows that no single modality is best and the choice of modality is application dependent. For example, planar x-ray imaging and x-ray computed tomography (CT) can provide excellent anatomical information, yet very little functional and molecular information can be obtained from these images. Conversely, nuclear imaging techniques – PET and SPECT – are able to provide rich functional and molecular images, yet they provide almost no anatomical context. To that end, CT and PET/SPECT are often combined to give a more complete picture of the patient. Nuclear magnetic resonance imaging can provide good images in all three categories, but it is an expensive and slow technique.

At the same time that there are tradeoffs in the types of information that each modality can provide, the imaging depth and resolution vary from modality to modality. Figure 1.3 shows the approximate resolution and imaging depth of the predominant molecular imaging modalities. Optical and PA imaging are able to achieve the best resolution (limited only by the diffraction of the light); however, this resolution is only achieved when the optical scattering caused by tissue is minimal (i.e., at depths of less than 1 mm). Both CT and MRI are able to provide full body images at good resolution, making them well suited for a variety of clinical applications. Nuclear imaging techniques (PET and SPECT) also enable full-body imaging, but the resolution is much lower than the other modalities. Ultrasound (US) imaging offers good resolution images

at medium depths. It cannot provide whole-body images, but it is useful when a quick, localized scan is needed.

1.2 MOLECULAR TARGETS IN TUMORS

Every molecular imaging modality needs a specific protein or enzyme expression to target in a tumor. These targets are typically derived from emerging therapeutics. Thus, the molecular image can be used to predict the response of the tumor to that specific therapy. The choice of molecular target is driven by the relevance to the disease, the location of the target, and the existence of a targeting molecule.

The most accessible molecular targets are extracellular molecules (e.g., autocrines or enzymes) or transmembrane proteins (e.g., integrins or cell surface receptors). In molecular imaging of cancer, cell surface receptors present excellent targets. There are several clinically approved drugs that target these receptors, meaning molecular imaging has direct clinical relevance. The growth factor receptor family – most notably the human epidermal growth factor receptor type 1 (EGFR) and 2 (HER2) – are often overexpressed in several types of cancer and they promote cell growth and proliferation.^{76, 77} In fact, EGFR is overexpressed in more than 90% of head and neck cancer patients and HER2 is overexpressed in 20% of breast cancer patients.^{78, 79} This has led to the widespread clinical use of EGFR and HER2 antibodies – cetuximab and trastuzumab, respectively – as adjuvant treatment options.^{80, 81} The clinical success of these therapeutics has led to a great deal of interest in noninvasively identifying the overexpression of EGFR^{22, 61, 82-89} and HER2^{32, 57, 90-93} using molecular imaging. In addition to the epidermal growth factor receptor family, the estrogen receptor, folate receptor, $\alpha_v\beta_3$ integrin, and vascular endothelial growth factor receptor have proven to be useful targets for drugs⁹⁴⁻⁹⁷ and molecular imaging.^{20, 98-103}

The matrix metalloproteinase (MMP) family of enzymes has also proven to be a useful biomarker.^{49, 104} These enzymes, which are commonly excreted by either the tumor stroma or paracrine cells, help to degrade the extracellular matrix and promote extravasation.¹⁰⁵ However, given the ubiquity of MMPs in normal tissue, an effective drug has remained elusive – though research efforts have sustained.¹⁰⁶ Activatable optical probes have been used with fluorescence and photoacoustic imaging to detect elevated levels of MMP expression.^{49, 69, 104, 107} In spite of the lack of clinical therapeutics targeted at MMPs, the detection of MMPs may present a valuable way to predict the malignancy of a tumor.¹⁰⁸⁻¹¹⁰

An abundance of small molecular targeted drugs have recently emerged. Unlike antibodies, these drugs target intracellular proteins and must be transported across the cellular membrane. Once inside the cell, the drugs inhibit tyrosine, mitogen-activated, or serine/threonine protein kinases.¹¹¹ These protein kinases serve a critical role in the downstream pathways of the previously-discussed cell-surface receptors, and mutations often activate these pathways, regardless of cell-surface receptor expression.¹¹² Delivering targeted contrast agent to these intracellular targets has proven difficult and much of the imaging of these molecules has been performed with genetically modified cells, rather than exogenous contrast agents.¹¹³ Emerging technologies, such as the attachment of cell penetrating peptides to the contrast agent, are encouraging for the imaging of these intracellular targets.^{104, 114}

While it is still in its infancy, molecular imaging has already begun to make an impact in the clinic. A future can be imagined where a set of imaging probes can be used to characterize the molecular expressions in a tumor, predict its progression, and determine an optimal treatment strategy. In an era of personalized medicine, determining this information in noninvasively in real-time is an exciting prospect.

1.3 CANCER STAGING AND LYMPHATIC IMAGING

1.3.1 Cancer Staging

The spread of cancer cells from the primary tumor is the most important prognostic indicator.¹¹⁵ Indeed, the majority of cancer deaths are the result metastases rather than the primary tumor. Therefore, physicians often use a classification scheme known as “staging” to describe the spread and aggressiveness of a tumor.¹¹⁶ Staging takes into account the site and extent of primary tumor, regional lymph node involvement, presence of distant metastases, and tumor grade.

Cancer staging is often performed with the TNM system which characterizes the size of the primary tumor (T), the number and location of affected lymph nodes (N), and the presence of distant metastases (M). The TNM categorization is then used to assign a single staging number, which is dependent on the type of cancer. Cancer stages range from 0 (carcinoma *in situ*) to IV (distant metastases are present). In general, an increasing cancer stage corresponds to growth of the primary tumor, spread to regional lymph nodes and organs, and finally the presence of distant metastases. In addition to predicting outcome of the patient, the tumor stage is used to identify the best course of treatment and determine eligibility for clinical trials.

1.3.2 Sentinel Lymph Node Biopsy

The lymphatic system plays a crucial role in the progression of cancer. Many types of cancer, including head and neck, breast, gastrointestinal, and skin cancer, metastasize to the regional lymph nodes.¹¹⁷⁻¹²⁰ The presence of metastases in the regional nodes is often a harbinger of more distant metastases.¹¹⁷ Therefore, it is often critically important for staging and treatment planning to know the extent of the spread of the disease.

The lymphatic spread of cancer is commonly detected by a sentinel lymph node (SLN) biopsy.¹¹⁹ The SLN is defined as the first lymph node to which a primary tumor drains. The procedure involves an injection of a radioactive colloid and/or optical dye near the primary tumor. Lymphoscintigraphy and visual inspection is used to identify the SLN. After resection of the SLN, samples are sent for histological processing and pathological evaluation. After several days to a few weeks, the patient receives the results of the analysis.

Despite its high accuracy and general clinical acceptance, the SLN biopsy procedure does have some drawbacks. First, the SLN biopsy procedure and SLN resection – which can be performed during the biopsy procedure or after a metastasis has been detected – are both invasive and commonly result in lymphedema and nerve damage.^{121, 122} In fact, lymphedema and numbness were experienced by 3.5% and 10.9%, respectively, of breast cancer patients undergoing an SLN biopsy. The occurrence is much higher for patients undergoing elective axillary lymph node resection (19.1% and 37.7%, respectively).¹²² Second, the radioactive colloid exposes the patient to harmful radiation. Third, the procedure is subject to false negatives. For example, in melanoma patients, false negatives for the SLN biopsy procedure range from 5-9%.¹²³ These false negatives are often due to the presence of metastases which are in transit to (but not yet inside) the SLN at the time of the biopsy or sampling error. Finally, the long waiting time could lead to patient anxiety and progression of the disease.

1.3.3 Imaging of Cancer in the Lymphatics

Because of the limitations of the sentinel lymph node biopsy, several biomedical imaging modalities have been suggested to improve or replace the SLN biopsy procedure. Two main contributions of biomedical imaging have been proposed: 1)

improve the accuracy and decrease the morbidity of the SLN biopsy through image guidance, and 2) replace the SLN biopsy procedure by detecting metastases in the SLN noninvasively. A variety of imaging methods have shown a great deal of promise for the former, while the latter has seen only modest success.^{124, 125}

Fluorescent imaging,²⁵ MRI,¹²⁶ US imaging,¹²⁷ x-ray imaging,¹²⁸ and PA imaging⁶⁴⁻⁶⁸ have each been used to map the SLN in animal models. The imaging procedure mirrors that of the SLN biopsy. After injection of a contrast agent near the primary tumor, drainage of the contrast agent is monitored to identify the SLN and map the lymphatic system in the area. There are two main benefits to adopting an image-guided SLN biopsy procedure. First, the need for a radioactive colloid could be removed. Second, the procedure itself could be refined and more-accurate, less-invasive results could be achieved; visual inspection of the dye drainage could be replaced with more sensitive imaging methods.

Detecting small metastases in the regional lymph nodes with biomedical imaging has remained an elusive task. Initial efforts focused on detecting anatomical and functional changes in the lymph node resulting from the invasion of cancer cells. For example, US imaging has been used to visualize elevated blood flow and morphological changes (i.e., a rounding and enlarging of the node) that indicate the presence of a metastasis.¹²⁹ However, the sensitivity and specificity of the method are not high enough to warrant the replacement of SLN resection. Positron emission tomography with FDG has been shown to reliably detect metastases larger than 80 mm³.¹³⁰ When the metastases are impalpable, however, the sensitivity and specificity fall to 50% and 87%, respectively.¹³¹ Fluorescent imaging of dye-labeled antibodies also shows promise for the detection of SLN metastasis, but more work needs to be done to extend preliminary results.⁸⁹ Initial clinical results of MRI before and after the administration of SPIO

nanoparticles showed a sensitivity and specificity of greater than 90% in the detection of lymph node metastases.¹³² The method, however, requires multiple imaging sessions and relies on negative contrast, which can be unreliable. Furthermore, the size of detected metastasis was limited to the millimeter range.

Although there have been many promising preclinical and translational results showing the utility of imaging the lymphatic system, further advancements need to be made before the technologies are adopted in the clinic. A noninvasive method to detect micrometastases in the SLN could prove invaluable for early detection of the spread of a tumor. Ideally, the method would exhibit high (near 100%) sensitivity and specificity, would result in minimal morbidity or toxicity, and could be performed in real-time with instantaneous results. Such a technique could improve survival rates and reduce unnecessary treatment.

1.4 RESEARCH GOALS

The overall research goals presented of this project are focused on the improvement of photoacoustic imaging technology and its application to a clinically appropriate model of cancer. This includes the simultaneous development and optimization of imaging algorithms, nanoparticle contrast agents, and small animal models. Specifically, the aims of this dissertation are create tools that would improve a physician's ability to accurately identify the spread of cancer through the lymphatic systems. This will be done by improving the guidance of SLN mapping with PA imaging and by noninvasively detecting micrometastases in the SLN with ultrasound-guided molecular sPA imaging.

Chapter 2 focuses on detecting functional changes in lymph nodes as they are invaded with metastases. Spectroscopic photoacoustic imaging is used to observe

hypoxia throughout the metastatic node, even when the metastases are small (less than 200 μm). The resulting technique – which requires no administration of contrast agents or exposure to unsafe ionizing radiation – could easily be adapted in the clinic to augment current screening procedures.

The concept is extended to molecular specific detection of micrometastases in the lymphatics in Chapter 3. Upon cellular interaction, molecularly targeted gold nanospheres targeted to EGFR change optical properties – a result of aggregation and plasmon coupling. The nanoparticles which have interacted with small colonies of metastatic cells are specifically detected with sPA imaging. The results suggest that the method could be used for noninvasive cancer staging in real-time.

Chapter 4 explores the role of the optical imaging wavelengths used in sPA imaging. A method to select wavelengths based on the optical properties of absorbers is presented. Simulations, phantom imaging, and *in vivo* imaging indicate that the choice of wavelengths is critical for spectral unmixing accuracy.

Finally, Chapter 5 presents an alternative to sPA imaging for SLN mapping, which can be time-intensive and computationally expensive. High contrast single-wavelength PA images of silica-coated gold nanoplates draining through the lymphatics indicate that PA imaging could improve the accuracy and safety of the SLN biopsy procedure.

A future outlook and the short and long term path to the clinic are explored in Chapter 6. A case is made for the immediate clinical investigation of label-free sPA lymph node imaging. The other technologies presented in this dissertation involve plasmonic nanoparticles. Therefore the necessary intermediate steps for clinical translation are presented. Finally, some preclinical corollaries to the present work (e.g., photothermal therapy of the SLN) are discussed.

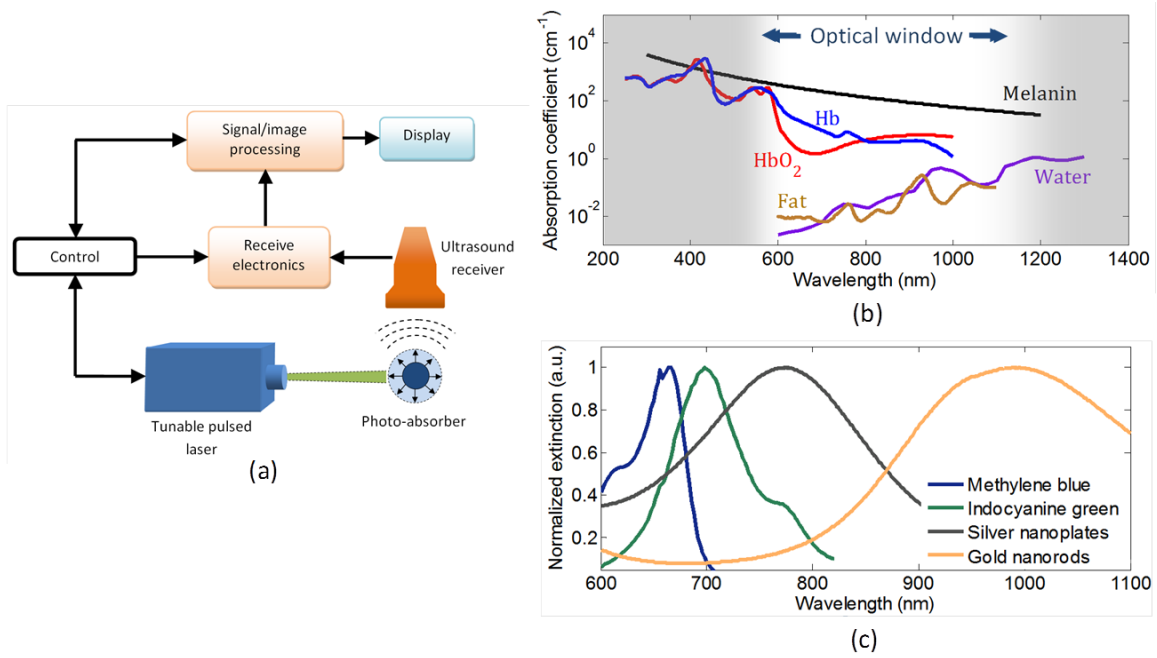


Figure 1.1 a) A block diagram of a typical photoacoustic imaging system, b) the absorption spectra of common endogenous tissue components with the optical window depicted, and c) absorption spectra of four contrast agents that span the optical window.

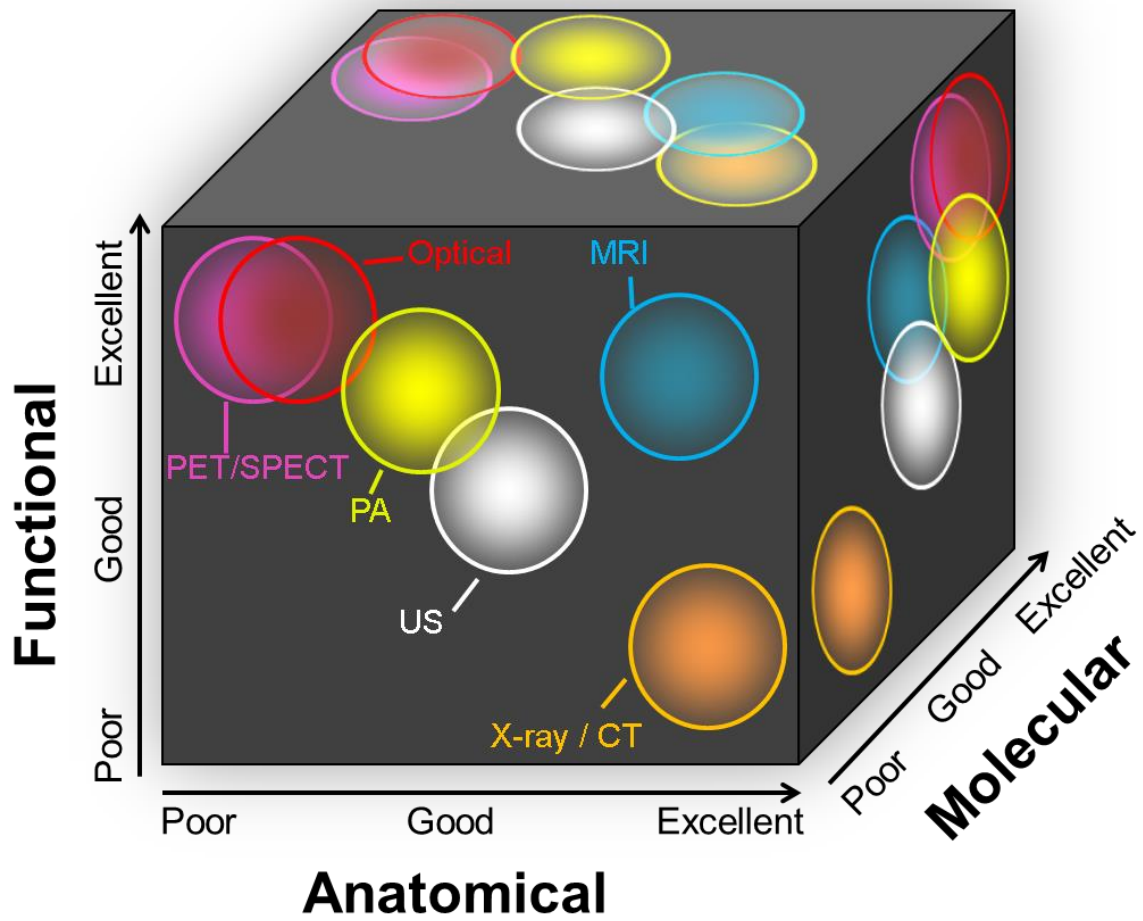


Figure 1.2 A qualitative map showing the ability of biomedical imaging modalities to provide anatomical, functional, and molecular information.

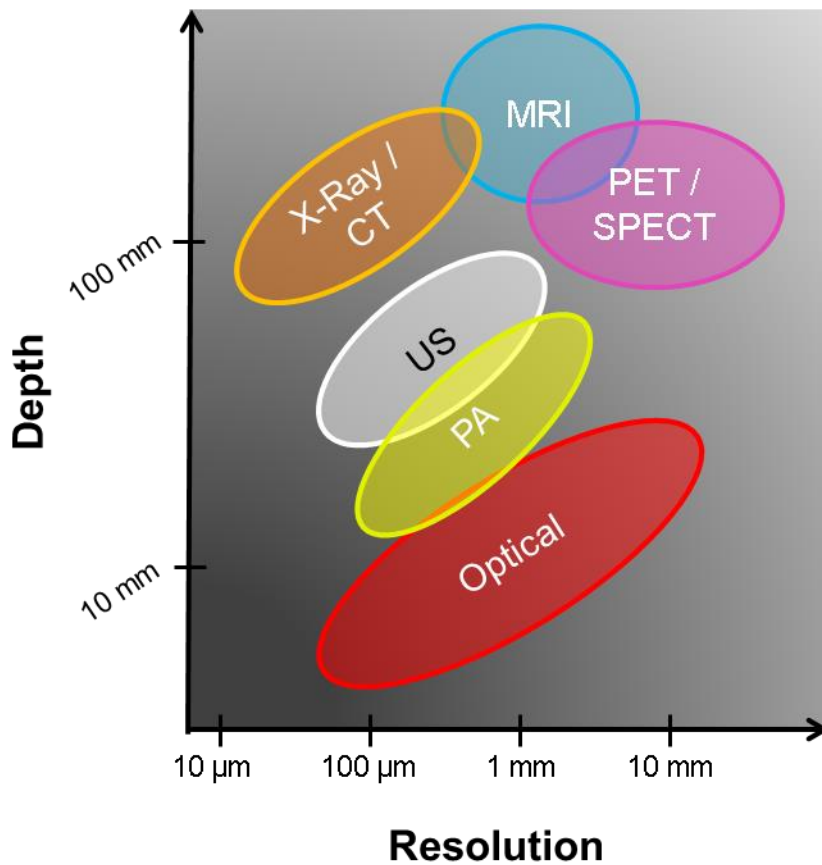


Figure 1.3 A graph showing the approximate resolution and imaging depth achieved with biomedical imaging modalities.

1.5 REFERENCES

1. Hanahan, D. & Weinberg, R.A. The hallmarks of cancer. *cell* **100**, 57-70 (2000).
2. Hanahan, D. & Weinberg, R.A. Hallmarks of cancer: the next generation. *Cell* **144**, 646-674 (2011).
3. Weissleder, R. Molecular imaging in cancer. *Science* **312**, 1168-1171 (2006).
4. Weissleder, R. & Ntziachristos, V. Shedding light onto live molecular targets. *Nature medicine* **9**, 123-128 (2003).
5. Gambhir, S.S. Molecular imaging of cancer with positron emission tomography. *Nat Rev Cancer* **2**, 683-693 (2002).

6. Kaufmann, B.A. & Lindner, J.R. Molecular imaging with targeted contrast ultrasound. *Current opinion in biotechnology* **18**, 11-16 (2007).
7. Mallidi, S., Luke, G.P. & Emelianov, S. Photoacoustic imaging in cancer detection, diagnosis, and treatment guidance. *Trends in Biotechnology* **29**, 213-221 (2011).
8. Harris, A.L. Hypoxia - a key regulatory factor in tumour growth. *Nat Rev Cancer* **2**, 38-47 (2002).
9. Shepp, L.A. & Vardi, Y. Maximum likelihood reconstruction for emission tomography. *Medical Imaging, IEEE Transactions on* **1**, 113-122 (1982).
10. Jaszczak, R.J., Greer, K.L., Floyd Jr, C.E., Harris, C.C. & Coleman, R.E. Improved SPECT quantification using compensation for scattered photons. *Journal of nuclear medicine: official publication, Society of Nuclear Medicine* **25**, 893-900 (1984).
11. Gambhir, S.S. et al. A tabulated summary of the FDG PET literature. *Journal of nuclear medicine* **42**, 1S-93S (2001).
12. Warburg, O. On the origin of cancer cells. *Science* **123**, 309-314 (1956).
13. Been, L.B. et al. [18F] FLT-PET in oncology: current status and opportunities. *European journal of nuclear medicine and molecular imaging* **31**, 1659-1672 (2004).
14. Beheshti, M. et al. Detection of bone metastases in patients with prostate cancer by 18F fluorocholine and 18F fluoride PET-CT: a comparative study. *European journal of nuclear medicine and molecular imaging* **35**, 1766-1774 (2008).
15. Koh, W.-J. et al. Imaging of hypoxia in human tumors with [F-18] fluoromisonidazole. *International Journal of Radiation Oncology* Biology* Physics* **22**, 199-212 (1992).
16. Wester, H.-J. Nuclear imaging probes: from bench to bedside. *Clinical cancer research* **13**, 3470-3481 (2007).
17. Jaffer, F.A. & Weissleder, R. Molecular imaging in the clinical arena. *JAMA: the journal of the American Medical Association* **293**, 855-862 (2005).
18. Lauterbur, P.C. Image Formation by Induced Local Interactions - Examples Employing Nuclear Magnetic-Resonance. *Nature* **242**, 190-191 (1973).

19. Meaney, J.F. et al. Diagnosis of pulmonary embolism with magnetic resonance angiography. *New England Journal of Medicine* **336**, 1422-1427 (1997).
20. Sipkins, D.A. et al. Detection of tumor angiogenesis in vivo by $\alpha\beta 3$ -targeted magnetic resonance imaging. *Nature medicine* **4**, 623-626 (1998).
21. Pearlman, J.D. et al. Magnetic resonance mapping demonstrates benefits of VEGF-induced myocardial angiogenesis. *Nature medicine* **1**, 1085-1089 (1995).
22. Suwa, T., Ozawa, S., Ueda, M., Ando, N. & Kitajima, M. Magnetic resonance imaging of esophageal squamous cell carcinoma using magnetite particles coated with anti-epidermal growth factor receptor antibody. *International Journal of Cancer* **75**, 626-634 (1998).
23. Daldrop-Link, H.E. et al. In vivo tracking of genetically engineered, anti-HER2/neu directed natural killer cells to HER2/neu positive mammary tumors with magnetic resonance imaging. *European radiology* **15**, 4-13 (2005).
24. Ntziachristos, V., Ripoll, J., Wang, L.V. & Weissleder, R. Looking and listening to light: the evolution of whole-body photonic imaging. *Nature biotechnology* **23**, 313-320 (2005).
25. Kim, S. et al. Near-infrared fluorescent type II quantum dots for sentinel lymph node mapping. *Nat Biotechnol* **22**, 93-97 (2004).
26. Montet, X. et al. Tomographic fluorescence imaging of tumor vascular volume in mice. *Radiology* **242**, 751-758 (2007).
27. Wang, L., Jacques, S.L. & Zheng, L. MCML--Monte Carlo modeling of light transport in multi-layered tissues. *Computer methods and programs in biomedicine* **47**, 131-146 (1995).
28. Ntziachristos, V., Bremer, C. & Weissleder, R. Fluorescence imaging with near-infrared light: new technological advances that enable in vivo molecular imaging. *European radiology* **13**, 195-208 (2003).
29. Mansfield, J.R., Gossage, K.W., Hoyt, C.C. & Levenson, R.M. Autofluorescence removal, multiplexing, and automated analysis methods for in-vivo fluorescence imaging. *Journal of biomedical optics* **10**, 041207-041207-041209 (2005).
30. Patterson, G.H. & Piston, D.W. Photobleaching in two-photon excitation microscopy. *Biophysical journal* **78**, 2159-2162 (2000).
31. Chan, W.C. & Nie, S. Quantum dot bioconjugates for ultrasensitive nonisotopic detection. *Science* **281**, 2016-2018 (1998).

32. Wu, X. et al. Immunofluorescent labeling of cancer marker Her2 and other cellular targets with semiconductor quantum dots. *Nature biotechnology* **21**, 41-46 (2002).
33. Chan, W.C. et al. Luminescent quantum dots for multiplexed biological detection and imaging. *Current opinion in biotechnology* **13**, 40-46 (2002).
34. Ferrara, K., Pollard, R. & Borden, M. Ultrasound microbubble contrast agents: fundamentals and application to gene and drug delivery. *Annu Rev Biomed Eng* **9**, 415-447 (2007).
35. Kripfgans, O.D., Fowlkes, J.B., Miller, D.L., Eldevik, O.P. & Carson, P.L. Acoustic droplet vaporization for therapeutic and diagnostic applications. *Ultrasound Med Biol* **26**, 1177-1189 (2000).
36. Wilson, K., Homan, K. & Emelianov, S. Biomedical photoacoustics beyond thermal expansion using triggered nanodroplet vaporization for contrast-enhanced imaging. *Nat Commun* **3**, 618 (2012).
37. Needles, A. et al. Nonlinear contrast imaging with an array-based micro-ultrasound system. *Ultrasound Med Biol* **36**, 2097-2106 (2010).
38. Bell, A.G. Upon the production of sound by radiant energy. *Philosophical Magazine Series 5* **11**, 510-528 (1881).
39. Wang, L.V. Photoacoustic Imaging and Spectroscopy, Edn. 1. (CRC Press, 2009).
40. Xu, M. & Wang, L.V. Photoacoustic imaging in biomedicine. *Review of Scientific Instruments* **77**, 041101 (2006).
41. Chen, Y.-S., Frey, W., Aglyamov, S. & Emelianov, S. Environment-Dependent Generation of Photoacoustic Waves from Plasmonic Nanoparticles. *Small* **8**, 47-52 (2012).
42. Shah, J., Aglyamov, S.R., Sokolov, K., Milner, T.E. & Emelianov, S.Y. Ultrasound imaging to monitor photothermal therapy - Feasibility study. *Optics Express* **16**, 3776-3785 (2008).
43. Kim, S. et al. in Ultrasonics Symposium (IUS), 2010 IEEE 233-236 (2010).
44. Chen, Y.S., Frey, W., Walker, C., Aglyamov, S. & Emelianov, S. Sensitivity enhanced nanothermal sensors for photoacoustic temperature mapping. *Journal of biophotonics* (2013).

45. Cox, B., Laufer, J.G., Arridge, S.R. & Beard, P.C. Quantitative spectroscopic photoacoustic imaging: a review. *J Biomed Opt* **17**, 061202 (2012).
46. Cook, J.R., Frey, W. & Emelianov, S. Quantitative Photoacoustic Imaging of Nanoparticles in Cells and Tissues. *ACS nano* (2013).
47. Kim, S., Chen, Y.-S., Luke, G.P. & Emelianov, S.Y. In vivo three-dimensional spectroscopic photoacoustic imaging for monitoring nanoparticle delivery. *Biomed. Opt. Express* **2**, 2540-2550 (2011).
48. Wang, X., Xie, X., Ku, G., Wang, L.V. & Stoica, G. Noninvasive imaging of hemoglobin concentration and oxygenation in the rat brain using high-resolution photoacoustic tomography. *J Biomed Opt* **11**, 024015 (2006).
49. Levi, J. et al. Molecular Photoacoustic Imaging of Follicular Thyroid Carcinoma. *Clinical Cancer Research* **19**, 1494-1502 (2013).
50. Kim, C. et al. In Vivo Molecular Photoacoustic Tomography of Melanomas Targeted by Bioconjugated Gold Nanocages. *ACS Nano* **4**, 4559-4564 (2010).
51. Penrose, R. & Todd, J.A. On best approximate solutions of linear matrix equations. *Mathematical Proceedings of the Cambridge Philosophical Society* **52**, 17-19 (1956).
52. Li, M.-L. et al. Simultaneous Molecular and Hypoxia Imaging of Brain Tumors In Vivo Using Spectroscopic Photoacoustic Tomography. *Anglais* **96** (2008).
53. Keshava, N. & Mustard, J.F. Spectral unmixing. *Ieee Signal Proc Mag* **19**, 44-57 (2002).
54. Luke, G.P., Yeager, D. & Emelianov, S.Y. Biomedical applications of photoacoustic imaging with exogenous contrast agents. *Ann Biomed Eng* **40**, 422-437 (2012).
55. de la Zerda, A. et al. Ultrahigh sensitivity carbon nanotube agents for photoacoustic molecular imaging in living mice. *Nano Lett* **10**, 2168-2172 (2010).
56. De la Zerda, A. et al. Carbon nanotubes as photoacoustic molecular imaging agents in living mice. *Nat Nanotechnol* **3**, 557-562 (2008).
57. Kim, G. et al. Indocyanine-green-embedded PEBBLEs as a contrast agent for photoacoustic imaging. *J Biomed Opt* **12**, 044020 (2007).

58. Buehler, A., Herzog, E., Razansky, D. & Ntziachristos, V. Video rate optoacoustic tomography of mouse kidney perfusion. *Opt Lett* **35**, 2475-2477 (2010).
59. Taruttis, A., Herzog, E., Razansky, D. & Ntziachristos, V. Real-time imaging of cardiovascular dynamics and circulating gold nanorods with multispectral optoacoustic tomography. *Opt Express* **18**, 19592-19602 (2010).
60. Homan, K. et al. Silver nanosystems for photoacoustic imaging and image-guided therapy. *Journal of Biomedical Optics* **15**, 021316 (2010).
61. Homan, K.A. et al. Silver Nanoplate Contrast Agents for in Vivo Molecular Photoacoustic Imaging. *ACS Nano* **6**, 641-650 (2012).
62. Wang, Y. et al. Photoacoustic Tomography of a Nanoshell Contrast Agent in the in Vivo Rat Brain. *Nano Letters* **4**, 1689-1692 (2004).
63. Bayer, C.L., Luke, G.P. & Emelianov, S.Y. Photoacoustic Imaging for Medical Diagnostics. *Acoustics Today* **8**, 15-23 (2012).
64. Cai, X. et al. In vivo quantitative evaluation of the transport kinetics of gold nanocages in a lymphatic system by noninvasive photoacoustic tomography. *ACS Nano* **5**, 9658-9667 (2011).
65. Pan, D. et al. Near infrared photoacoustic detection of sentinel lymph nodes with gold nanobeacons. *Biomaterials* **31**, 4088-4093 (2010).
66. Song, K.H., Kim, C., Cobley, C.M., Xia, Y. & Wang, L.V. Near-Infrared Gold Nanocages as a New Class of Tracers for Photoacoustic Sentinel Lymph Node Mapping on a Rat Model. *Nano Letters* **9**, 183-188 (2008).
67. Song, K.H., Kim, C., Maslov, K. & Wang, L.V. Noninvasive in vivo spectroscopic nanorod-contrast photoacoustic mapping of sentinel lymph nodes. *European Journal of Radiology* **70**, 227-231 (2009).
68. Song, K.H., Stein, E.W., Margenthaler, J.A. & Wang, L.V. Noninvasive photoacoustic identification of sentinel lymph nodes containing methylene blue in vivo in a rat model. *Journal of Biomedical Optics* **13**, 054033-054036 (2008).
69. Razansky, D. et al. Multispectral Optoacoustic Tomography of Matrix Metalloproteinase Activity in Vulnerable Human Carotid Plaques. *Molecular Imaging and Biology*, 1-9 (2011).
70. Jain, P.K., Lee, K.S., El-Sayed, I.H. & El-Sayed, M.A. Calculated Absorption and Scattering Properties of Gold Nanoparticles of Different Size, Shape, and

- Composition: Applications in Biological Imaging and Biomedicine. *The Journal of Physical Chemistry B* **110**, 7238-7248 (2006).
71. Nikoobakht, B. & El-Sayed, M.A. Preparation and growth mechanism of gold nanorods (NRs) using seed-mediated growth method. *Chemistry of Materials* **15**, 1957-1962 (2003).
 72. Niidome, T. et al. PEG-modified gold nanorods with a stealth character for in vivo applications. *Journal of Controlled Release* **114**, 343-347 (2006).
 73. Kumar, S., Aaron, J. & Sokolov, K. Directional conjugation of antibodies to nanoparticles for synthesis of multiplexed optical contrast agents with both delivery and targeting moieties. *Nature Protocols* **3**, 314-320 (2008).
 74. Longmire, M., Choyke, P.L. & Kobayashi, H. Clearance properties of nano-sized particles and molecules as imaging agents: considerations and caveats. *Nanomedicine* **3**, 703-717 (2008).
 75. Connor, E.E., Mwamuka, J., Gole, A., Murphy, C.J. & Wyatt, M.D. Gold nanoparticles are taken up by human cells but do not cause acute cytotoxicity. *Small* **1**, 325-327 (2005).
 76. Nicholson, R.I., Gee, J.M. & Harper, M.E. EGFR and cancer prognosis. *Eur J Cancer* **37 Suppl 4**, S9-15 (2001).
 77. Menard, S., Tagliabue, E., Campiglio, M. & Pupa, S.M. Role of HER2 gene overexpression in breast carcinoma. *Journal of cellular physiology* **182**, 150-162 (2000).
 78. Dassonville, O. et al. Expression of epidermal growth factor receptor and survival in upper aerodigestive tract cancer. *Journal of Clinical Oncology* **11**, 1873-1878 (1993).
 79. Pritchard, K.I. et al. HER2 and responsiveness of breast cancer to adjuvant chemotherapy. *New England Journal of Medicine* **354**, 2103-2111 (2006).
 80. Bonner, J.A. et al. Radiotherapy plus cetuximab for squamous-cell carcinoma of the head and neck. *New England Journal of Medicine* **354**, 567-578 (2006).
 81. Vogel, C.L. et al. Efficacy and safety of trastuzumab as a single agent in first-line treatment of HER2-overexpressing metastatic breast cancer. *Journal of Clinical Oncology* **20**, 719-726 (2002).

82. Mallidi, S., Larson, T., Aaron, J., Sokolov, K. & Emelianov, S. Molecular specific optoacoustic imaging with plasmonic nanoparticles. *Opt Express* **15**, 6583-6588 (2007).
83. Mallidi, S. et al. Multiwavelength Photoacoustic Imaging and Plasmon Resonance Coupling of Gold Nanoparticles for Selective Detection of Cancer. *Nano Letters* **9**, 2825-2831 (2009).
84. Aaron, J. et al. Plasmon resonance coupling of metal nanoparticles for molecular imaging of carcinogenesis in vivo. *J Biomed Opt* **12**, 034007 (2007).
85. Aaron, J., Travis, K., Harrison, N. & Sokolov, K. Dynamic imaging of molecular assemblies in live cells based on nanoparticle plasmon resonance coupling. *Nano Lett* **9**, 3612-3618 (2009).
86. Aaron, J.S. et al. Increased optical contrast in imaging of epidermal growth factor receptor using magnetically actuated hybrid gold/iron oxide nanoparticles. *Optics Express* **14**, 12930-12943 (2006).
87. Sokolov, K. et al. Real-Time Vital Optical Imaging of Precancer Using Anti-Epidermal Growth Factor Receptor Antibodies Conjugated to Gold Nanoparticles. *Cancer Research* **63**, 1999-2004 (2003).
88. Li, P.C. et al. In vivo Photoacoustic Molecular Imaging with Simultaneous Multiple Selective Targeting Using Antibody-Conjugated Gold Nanorods. *Optics Express* **16**, 18605-18615 (2008).
89. Gleysteen, J.P. et al. Fluorescent labeled anti-EGFR antibody for identification of regional and distant metastasis in a preclinical xenograft model. *Head Neck* **30**, 782-789 (2008).
90. Kramer-Marek, G., Kiesewetter, D.O. & Capala, J. Changes in HER2 expression in breast cancer xenografts after therapy can be quantified using PET and (18)F-labeled affibody molecules. *Journal of Nuclear Medicine* **50**, 1131-1139 (2009).
91. Li, P.-C. et al., Vol. 6086. (eds. A.O. Alexander & V.W. Lihong) 60860M (SPIE, 2006).
92. Shah, C. et al. Imaging biomarkers predict response to anti-HER2 (ErbB2) therapy in preclinical models of breast cancer. *Clinical Cancer Research* **15**, 4712-4721 (2009).
93. Chen, T.-J. et al. Targeted herceptin-dextran iron oxide nanoparticles for noninvasive imaging of HER2/neu receptors using MRI. *JBIC Journal of Biological Inorganic Chemistry* **14**, 253-260 (2009).

94. Abe, O. et al. Tamoxifen for early breast cancer: an overview of the randomised trials. *Lancet* **351**, 1451-1467 (1998).
95. Reddy, J.A. & Low, P.S. Folate-mediated targeting of therapeutic and imaging agents to cancers. *Critical Reviews™ in Therapeutic Drug Carrier Systems* **15** (1998).
96. Posey, J.A. et al. A pilot trial of Vitaxin, a humanized anti-vitronectin receptor (anti $\alpha v \beta 3$) antibody in patients with metastatic cancer. *Cancer Biotherapy and Radiopharmaceuticals* **16**, 125-132 (2001).
97. Hurwitz, H. et al. Bevacizumab plus irinotecan, fluorouracil, and leucovorin for metastatic colorectal cancer. *New England journal of medicine* **350**, 2335-2342 (2004).
98. Mintun, M. et al. Breast cancer: PET imaging of estrogen receptors. *Radiology* **169**, 45-48 (1988).
99. Ciana, P. et al. In vivo imaging of transcriptionally active estrogen receptors. *Nature medicine* **9**, 82-86 (2002).
100. Chen, W.-T., Khazaie, K., Zhang, G., Weissleder, R. & Tung, C.-H. Detection of dysplastic intestinal adenomas using a fluorescent folate imaging probe. *Molecular Imaging* **4**, 67 (2005).
101. Choi, H., Choi, S.R., Zhou, R., Kung, H.F. & Chen, I. Iron oxide nanoparticles as magnetic resonance contrast agent for tumor imaging via folate receptor-targeted delivery< sup> 1</sup>. *Academic radiology* **11**, 996-1004 (2004).
102. Backer, M.V. et al. Molecular imaging of VEGF receptors in angiogenic vasculature with single-chain VEGF-based probes. *Nature medicine* **13**, 504-509 (2007).
103. Nagengast, W.B. et al. In vivo VEGF imaging with radiolabeled bevacizumab in a human ovarian tumor xenograft. *Journal of Nuclear Medicine* **48**, 1313-1319 (2007).
104. Savariar, E.N. et al. Real-time In Vivo Molecular Detection of Primary Tumors and Metastases with Ratiometric Activatable Cell-Penetrating Peptides. *Cancer research* **73**, 855-864 (2013).
105. Egeblad, M. & Werb, Z. New functions for the matrix metalloproteinases in cancer progression. *Nat Rev Cancer* **2**, 161-174 (2002).

106. Fingleton, B. in *Seminars in cell & developmental biology*, Vol. 19 61-68 (Elsevier, 2008).
107. Levi, J. et al. Design, Synthesis, and Imaging of an Activatable Photoacoustic Probe. *Journal of the American Chemical Society* **132**, 11264-11269 (2010).
108. Ajisaka, H., Yonemura, Y. & Miwa, K. Correlation of lymph node metastases and expression of matrix metalloproteinase-7 in patients with gastric cancer. *Hepatology* **51**, 900-905 (2004).
109. Daniele, A. et al. Expression of Metalloproteinases MMP-2 and MMP-9 in Sentinel Lymph Node and Serum of Patients with Metastatic and Non-Metastatic Breast Cancer. *Anticancer Research* **30**, 3521-3527 (2010).
110. Kurahara, S. et al. Expression of MMPS, MT-MMP, and TIMPs in squamous cell carcinoma of the oral cavity: correlations with tumor invasion and metastasis. *Head Neck* **21**, 627-638 (1999).
111. Zhang, J., Yang, P.L. & Gray, N.S. Targeting cancer with small molecule kinase inhibitors. *Nature Reviews Cancer* **9**, 28-39 (2009).
112. Lievre, A. et al. KRAS mutation status is predictive of response to cetuximab therapy in colorectal cancer. *Cancer research* **66**, 3992-3995 (2006).
113. Wang, Y. et al. Visualizing the mechanical activation of Src. *Nature* **434**, 1040-1045 (2005).
114. Sugahara, K.N. et al. Coadministration of a tumor-penetrating peptide enhances the efficacy of cancer drugs. *science* **328**, 1031-1035 (2010).
115. Mehlen, P. & Puisieux, A. Metastasis: a question of life or death. *Nature Reviews Cancer* **6**, 449-458 (2006).
116. , Vol. 2013 (National Cancer Institute, www.cancer.gov/cancertopics/factsheet/detection/staging).
117. Cochran, A.J., Roberts, A.A. & Saida, T. The place of lymphatic mapping and sentinel node biopsy in oncology. *International journal of clinical oncology* **8**, 139-150 (2003).
118. Stoeckli, S.J., Steinert, H., Pfaltz, M. & Schmid, S. Sentinel Lymph Node Evaluation in Squamous Cell Carcinoma of the Head and Neck. *Otolaryngology - Head and Neck Surgery* **125**, 221-226 (2001).

119. Veronesi, U. et al. Sentinel-node biopsy to avoid axillary dissection in breast cancer with clinically negative lymph-nodes. *Lancet* **349**, 1864-1867 (1997).
120. Gershenwald, J.E. et al. Multi-Institutional Melanoma Lymphatic Mapping Experience: The Prognostic Value of Sentinel Lymph Node Status in 612 Stage I or II Melanoma Patients. *Journal of Clinical Oncology* **17**, 976 (1999).
121. Goldberg, J., Riedel, E., Morrow, M. & Van Zee, K. Morbidity of Sentinel Node Biopsy: Relationship Between Number of Excised Lymph Nodes and Patient Perceptions of Lymphedema. *Annals of Surgical Oncology* **18**, 2866-2872 (2011).
122. Langer, I. et al. Morbidity of Sentinel Lymph Node Biopsy (SLN) Alone Versus SLN and Completion Axillary Lymph Node Dissection After Breast Cancer Surgery: A Prospective Swiss Multicenter Study on 659 Patients. *Annals of Surgery* **245**, 452-461 (2007).
123. Scoggins, C.R. et al. Factors associated with false-negative sentinel lymph node biopsy in melanoma patients. *Annals of surgical oncology* **17**, 709-717 (2010).
124. Cohen, S.M., Fishinghawk, B.G. & Cohen, M.S. Translational imaging of lymphatics in cancer. *Advanced Drug Delivery Reviews* **63**, 956-962 (2011).
125. Wunderbaldinger, P. Problems and prospects of modern lymph node imaging. *European Journal of Radiology* **58**, 325-337 (2006).
126. Kobayashi, H. et al. Lymphatic drainage imaging of breast cancer in mice by micro-magnetic resonance lymphangiography using a nano-size paramagnetic contrast agent. *Journal of the National Cancer Institute* **96**, 703-708 (2004).
127. Goldberg, B.B. et al. Sentinel Lymph Nodes in a Swine Model with Melanoma: Contrast-enhanced Lymphatic US1. *Radiology* **230**, 727-734 (2004).
128. Oh, M.H. et al. Large-scale synthesis of bioinert tantalum oxide nanoparticles for X-ray computed tomography imaging and bimodal image-guided sentinel lymph node mapping. *Journal of the American Chemical Society* **133**, 5508-5515 (2011).
129. Richards, P.S. & Peacock, T.E. The role of ultrasound in the detection of cervical lymph node metastases in clinically N0 squamous cell carcinoma of the head and neck. *Cancer Imaging* **7**, 167-178 (2007).
130. Wagner, J.D. et al. FDG-PET sensitivity for melanoma lymph node metastases is dependent on tumor volume. *Journal of surgical oncology* **77**, 237-242 (2001).
131. Kyzas, P.A., Evangelou, E., Denaxa-Kyza, D. & Ioannidis, J.P. 18F-fluorodeoxyglucose positron emission tomography to evaluate cervical node

- metastases in patients with head and neck squamous cell carcinoma: a meta-analysis. *Journal of the National Cancer Institute* **100**, 712-720 (2008).
132. Harisinghani, M.G. et al. Noninvasive detection of clinically occult lymph-node metastases in prostate cancer. *New England Journal of Medicine* **348**, 2491-2499 (2003).

Chapter 2: Label-Free Detection of Lymph Node Metastasis with Functional Spectroscopic Photoacoustic Imaging

2.1 INTRODUCTION

Over 90% of cancer deaths can be attributed directly or indirectly to metastases rather than the primary tumor.¹ The ability to reliably detect the spread of malignant cells can dramatically improve a physician's ability to devise a treatment plan. In many types of cancer, including skin, head and neck, breast, and gastrointestinal, the presence of cancerous cells in the regional lymph nodes is a harbinger of distant metastasis. Therefore, a sentinel lymph node (SLN) biopsy is commonly performed to detect the spread of cancer cells throughout the lymphatics.²⁻⁵ The SLN biopsy procedure offers a less invasive alternative to elective regional lymph node dissection with lower rates of morbidity and comparable survival rates.⁶ Furthermore, it is more likely to correctly identify tumor bearing nodes.⁷ Because of these benefits, this procedure has gained widespread acceptance in the clinical community.

Sentinel lymph node biopsies are performed after a primary tumor is detected. First, a blue dye and/or radioactive tracer are injected peritumorally to identify the SLN – the first lymph node to which a tumor drains – and guide the rest of the surgery. A preoperative lymphoscintigraphy or SPECT/CT scan can be used to plan the procedure, while a gamma probe or Geiger counter and visual inspection of the blue dye is used for intraoperative guidance. The surgeon typically removes all stained nodes for pathological evaluation.

Despite the advantages of SLN biopsy, the procedure still suffers from nontrivial morbidity, it requires the injection of a radioactive material, the efficacy is subject to the skill of the surgeon and pathologist, and patients must wait for up to several days to

weeks to receive the results. These shortcomings have prompted a number of investigators to develop imaging procedures to improve the accuracy of the procedure, remove the need for the radioactive compound, or noninvasively detect metastases.^{8, 9} These imaging modalities include magnetic resonance imaging (MRI),¹⁰ positron emission tomography (PET),¹¹ ultrasound (US) imaging,^{12, 13} fluorescence imaging,¹⁴ and photoacoustic (PA) imaging.¹⁵⁻¹⁹ Image guidance has the potential to improve localization of the SLN, decrease morbidity and provide indirect indicators of metastasis.

In spite of the promise that these imaging techniques have shown for improving the SLN biopsy procedure, they have yet to gain clinical acceptance. One reason is that they often require administration of a contrast agent. This serves to lengthen the translation process. In addition, an improvement to diagnostic accuracy, patient outcome, or patient morbidity is yet to be demonstrated, though there is high likelihood that imaging could improve all three. Finally, the sensitivity and specificity of the detection of SLN metastasis with imaging has not yet warranted the replacement of the SLN biopsy.

In this chapter, the concept of using label-free spectroscopic photoacoustic (sPA) imaging for the noninvasive detection of SLN metastasis is investigated. The detection is based on functional changes that are observed in the lymph nodes (i.e., hypoxia) as they are invaded with malignant cells. Decreased oxygen saturation resulting from sub-millimeter metastases enveloping 1% or less of the volume of the SLN was observed using sPA imaging. These results suggest that sPA imaging may be able to accurately detect SLN metastasis without resorting to the invasive biopsy procedure. Furthermore, sPA imaging could easily be coupled to US imaging to provide a comprehensive functional and anatomical picture of the regional lymph nodes.

2.2 MATERIALS AND METHODS

All animal studies were performed following protocols approved by the Institutional Animal Care and Use Committee (IACUC) at The University of Texas at Austin. An orthotopic mouse model of squamous cell carcinoma of the oral cavity (SCCOC) first described by Myers, et al. was used for these studies.²⁰ Female Nu/Nu homozygous mice of age 57-70 days (Charles River Laboratories, strain code 088) were inoculated with FaDu cells which had been transfected with Luciferase (graciously provided by the lab of Dr. Jeffrey Myers) via a submucosal injection in the tongue. Additional details on the mouse model can be found in Appendix A. The primary tumors were allowed to grow in the tongues of the mice for 2-4 weeks, until they were approximately 3-5 mm in diameter. At this point there is high likelihood of metastasis to one or more cervical lymph nodes.

Once the tumor had reached the appropriate size, the mice underwent combined US and sPA imaging while anesthetized with isoflurane (1.5-2%). A Vevo LAZR high frequency US and PA imaging system (VisualSonics) equipped with a linear array transducer (LZ-550, 40 MHz center frequency) was used to acquire all PA and US images. The co-registered spatial dimensions of the collected US and PA images were 14 mm (width) by 15 mm (depth). US and PA images at each optical wavelength covering three-dimensional (3-D) volumes surrounding the cervical LNs were acquired by scanning the US transducer in the elevational direction with a step size of 76 μm . The laser was tuned to optical wavelengths of 680, 700, 720, 740, 760, 780, 800, 820, 840, and 860 nm. Laser fluences, measured by a Nova II power meter with a PE50BB sensor (Ophir), were 10-20 mJ/cm^2 ; all laser energies were below the American National Standards Institute safe exposure level for human skin. Photoacoustic images were averaged 8 times, thus suppressing uncorrelated noise. Each PA image was normalized

by the measured fluence of each pulse to correct for the wavelength-dependent and pulse-to-pulse laser energy variations.

After US/sPA imaging, bioluminescence imaging was used to identify metastases and guide the resection of the lymph nodes. An IVIS Spectrum (Perkin Elmer) with an open filter collected bioluminescence images for 10-15 minutes following the intraperitoneal injection of 100 μ L of RediJect Luciferase (Perkin Elmer). The mice were then euthanized via an overdose of isoflurane (5%) and cervical dislocation. Continued bioluminescence imaging during dissection allowed for the accurate removal the primary tumor and all metastases. The samples were fixed in a 1:10 buffered dilution of formalin (Fisher Scientific) for 24-48 hours then transferred to 70% ethanol. All histological processing was performed at the Integrated Imaging, Pathology, & Histology Facility Core at The University of Texas MD Anderson Cancer Center Science Park location. After being embedded in paraffin, the lymph nodes were sliced in 100 μ m levels and stained with a hematoxylin & eosin stain to allow for the identification of metastases. A Leica DMI 3000B microscope with a 10x objective coupled to a DFC 290 camera was used to record color images of the histology.

The 10 single-wavelength PA images were processed using a custom Matlab routine. The hemoglobin was taken to be the dominant absorber in the tissue, so only two absorption spectra were considered for sPA imaging: deoxygenated hemoglobin (Hb) and oxygenated hemoglobin (Hb_{O₂}). The absorption spectra were obtained from literature.²¹ A linear least squared error method was used to estimate the relative concentrations of Hb and Hb_{O₂}.²²

Analysis of the SO₂ in the nodes was performed under the guidance of the US images. The lymph nodes were segmented manually in the US images using Amira three-dimensional visualization software. The SO₂ in every pixel in each lymph node was

analyzed to observe the distribution of oxygen. The average SO_2 throughout each normal and metastatic node was compared using a one-way t-test. An ROC curve was constructed using the average SO_2 throughout the nodes and the sensitivity and specificity were derived from the curve.

2.3 RESULTS AND DISCUSSION

The progression of a metastatic focus in the SLN can be observed with US/sPA imaging (Figure 2.1). The cervical lymph nodes which have not been invaded by metastatic cells typically contain a large amount of oxygenated blood (Figure 2.1a-b). Indeed, the level of oxygenation is much higher than in the nearby tissue. Histology from these normal lymph nodes shows the typical morphology of lymph node cells (Figure 2.1c).

No qualitative changes in the functional sPA images were observed when the primary tumor spread to regions near, but not in, the lymph node (Figure 2.1d-f). In this case, the metastases were typically observed in the afferent lymph vessel (Figure 2.1f, arrows). Similar results were seen when a small micrometastasis (ca. 50 μm) formed on the border of the lymph node (Figure 2.1g-i). However, when the metastasis exceeded 300 μm (Figure 2.1j-o) significant functional changes can be observed. The metastatic nodes exhibited a large drop in SO_2 . In nodes harboring larger metastases, morphological changes in the node were also observed (Figure 2.1m-n). Specifically, the nodes became larger and more rounded. In addition, a hypoechoic region developed in the US image of the node and this same region experienced lower levels of SO_2 than the rest of the node. This correlates with previous studies which report decreased echogenicity resulting from metastasis.¹³

A three-dimensional scan of the lymph node shown in Figure 2.1m-o was performed (Figure 2.2). The images show that a localized hypoxic region persists throughout much of the node. This region is co-localized with a hypoechoic region in the US image. Furthermore, the size of this region is consistent with the amount of nodal invasion observed in histology (Figure 2.1o). These results indicate that combined US and sPA imaging may be able to provide physicians with a clear view of metastatic lymph nodes.

When 31 lymph nodes from 17 mice were analyzed (Figure 2.3a), metastatic nodes ($N = 8$) experienced a statistically significant decrease in SO_2 when compared to either normal nodes ($N = 17$, $p = 0.0029$) or nodes with nearby metastases ($N = 7$, $p = 0.012$). A histogram of the SO_2 in a normal or metastatic node (Figure 2.3b) shows that the observed hypoxia is a result of decreased oxygen throughout the entire node. This indicates that not only do the tumor cells decrease the SO_2 through their enhanced metabolism,²³ but they also disrupt the normal function of the node, leading to large-scale functional changes. In fact, these functional changes are observed even in metastases as small as $180 \mu\text{m}$ (Figure 2.3c). Furthermore, the level of hypoxia is inversely related to the size of the metastasis.

Overall, the average level of SO_2 in the lymph node provides a good metric to identify metastases (Figure 2.3d). In these initial preclinical experiments, a sensitivity of 75% and specificity of 78% was achieved. The area under the ROC was 0.842. This indicates that a metastatic node will exhibit a lower SO_2 than a normal node 84% of the time. In spite of the overall positive results, there are limitations to this approach. Metastases smaller than $150 \mu\text{m}$ were not detected by measuring the SO_2 in the node. Furthermore, metastases forming in the afferent lymphatic vessel did not lead to measurable functional changes. A more precise method is needed to detect the smaller,

elusive metastases. However, it is worthwhile to note that detectable functional changes occurred even when metastases only invaded 1% of the entire lymph node volume. This indicates the sPA imaging may be able to detect the spread of cancer long before the metastases are palpable.

The misclassifications that were observed in these experiments could be a function of mouse-to-mouse variability in nodal SO_2 . Future studies could analyze several normal lymph nodes in each mouse in relation to the metastatic node(s). The future clinical screening procedure could involve scanning several regional nodes and identifying hypoxic nodes for further histological analysis.

2.4 CONCLUSIONS

Determining the extent of the spread of cancer throughout the regional lymph nodes is critical for the effective treatment of many types of cancer. The results presented here show that sPA imaging has the potential to noninvasively detect the functional changes that arise from micrometastases in the regional nodes. Because of the synergy between US and PA imaging, the two modalities could be combined to simultaneously visualize SO_2 , blood flow, and node morphology. The combination of the two modalities could potentially improve the overall sensitivity and specificity.

The greatest benefit of this technique is that it does not require the use of a contrast agent; the nodes can be scanned in an entirely noninvasive manner. This greatly facilitates the timely transition of this technology into the clinic. Because safe levels of non-ionizing radiation are used, there are no foreseeable health concerns with this approach. The initial preclinical results indicate that further studies in the clinical realm are warranted.

Although the method is appealing because it can be performed in real-time without the use of contrast agents or ionizing radiation, its inability to identify small metastases outside the lymph nodes suggests another approach is needed. In the next chapter, a molecularly-activatable plasmonic nanosensor is used to increase the sensitivity and specificity of sPA detection of micrometastases.

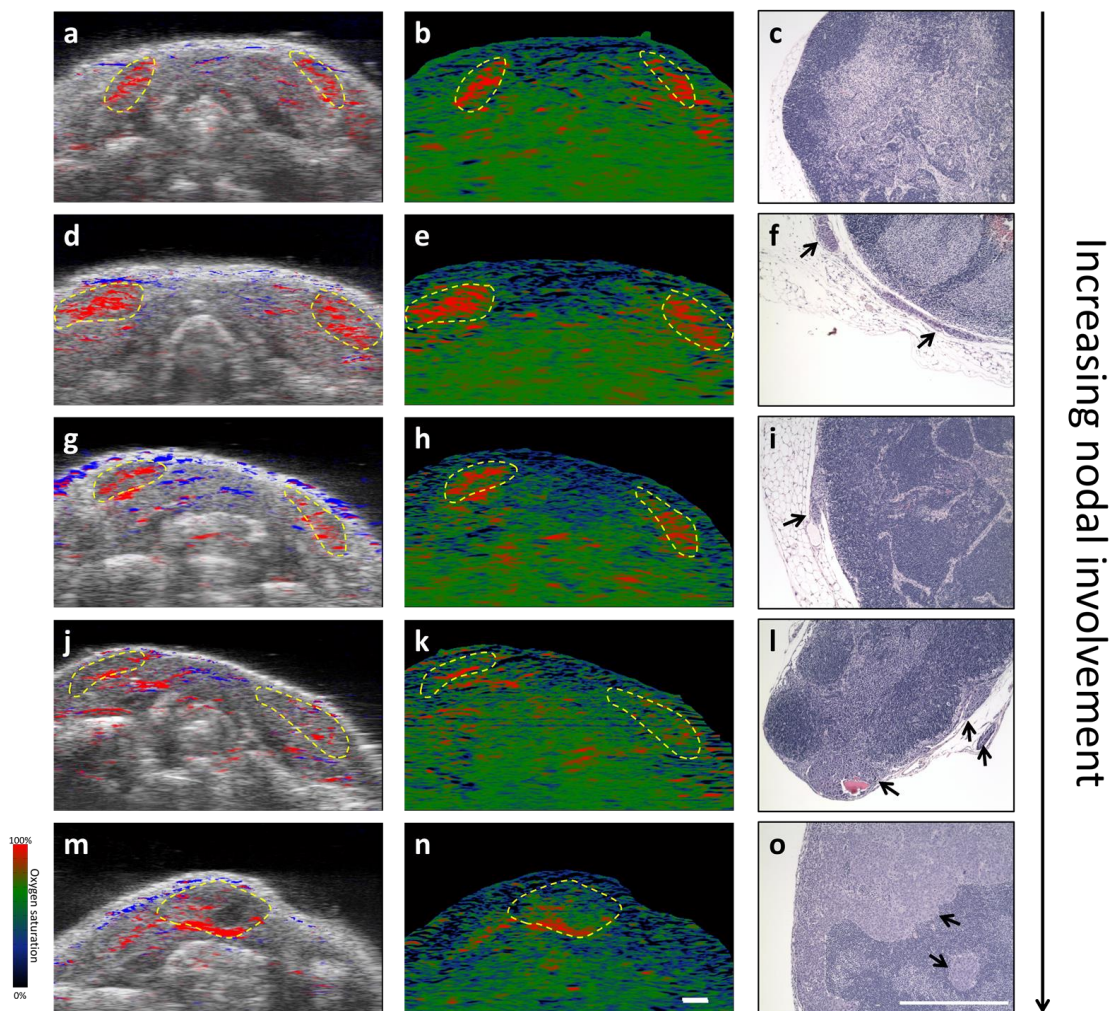


Figure 2.1 a, d, g, j, m) Combined US and sPA images showing lymph nodes from five mice (outlined in yellow) and the surrounding oxygenated (red) and deoxygenated (blue) blood, b, e, h, k, n) parametric SO_2 maps showing the level of oxygenation throughout the same two-dimensional slice (scale bar = 1 mm), and c, f, i, l, o) H&E stains of a lymph node from each mouse (scale bar = 500 μm). Images correspond to a mouse without SLN metastases (a-c), a mouse with metastasis near the SLN (d-f), and three mice with increasing spread of metastases throughout the SLN (g-i), (j-l), and (m-o).

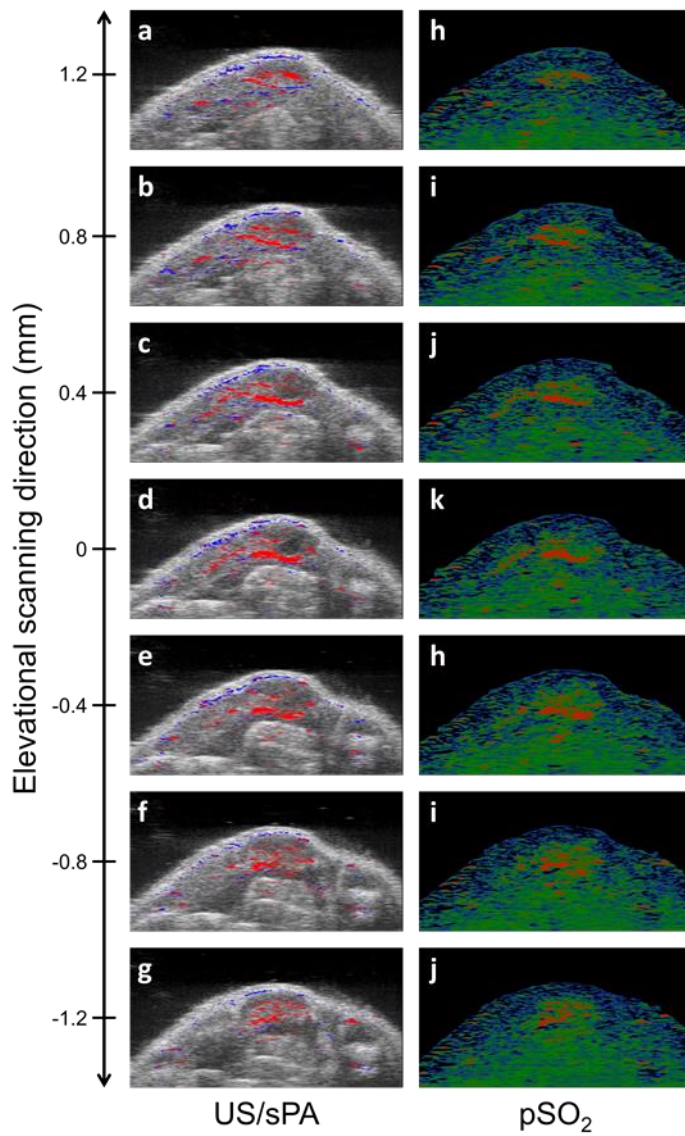


Figure 2.2 a-g) Combined US and sPA images of two-dimensional slices spanning a 2.4-mm three-dimensional volume containing a single metastatic lymph node. h-j) A parametric SO_2 map shows that lymph node is hypoxic throughout much of its volume.

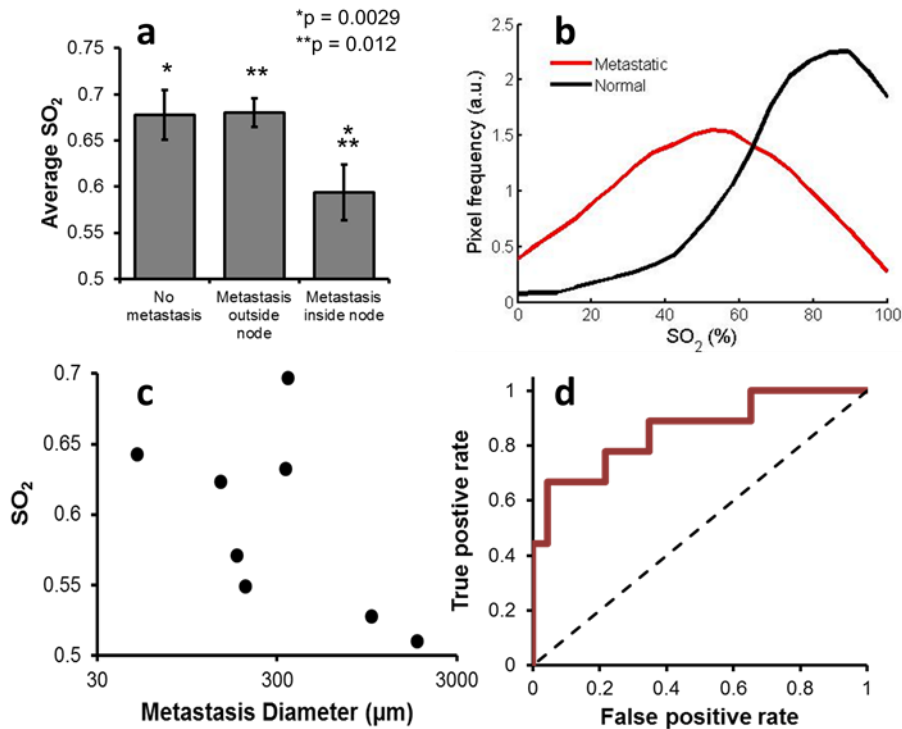


Figure 2.3 a) Lymph nodes with metastases (N = 8 nodes) exhibited statistically significant decreases in SO_2 when compared to either normal nodes (N = 17 nodes, p = 0.0029) or nodes with nearby metastases (N = 6 nodes, p = 0.012). b) A histogram of the SO_2 in the pixels in the LN of a metastatic node (red) shows a significantly different distribution than a normal node (black). c) An ROC curve shows the predictive power of lymph node SO_2 as an indicator of metastasis (red). The black dashed line corresponds to random chance. d) The lymph node SO_2 correlates negatively with metastasis size.

2.5 REFERENCES

1. Sleeman, J. & Steeg, P.S. Cancer metastasis as a therapeutic target. *European Journal of Cancer* **46**, 1177-1180 (2010).
2. Bergkvist, L. & Frisell, J. Multicentre validation study of sentinel node biopsy for staging in breast cancer. *British Journal of Surgery* **92**, 1221-1224 (2005).
3. Cochran, A.J., Roberts, A.A. & Saida, T. The place of lymphatic mapping and sentinel node biopsy in oncology. *International journal of clinical oncology* **8**, 139-150 (2003).
4. Morton, D.L. et al. Sentinel-node biopsy or nodal observation in melanoma. *New England Journal of Medicine* **355**, 1307-1317 (2006).
5. Stoeckli, S.J., Steinert, H., Pfaltz, M. & Schmid, S. Sentinel Lymph Node Evaluation in Squamous Cell Carcinoma of the Head and Neck. *Otolaryngology - Head and Neck Surgery* **125**, 221-226 (2001).
6. Langer, I. et al. Morbidity of Sentinel Lymph Node Biopsy (SLN) Alone Versus SLN and Completion Axillary Lymph Node Dissection After Breast Cancer Surgery: A Prospective Swiss Multicenter Study on 659 Patients. *Annals of Surgery* **245**, 452-461 (2007).
7. Gershenwald, J.E. et al. Patterns of recurrence following a negative sentinel lymph node biopsy in 243 patients with stage I or II melanoma. *Journal of clinical oncology* **16**, 2253-2260 (1998).
8. Cohen, S.M., FISHINGHAWK, B.G. & COHEN, M.S. Translational imaging of lymphatics in cancer. *Advanced Drug Delivery Reviews* **63**, 956-962 (2011).
9. Wunderbaldinger, P. Problems and prospects of modern lymph node imaging. *European Journal of Radiology* **58**, 325-337 (2006).
10. Harisinghani, M.G. et al. Noninvasive detection of clinically occult lymph-node metastases in prostate cancer. *New England Journal of Medicine* **348**, 2491-2499 (2003).
11. Wagner, J.D. et al. FDG-PET sensitivity for melanoma lymph node metastases is dependent on tumor volume. *Journal of surgical oncology* **77**, 237-242 (2001).
12. Goldberg, B.B. et al. Sentinel Lymph Nodes in a Swine Model with Melanoma: Contrast-enhanced Lymphatic US1. *Radiology* **230**, 727-734 (2004).

13. Richards, P.S. & Peacock, T.E. The role of ultrasound in the detection of cervical lymph node metastases in clinically N0 squamous cell carcinoma of the head and neck. *Cancer Imaging* **7**, 167-178 (2007).
14. Savariar, E.N. et al. Real-time In Vivo Molecular Detection of Primary Tumors and Metastases with Ratiometric Activatable Cell-Penetrating Peptides. *Cancer research* **73**, 855-864 (2013).
15. Cai, X. et al. In vivo quantitative evaluation of the transport kinetics of gold nanocages in a lymphatic system by noninvasive photoacoustic tomography. *ACS Nano* **5**, 9658-9667 (2011).
16. Pan, D. et al. Near infrared photoacoustic detection of sentinel lymph nodes with gold nanobeacons. *Biomaterials* **31**, 4088-4093 (2010).
17. Song, K.H., Kim, C., Cobley, C.M., Xia, Y. & Wang, L.V. Near-Infrared Gold Nanocages as a New Class of Tracers for Photoacoustic Sentinel Lymph Node Mapping on a Rat Model. *Nano Letters* **9**, 183-188 (2008).
18. Song, K.H., Kim, C., Maslov, K. & Wang, L.V. Noninvasive in vivo spectroscopic nanorod-contrast photoacoustic mapping of sentinel lymph nodes. *European Journal of Radiology* **70**, 227-231 (2009).
19. Song, K.H., Stein, E.W., Margenthaler, J.A. & Wang, L.V. Noninvasive photoacoustic identification of sentinel lymph nodes containing methylene blue in vivo in a rat model. *Journal of Biomedical Optics* **13**, 054033-054036 (2008).
20. Myers, J.N., Holsinger, F.C., Jasser, S.A., Bekele, B.N. & Fidler, I.J. An Orthotopic Nude Mouse Model of Oral Tongue Squamous Cell Carcinoma. *Clinical Cancer Research* **8**, 293-298 (2002).
21. Prael, S. (Oregon Medical Laser Center, 2011).
22. Kim, S., Chen, Y.-S., Luke, G.P. & Emelianov, S.Y. In vivo three-dimensional spectroscopic photoacoustic imaging for monitoring nanoparticle delivery. *Biomed. Opt. Express* **2**, 2540-2550 (2011).
23. Vander Heiden, M.G., Cantley, L.C. & Thompson, C.B. Understanding the Warburg effect: the metabolic requirements of cell proliferation. *Science* **324**, 1029-1033 (2009).

Chapter 3: Detection of Micrometastases with Spectroscopic Photoacoustic Imaging of Molecularly-activated Plasmonic Nanosensors

3.1 INTRODUCTION

Accurate detection of regional lymph node (LN) metastases is a critical step in staging, prognosis, and development of a treatment plan for cancer patients¹⁻³. Lymphatic mapping with sentinel lymph node (SLN) biopsy has been introduced as an alternative to elective LN dissection and gained rapid acceptance because it allowed improved accuracy and decreased patient morbidity for regional cancer staging^{4, 5}. The fact that nodes test positive for tumors a minority of the time (for example, 15% for melanoma¹) makes it even more desirable to perform the procedure. However, SLN biopsy still has major limitations. It requires two or more injections of radionuclide tracers and/or dye. If multiple injections are used, two different LNs may be identified as the SLN. In addition, it is an invasive surgical procedure with associated risks of short and long term morbidity, and up to two weeks of waiting for full histopathology evaluation.^{6, 7} Furthermore, the detection limits for pathologic identification of metastatic cells remain subject to the skill and patience of the pathologist.

A variety of imaging techniques – including US imaging, fluorescence, magnetic resonance imaging (MRI), positron-emission tomography (PET), and computed tomography (CT) – have been tested in clinical patients in attempts to improve the accuracy and safety of SLN biopsy⁸⁻¹³. Although these imaging modalities can provide useful morphological (e.g., SLN size and shape) and functional (e.g., blood flow or nanoparticle drainage) information⁹, they do not have sufficient sensitivity and specificity to replace the current invasive SLN procedure^{11, 12}. Photoacoustic (PA) imaging has recently been introduced as a modality that can improve the detection threshold and

sensitivity of radiographic imaging modalities¹⁴⁻¹⁹. It was shown that PA imaging can be used to accurately track intradermally-injected dyes or nanoparticles for localization of LNs with high sensitivity^{20, 21}. Although the previously proposed image-guided methods show promise for increasing the accuracy of LN mapping while eliminating the use of radioactive compounds, they still require surgical removal and histopathological evaluation of the SLNs.

This chapter presents a new approach that is based on molecular detection of LN metastases using spectroscopic photoacoustic (sPA) imaging with molecularly-activated plasmonic nanosensors (MAPS). These MAPS can be used in *in vivo* applications where signal due to delivery of a contrast agent hinders the ability to visualize molecular expressions. Experiments in the orthotopic nude mouse model of squamous cell carcinoma of the oral cavity (SCCOC) that develops LN micrometastases²² show that this method requires only a single peritumoral injection of MAPS which drain through the lymphatics and specifically interact with metastatic cells; these interactions drastically change optical properties of MAPS. US imaging provides detailed anatomic information about the location and morphology of LNs, while highly sensitive sPA imaging can detect optical changes associated with MAPS labeling of metastatic cells thus allowing real-time detection of micrometastases in the LNs.

3.2 MATERIALS AND METHODS

3.2.1 Nanoparticle Synthesis

Molecular targeted AuNPs were synthesized as previously described²³. First, 40 nm spherical AuNPs were prepared by heating 100 mL of a 0.01% (w/v) water solution of chloroauric acid (HAuCl₄, Sigma-Aldrich) to boiling, and rapidly adding 4 mL of a 1% (w/v) solution of sodium citrate. The reaction mixture becomes purple-red within few

minutes indicating synthesis of AuNPs. Then, anti-EGFR or anti-RG16 monoclonal antibodies (clone C225 or RG16, Sigma-Aldrich) were attached to the AuNPs using directional conjugation chemistry that utilizes a carbohydrate chain on the Fc portion of the antibody leaving antigen binding sites on the Fab moiety available for targeting²³. Briefly, antibodies at 1 mg/mL in 40 mM HEPES buffer, pH 7.5 and 100 mM sodium periodate (NaIO₄, Sigma-Aldrich) were mixed at 10:1 (v/v) ratio, respectively, and were incubated for 30 minutes in dark at room temperature. This reaction results in oxidation of hydroxyl moieties in the Fc antibody regions to aldehyde groups. Then, approximately 100 fold molar excess of a heterofunctional linker (dithiolaromatic-PEG6k-CONHNH₂, SensoPath Technologies) was added to the oxidized antibodies for 1 hour. The hydrazide portion of the linker reacts with aldehydes to form a stable linkage. The antibody-linker complexes were purified using a 100,000 MWCO centrifugal filter (Millipore). After purification, the modified antibodies were resuspended in 40 mM HEPES (pH 7.4) at concentration of 0.1 mg/mL and were mixed with as prepared AuNPs at 1:10 antibody/nanoparticle (v/v) ratio for 20 minutes at RT. During this step a stable bond is formed between the gold surface and the linker's thiol groups. Subsequently, 10⁻⁵ M 1x saline PBS solution of methoxy-poly(ethylene-glycol)thiol (mPEG-SH, 14 kD, Shearwater Polymers) was added at *ca.* 1:10 mPEG-SH to nanoparticle ratio (v/v) for 20 minutes to passivate the surface of nanoparticle conjugates that is not covered by antibodies. The final conjugates were washed using centrifugation (4000 rpm, 30 minutes) and were resuspended in 1x saline PBS at concentration of *ca.* 1 x 10¹² nanoparticles/mL.

3.2.2 Animal Studies

All animal studies were approved by the Institutional Animal Care and Use Committee at the University of Texas at Austin. Female Nu/Nu nude mice of 2 months of age were used in this study (Charles River Laboratories, strain code 88). The primary tumors were initiated with a submucosal injection of 300,000 FaDu-Luciferase cells suspended in 30 μ L of DMEM media into the tongue. The tumors were allowed to grow to 3-4 mm in diameter before the imaging experiments were performed. At this point 82% of the inoculated mice in the studies developed metastases in the lymphatics²².

During US and PA imaging, the mice were anesthetized with isoflurane (1.5%, 0.5 L/min O₂). Heart rate, respiration rate, and body temperature were monitored using a heated electrocardiogram pad. The mice were imaged prior to the injection of nanoparticles. Forty microliters of sterile filtered nanoparticle solution were injected peritumorally immediately after the first imaging session while the mice were still under anesthesia. The total injected dose was 1.6 pmol of nanoparticles that is equivalent to 40 μ g of gold. This dose is significantly below previously reported thresholds for any observed adverse effects in vitro or in vivo.²⁴ Imaging was performed continuously for two hours following the injection of nanoparticles.

Following the US and PA imaging, the bioluminescent cancer cells in the mice were imaged using an IVIS Spectrum (PerkinElmer). Once anesthetized with isoflurane, the mice were injected with 100 μ L of RediJect D-Luciferin (PerkinElmer). Bioluminescence imaging was performed for 10-15 minutes following the injection. Then mice were euthanized by an overdose of isoflurane and cervical dislocation. Bioluminescence imaging was performed to guide the resection of the primary tumor and metastases. The primary tumor and cervical LNs were fixed in 10% formalin for 24 hours

and, then, were transferred to 70% ethanol. Samples were then embedded in paraffin for histological analysis. No randomization or blinding were used in the animal studies.

3.2.3 Photoacoustic and Ultrasound Imaging

A Vevo LAZR high frequency US and PA imaging system (VisualSonics) equipped with a linear array transducer (LZ-550, 40 MHz center frequency) was used to acquire all PA and US images. The co-registered spatial dimensions of the collected US and PA images were 14 mm (width) by 15 mm (depth). US and PA images at each optical wavelength covering three-dimensional (3-D) volumes surrounding the cervical LNs were acquired by scanning the US transducer in the elevational direction with a step size of 76 μm . The laser was tuned to optical wavelengths of 680, 700, 720, 740, 760, 780, 800, 820, 840, and 860 nm. Laser fluences, as measured by a Nova II power meter with a PE50BB sensor (Ophir), were 10-20 mJ/cm^2 ; all laser energies were below the American National Standards Institute safe exposure level for human skin. Photoacoustic images were averaged 8 times, thus suppressing uncorrelated noise. Each PA image was normalized by the measured fluence of each pulse to correct for the wavelength-dependent and pulse-to-pulse laser energy variations.

To resolve different types of optical absorbers, an ultrasound-guided sPA imaging algorithm was developed (Figure 3.1). Analysis was restricted to the three predominant absorbers in the lymph nodes of the mice: oxygenated hemoglobin (HbO_2), deoxygenated hemoglobin (Hb), and activated MAPS (Figure 3.1a-b). The US image was used to automatically segment the mouse to remove PA imaging artifacts on the surface of the skin. The relative contributions of Hb, HbO_2 , and MAPS to the overall PA signal – $s\text{PA}_{\text{Hb}}$, $s\text{PA}_{\text{HbO}_2}$, and $s\text{PA}_{\text{MAPS}}$, respectively – in each pixel was estimated using a previously developed linear least squares method (Figure 3.1c-e)²⁵. Pixels containing negative

concentrations (an artifact resulting from noise or the presence of absorbers other than Hb_{O2}, Hb, and MAPS) were not displayed. Spectroscopic photoacoustic images were displayed using blue, red, and yellow color maps for sPA_{Hb}, sPA_{HbO2}, and sPA_{MAPS}, respectively.

3.2.4 Statistical Analysis

The SLNs were identified and segmented using the 3-D visualization of US data. Only the signal within 300 μm of the LNs was considered. In order to suppress the PA signal from blood, the following formula was used to measure the presence of activated MAPS in each LN: $sPA_{MAPS} = (PA_{680} - PA_{760})/PA_{760}$. The normalization by PA_{760} accentuates the differences between the spectra of activated MAPS and Hb (Figure 3.1b). After discarding pixels below a threshold that was proportional to the ratio of absorption of anti-EGFR AuNPs at 680 nm to 530 nm (to account for small variations in particle batches), the sPA_{MAPS} signal in each LN was summed in each segmented volume corresponding to the LN. A Lilliefors test was used to determine that the sPA_{MAPS} signal in the LNs did not follow a normal distribution. A nonparametric Mann-Whitney U test was used to test the hypothesis that the sPA_{MAPS} signal in metastatic nodes was not significantly greater than the controls. A value of $p < 0.05$ was taken to imply statistically significant difference between the groups. All lymph nodes from mice injected with EGFR-targeted MAPS were used to evaluate the sensitivity and specificity of the imaging technique (RG16-targeted MAPS were excluded from this analysis). An ROC curve constructed from the sPA_{MAPS} signal was used to determine the threshold for sensitivity and specificity. The number of lymph nodes analyzed in this study were chosen by analyzing the power of the Mann-Whitney U test. If it is assumed that a 50% increase in

signal is observed in metastatic nodes, then 5 nodes per group are needed to achieve a power of 95%.

3.2.5 Histology and Optical Imaging

Paraffinized samples were stained using hematoxylin and eosin (H&E) stain to show tissue morphology, silver stain to detect gold and anti-EGFR rabbit polyclonal antibodies (Sigma HPA018530) for molecular specific identification of metastatic cells. A Leica DMI 3000B microscope coupled to a DFC 290 camera was used to record color images.

Dark-field and hyperspectral imaging were performed on a Leica DM 6000 microscope with a 20x objective and xenon lamp. Hyperspectral imaging was carried out with PARISS® system (Lightform, Inc.) attached to the Leica DM 6000 microscope. The spatial resolution of the system is 1.25 μm at 20x magnification, and the spectral resolution is 1-3 nm. The system was calibrated using a multi-ion discharge lamp with known emission spectrum. To normalize scattering spectra with the incident lamp spectrum, a spectrum of the excitation xenon lamp was acquired using a Labsphere Spectralon calibrated scattering substrate.

3.3 RESULTS AND DISCUSSION

Three distinct states can be encountered in vivo after injection of MAPS: 1) cells with no MAPS present at the site of interest, 2) no interactions between cells and delivered MAPS due to the lack of a molecular biomarker of interest, and 3) molecular specific interactions between cells and targeted MAPS. Hyperspectral and dark field optical microscopy of cell cultures simulating these three states (Figure 3.2) shows that delivery of MAPS increases optical absorption and scattering in the wavelength range near nanoparticle plasmon resonance peak (Figure 3.2b-d) while molecular specific

interactions between MAPS and EGFR-expressing cancer cells are associated with dramatic changes in optical properties of the sample including broadening and strong red/near-infrared (NIR) shift of the peak wavelength of the optical spectrum of MAPS (Figure 3.2b,e). These changes are due to receptor-mediated aggregation and plasmon resonance coupling between closely spaced MAPS (Figure 3.2f-h)²⁶. The differences in optical properties of free MAPS and labeled cancer cells provide a straightforward mechanism to detect metastatic cancer cells using non-invasive sPA imaging at a sufficient depth for detection of micrometastasis in the lymphatics of cancer patients.

For the *in vivo* experiments, EGFR-targeted MAPS or control AuNPs conjugated with non-specific RG16 monoclonal antibody were injected peritumorally into tumor-bearing or normal mice and were allowed to drain to the cervical LNs. In clinical practice a similar injection of radionuclide tracers is routinely performed to identify the location of LNs, however, it does not allow detection of cancer cells. The RG16 antibody acts as a nonspecific control because it targets heavy chains of rabbit IgG/IgM/IgA, which are not normally present in endogenous mouse or FaDu cells. The total nanoparticle injected dose was approximately 1.6 pmol – that is significantly less than a dose of AuNPs with any reported cytotoxicity *in vivo*²⁴. The cervical LNs – the site of micrometastatic foci in this mouse model²² – were identified using US imaging. Combined US/sPA imaging was performed before and immediately following injection of the nanoparticles. The studies consisted of three animal groups: 1) mice with the orthotopic tongue primary tumor which are injected with EGFR-targeted MAPS, 2) mice with the orthotopic tongue tumor which are injected with control RG16-conjugated AuNPs, and 3) mice with no tumor inoculation which are injected with EGFR-targeted MAPS. Following the US/sPA imaging, the presence of micrometastases was confirmed using bioluminescence imaging (Figure 3.3b) and histology.

Representative overlaid US and sPA images of cervical LNs (Figure 3.3c-e) depicting the anatomy (gray) and contributions from sPA_{HbO2} (red), sPA_{Hb} (blue), and sPA_{MAPS} (yellow) after the peritumoral injection of MAPS show the ability of sPA imaging to detect micrometastases in the lymphatics with high spatial resolution. LNs are easily identifiable by a dark hypoechoic bean-shaped region in the US images. The injection of EGFR-targeted MAPS leads to a strong increase in the sPA_{MAPS} signal from the LNs with micrometastases (Figure 3.3c) which were independently confirmed by bioluminescence imaging in vivo (Figure 3.3b) and histopathological evaluation ex vivo (Figure 3.6). Tumor-bearing mice injected with EGFR-targeted MAPS exhibit a statistically significant increase in sPA_{MAPS} signal from metastatic LNs (N = 7 nodes) over LNs of control mice injected with RG16-conjugated AuNPs (N = 7 nodes, p = 0.006) and either LNs of normal mice or normal nodes in tumor-bearing mice injected with EGFR-targeted MAPS (N = 8 nodes, p = 0.037; Figure 3.4). Statistical analysis of this data results in a sensitivity of 85.7% and a specificity of 87.5% of this method in detection of lymph node micrometastasis. A three-dimensional reconstruction of the US/sPA images shows the sPA_{MAPS} signal is constrained to a small region of the LN (Figure 3.3f,g). Indeed, metastatic foci as small as 50 μm (as measured from histology) were detected using this method.

Sustained sPA imaging of cervical lymph nodes immediately following MAPS injection showed strong labeling of cancer cells over the course of two hours indicating quick delivery of the nanoparticles (Figure 3.5). A steady increase in sPA_{MAPS} signal amplitude and volume was seen in a small localized region on the border of the SLN. Little variation was observed in other regions of the image, indicating that sPA imaging is a reliable method to observe cancer cell mediated activation of MAPS. Furthermore, the short time scale of delivery and cell interactions of MAPS indicates that this method

would be well-suited clinically. These results indicate that by using sPA imaging of MAPS, diagnosis could be achieved noninvasively and in real-time.

The results of *in vivo* imaging were validated using histology of the excised LNs (Figure 3.6). H&E staining (Figure 3.6a-f) confirmed the presence of the metastases which were indicated by the bioluminescence imaging and were detected by sPA with EGFR-targeted MAPS. The metastases tended to form in the subcapsular region of the node near the afferent lymphatic vessel or within the vessel itself. This trend is in excellent correlation with the regions of elevated sPA_{MAPS} signal. Immunohistochemistry (Figure 3.6g-i) confirmed the elevated EGFR expression in the micrometastases. In addition, silver staining showed the presence of gold nanoparticles in lymph nodes from mice in all three groups. The lack of significant increases in the sPA_{MAPS} signal in control mice and in normal nodes of tumor-bearing mice, despite successful nanoparticle delivery to the LNs, indicates that EGFR-targeted MAPS are not activated in LNs in the absence of cancer cells and control RG16-conjugated AuNPs neither accumulate inside metastatic cells nor undergo other non-specific aggregation.

Molecular specific imaging of small cellular clusters *in vivo* at substantial depth remains a great challenge in modern biology and medicine²⁷. Attempts have been made to extend virtually every biomedical imaging modality, including positron emission tomography (PET)²⁸, magnetic resonance imaging²⁹, ultrasound (US) imaging³⁰, optical imaging³¹, and photoacoustic (PA) imaging^{18, 19, 32}, to localize molecular expressions *in vivo*. Nevertheless, accurate measurements of molecular expressions in a tissue remain a difficult task. Indeed, it is commonly assumed that the presence of a molecularly-targeted contrast agent correlates to the level of expression of the targeted molecule. What this assumption fails to consider is that delivery of a contrast agent to a site of interest and interaction between the agent and its target are two independent events. Therefore,

passive accumulation of a contrast agent in a tissue (e.g., via the enhanced permeability and retention effect in tumors³³) leads to decreased specificity in molecular sensing^{27, 34}.

Advanced optical imaging techniques, such as Förster Resonance Energy Transfer³⁵ or fluorescent imaging using activatable probes¹³, are able to provide a much more specific visualization of molecular expressions. However, these methods suffer from low penetration depth (less than one millimeter in the ballistic regime of photon transport) or poor resolution and sensitivity at greater depths³¹. Furthermore, fluorescent probes are prone to photobleaching. All of these factors severely limit clinical applicability of optical techniques for molecular detection of diseases, including micrometastases. Photoacoustic imaging addresses these limitations by combining the high contrast of optical imaging with the excellent resolution of US imaging at depths up to 5 cm¹⁷⁻¹⁹. In addition, plasmonic nanoparticles characterized by enhanced optical absorption and photostability^{36, 37} provide strong contrast in PA imaging^{36, 37}. Their easily modified surface^{23, 38} and large optical absorption (up to five orders of magnitude greater than dye molecules³⁹) make them ideally suited for localizing molecular expressions *in vivo*. However, previous efforts to combine plasmonic nanoparticles with *in vivo* PA imaging have not addressed the fundamental challenge in specificity that most other molecular imaging modalities suffer from: nanoparticles which have interacted with a molecule of interest cannot be differentiated from those which have simply been delivered to the region.

In contrast, this chapter presents a new approach for *in vivo* detection of cell surface receptors that is based on nano-scale interactions between cells and MAPS. The results show an excellent ability to detect small colonies of cancerous cells. Indeed, the 85.7% sensitivity and 87.5% specificity of sPA imaging of MAPS are significantly better than the results obtained using other non-invasive imaging modalities⁴⁰. For example,

PET imaging, while more sensitive than many other radiographic modalities, has 50% sensitivity and 87% specificity in detection of impalpable cervical metastases in oral cancer⁴¹; furthermore, it can only reliably detect metastatic foci greater than 80 mm³.¹¹ Demonstrated here is the capacity to detect metastatic tumors consisting of just few tens of malignant cells deep inside tissue.

3.4 CONCLUSIONS

This work builds on the functional imaging presented in Chapter 2 by adding a framework in which specific molecular expressions can be visualize with high sensitivity. The activatable nature of the MAPS means that the mere presence of the contrast agent in a LN does not generate a sPA signal; a molecular interaction must occur. The clinical translation of this technology will be facilitated by the miniaturization of the MAPS to ca. 5 nm. This will likely lead to rapid renal clearance of the MAPS while still preserving their functionality.

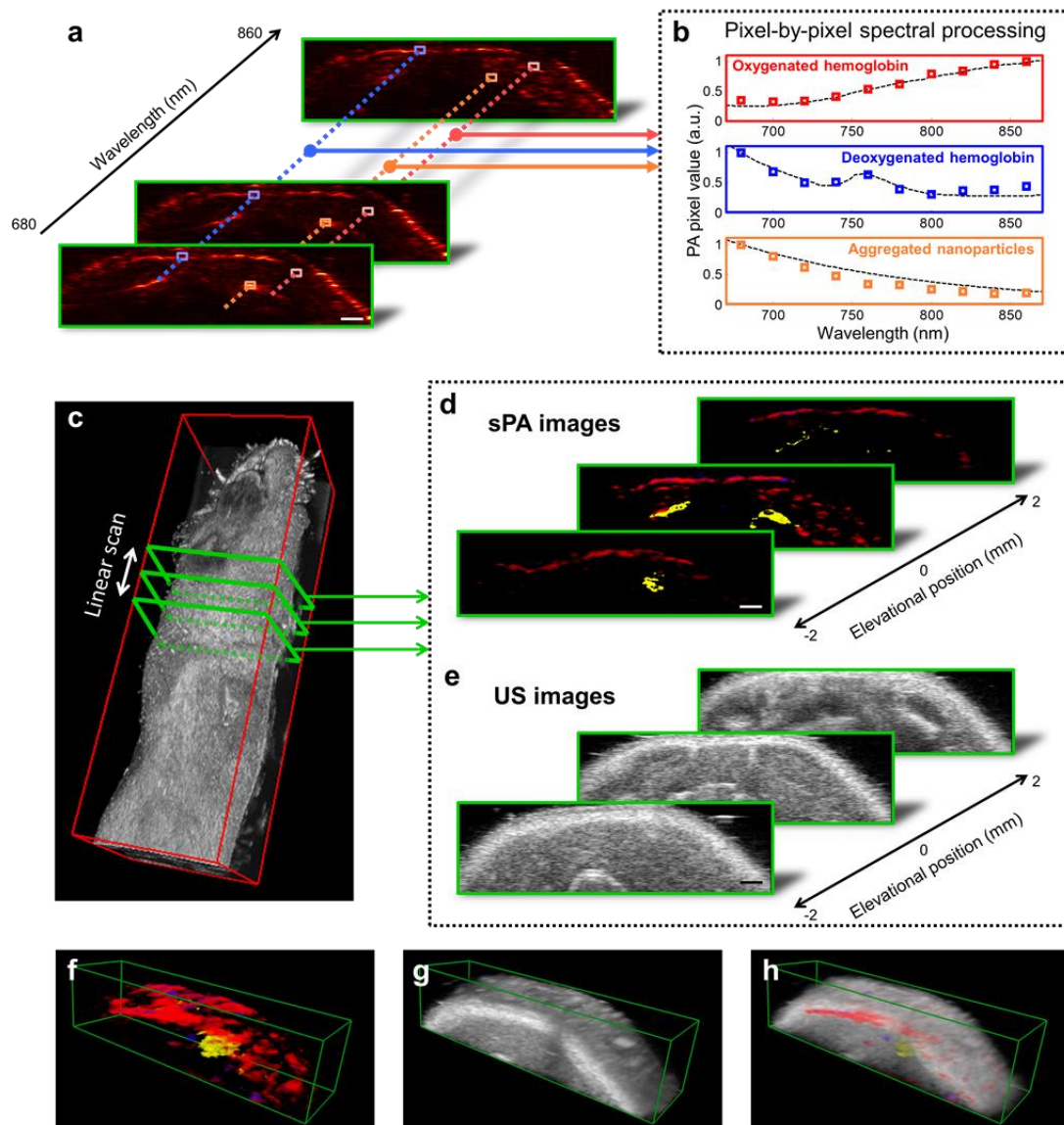


Figure 3.1 (a) In each two-dimensional plane PA images are acquired using excitation wavelengths spanning 680 nm to 860 nm in steps of 20 nm. (b) Each pixel is compared to one of three optical spectra: oxygenated hemoglobin, deoxygenated hemoglobin, and activated MAPS; the dashed lines represent the expected spectra, while the colored boxes are the measured PA signals. (c) The transducer is scanned in the elevational direction to acquire a set of coregistered (d) sPA and (e) US images. Each of the slices is combined to create three dimensional (f) sPA, (g) US, and (h) combined sPA and US images. Scale bars are 1 mm.

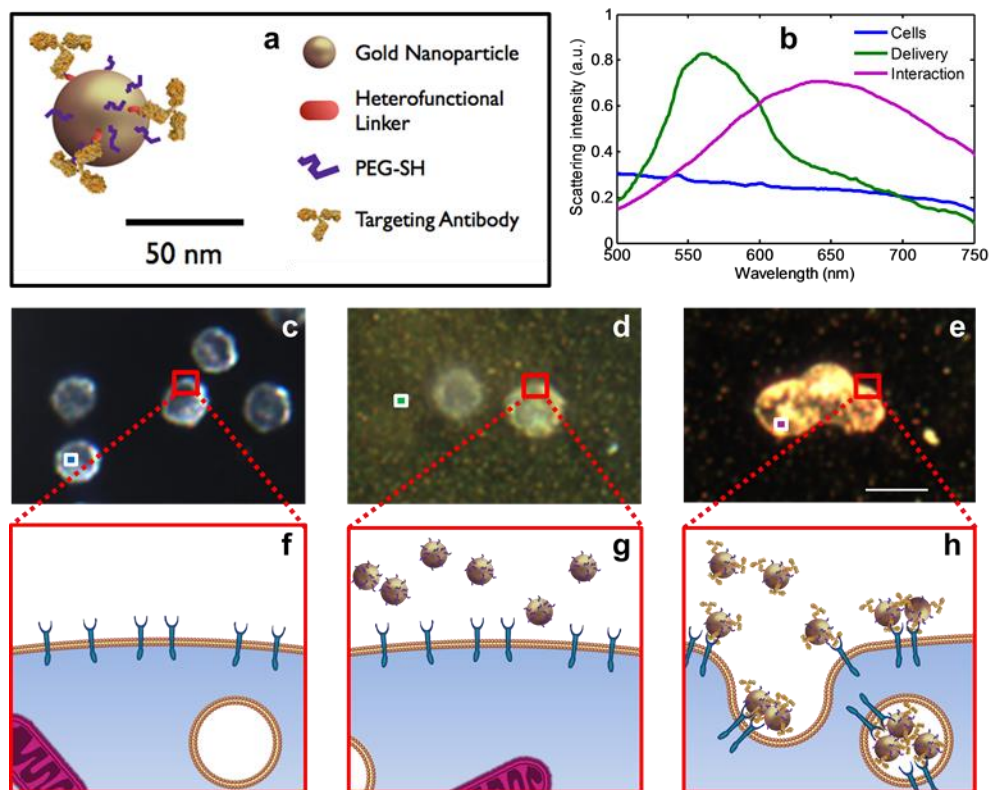


Figure 3.2 (a) A schematic of the EGFR-targeted MAPS; relative dimensions of antibody molecules and a gold nanoparticle (AuNPs) are preserved. (b) Hyperspectral darkfield microscopy was used to obtain optical spectra from unlabeled cells (blue), MAPS dispersed in extracellular space (green), and cells labeled with MAPS (violet). Dark-field optical images (c, d, and e; scale bar is 10 μm) and cartoon (f, g, and h) show: (c and f) cancer cells in the absence of gold nanoparticles; (d and g) cells in the presence of non-specific AuNPs; and (e and h) cells labeled with MAPS. Unlabeled cells have a characteristic bluish white appearance due to intrinsic light scattering properties (c) while a greenish haze is evident in the presence of non-specific AuNPs which strongly scatter green light (d). Molecular specific interactions between MAPS and EGFR-overexpressing cancer cells lead to receptor-mediated endocytosis which results in aggregation of the MAPS and strong changes in their optical properties (e). The colored boxes in (c-e) identify the regions from which the same-color spectral curves are displayed in (b).

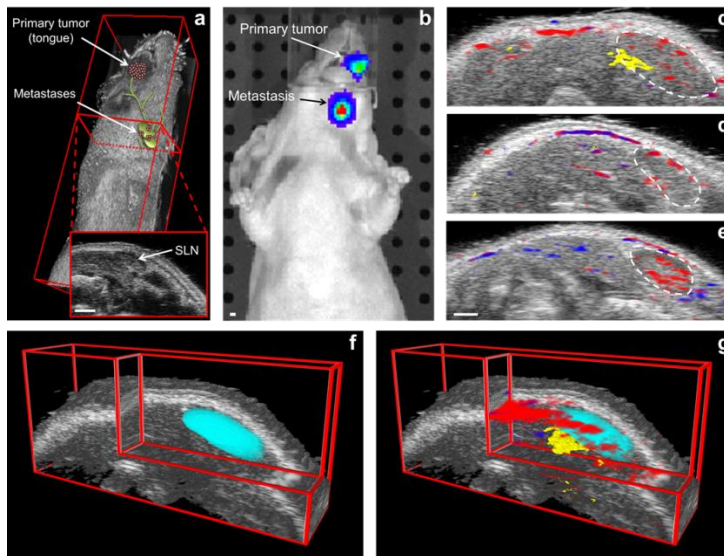


Figure 3.3 (a) Three-dimensional US image of a mouse with an overlaid cartoon of the primary tumor in the tongue and micrometastases in the cervical lymph nodes. The inset shows a two-dimensional cross section of the US image with a lymph node seen as the dark, hypoechoic oval. (b) A representative bioluminescence image confirms the presence of FaDu cells in the primary tumor and in the lymphatic system. Representative overlaid US and sPA images of: a tumor-bearing mouse with a lymph node metastasis two hours after a peritumoral injection of either (c) EGFR-targeted MAPS or (d) control RG16-conjugated AuNPs and (e) a normal mouse two hours after a submucosal injection of EGFR-targeted MAPS. Oxygenated (sPA_{HbO_2}) and deoxygenated (sPA_{Hb}) hemoglobin is depicted in red and blue, respectively, while the presence of cancer cells labeled with MAPS (sPA_{MAPS}) is depicted in yellow; anatomical location of a cervical lymph node is outlined by a dashed white line. Note, a strong sPA_{MAPS} signal in tumor-bearing mice injected with EGFR-targeted MAPS. A three-dimensional reconstruction of (f) the US images with the SLN volume segmented from the two-dimensional US images (cyan), and (g) the same image as (f) with the overlaid three-dimensional sPA image showing the volumetric distribution of sPA_{Hb} , sPA_{HbO_2} , and sPA_{MAPS} signals. All scale bars are 1 mm.

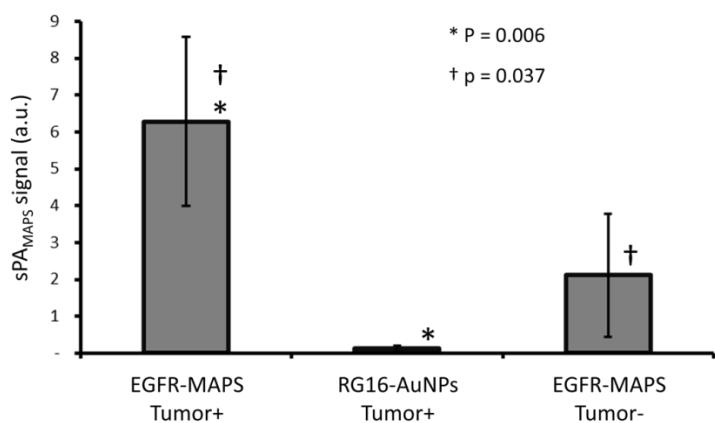


Figure 3.4 Statistical analysis of sPA imaging. The LNs were split into three categories for analysis: 1) LNs containing metastases in mice injected with EGFR-targeted MAPS (n = 7), 2) LNs in mice injected with RG16-conjugated AuNPs (n = 7), and 3) LNs without metastasis in mice with or without a primary tumor injected with EGFR-targeted MAPS (n = 8). The metastatic lymph nodes in tumor-bearing mice exhibit a statistically significant increase in the sPA_{MAPS} signal.

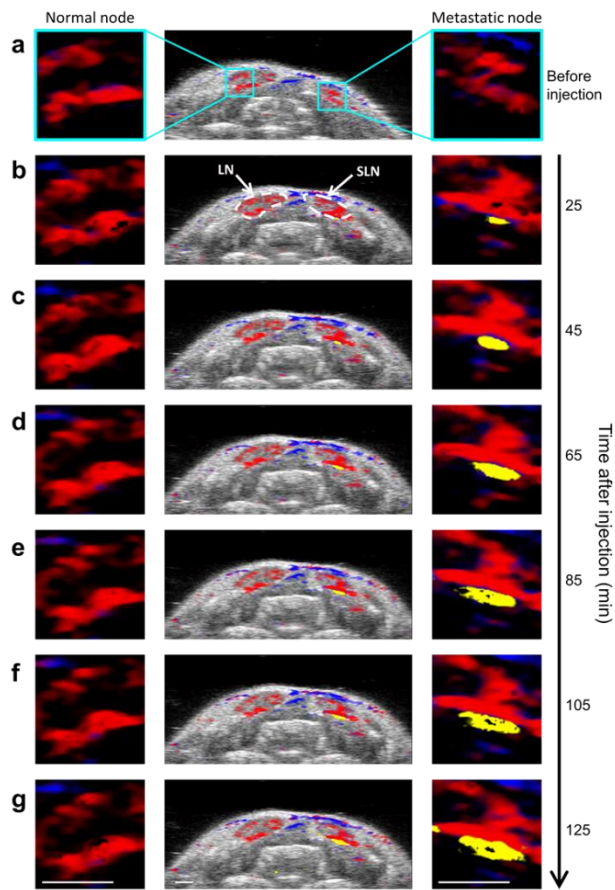


Figure 3.5 Combined US and sPA image of a two-dimensional cross section containing two lymph nodes (center), and 4x enlarged sPA images of a region on the border of the left lymph node (left) and right lymph node (right) (a) before, (b) 25, (c) 45, (d) 65, (e) 85, (f) 105, and (g) 125 minutes after the injection of MAPS. The steadily growing region of activated MAPS in the right lymph node indicates that MAPS are gradually being delivered to and are interacting with cancer cells on the border of the lymph node. Scale bars are 1 mm.

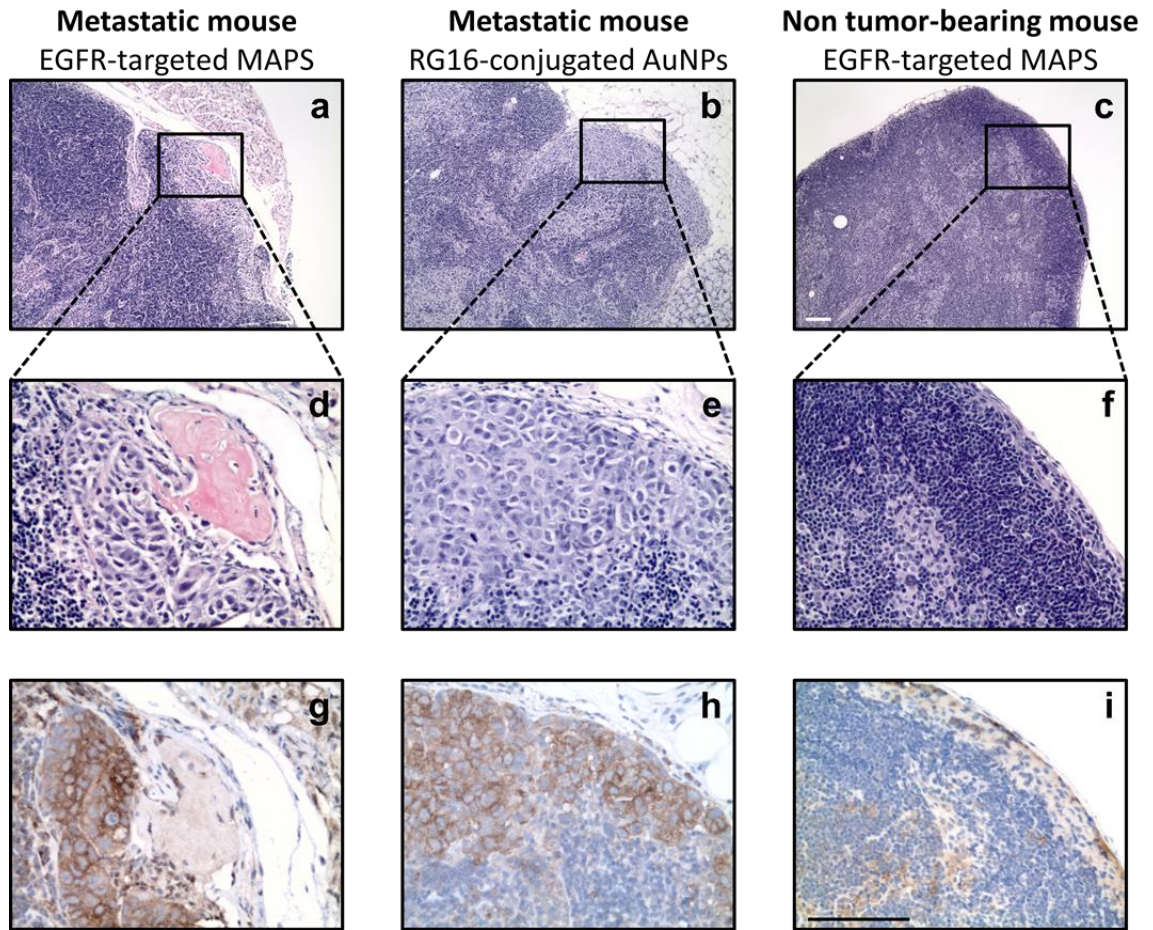


Figure 3.6 (a,b) H&E staining of lymph nodes from mice with positive bioluminescent signal in lymph nodes shows the subcapsular formation of micrometastases near an afferent lymph vessel. (c) The morphology of a lymph node from a normal mouse is shown for reference. (d,e) At high magnification, the irregular shape and large nuclei indicate presence of cancer cells in H&E sections. (f) A normal population of lymphatic cells is seen in normal mice. Immunohistochemical staining shows (g-h) elevated expression of EGFR in the micrometastases and (i) negligible EGFR expression in normal nodes. Scale bars are 50 μm .

3.5 REFERENCES

1. Gershenwald, J.E. et al. Multi-Institutional Melanoma Lymphatic Mapping Experience: The Prognostic Value of Sentinel Lymph Node Status in 612 Stage I or II Melanoma Patients. *Journal of Clinical Oncology* **17**, 976 (1999).
2. Stoeckli, S.J., Steinert, H., Pfaltz, M. & Schmid, S. Sentinel Lymph Node Evaluation in Squamous Cell Carcinoma of the Head and Neck. *Otolaryngology - Head and Neck Surgery* **125**, 221-226 (2001).
3. Veronesi, U. et al. Sentinel-node biopsy to avoid axillary dissection in breast cancer with clinically negative lymph-nodes. *Lancet* **349**, 1864-1867 (1997).
4. Ronka, R. et al. The impact of sentinel node biopsy and axillary staging strategy on hospital costs. *Annals of oncology : official journal of the European Society for Medical Oncology / ESMO* **15**, 88-94 (2004).
5. Bergkvist, L. & Frisell, J. Multicentre validation study of sentinel node biopsy for staging in breast cancer. *British Journal of Surgery* **92**, 1221-1224 (2005).
6. Goldberg, J., Riedel, E., Morrow, M. & Van Zee, K. Morbidity of Sentinel Node Biopsy: Relationship Between Number of Excised Lymph Nodes and Patient Perceptions of Lymphedema. *Annals of Surgical Oncology* **18**, 2866-2872 (2011).
7. Langer, I. et al. Morbidity of Sentinel Lymph Node Biopsy (SLN) Alone Versus SLN and Completion Axillary Lymph Node Dissection After Breast Cancer Surgery: A Prospective Swiss Multicenter Study on 659 Patients. *Annals of Surgery* **245**, 452-461 (2007).
8. Cohen, S.M., FISHINGHAWK, B.G. & COHEN, M.S. Translational imaging of lymphatics in cancer. *Advanced Drug Delivery Reviews* **63**, 956-962 (2011).
9. Wunderbaldinger, P. Problems and prospects of modern lymph node imaging. *European Journal of Radiology* **58**, 325-337 (2006).
10. Kim, S. et al. Near-infrared fluorescent type II quantum dots for sentinel lymph node mapping. *Nat Biotechnol* **22**, 93-97 (2004).
11. Wagner, J.D. et al. FDG-PET sensitivity for melanoma lymph node metastases is dependent on tumor volume. *Journal of surgical oncology* **77**, 237-242 (2001).
12. Van der Hoeven, J.J.M., Hoekstra, O.S., Comans, E.F.I. & al., e. Determinants of diagnostic performance of [F-18]Fluorodeoxyglucose positron emission tomography for axillary staging in breast cancer. *Ann Surg* **236**, 619-624 (2002).

13. Savariar, E.N. et al. Real-time In Vivo Molecular Detection of Primary Tumors and Metastases with Ratiometric Activatable Cell-Penetrating Peptides. *Cancer research* **73**, 855-864 (2013).
14. Zhang, H.F., Maslov, K., Stoica, G. & Wang, L.V. Functional photoacoustic microscopy for high-resolution and noninvasive in vivo imaging. *Nat Biotech* **24**, 848-851 (2006).
15. Eghtedari, M. et al. High sensitivity of in vivo detection of gold nanorods using a laser optoacoustic imaging system. *Nano Lett* **7**, 1914-1918 (2007).
16. Luke, G.P., Yeager, D. & Emelianov, S.Y. Biomedical applications of photoacoustic imaging with exogenous contrast agents. *Ann Biomed Eng* **40**, 422-437 (2012).
17. Diebold, G.J., Khan, M.I. & Park, S.M. Photoacoustic "signatures" of particulate matter: optical production of acoustic monopole radiation. *Science* **250**, 101-104 (1990).
18. Wang, L.V. & Hu, S. Photoacoustic tomography: in vivo imaging from organelles to organs. *Science* **335**, 1458-1462 (2012).
19. Beard, P. Biomedical photoacoustic imaging. *Interface Focus* **1**, 602-631 (2011).
20. Song, K.H., Stein, E.W., Margenthaler, J.A. & Wang, L.V. Noninvasive photoacoustic identification of sentinel lymph nodes containing methylene blue in vivo in a rat model. *Journal of Biomedical Optics* **13**, 054033-054036 (2008).
21. Song, K.H., Kim, C., Cogley, C.M., Xia, Y. & Wang, L.V. Near-Infrared Gold Nanocages as a New Class of Tracers for Photoacoustic Sentinel Lymph Node Mapping on a Rat Model. *Nano Letters* **9**, 183-188 (2008).
22. Myers, J.N., Holsinger, F.C., Jasser, S.A., Bekele, B.N. & Fidler, I.J. An Orthotopic Nude Mouse Model of Oral Tongue Squamous Cell Carcinoma. *Clinical Cancer Research* **8**, 293-298 (2002).
23. Kumar, S., Aaron, J. & Sokolov, K. Directional conjugation of antibodies to nanoparticles for synthesis of multiplexed optical contrast agents with both delivery and targeting moieties. *Nature Protocols* **3**, 314-320 (2008).
24. Khlebtsov, N. & Dykman, L. Biodistribution and toxicity of engineered gold nanoparticles: a review of in vitro and in vivo studies. *Chemical Society Reviews* **40**, 1647-1671 (2011).

25. Kim, S., Chen, Y.-S., Luke, G.P. & Emelianov, S.Y. In vivo three-dimensional spectroscopic photoacoustic imaging for monitoring nanoparticle delivery. *Biomed. Opt. Express* **2**, 2540-2550 (2011).
26. Aaron, J., Travis, K., Harrison, N. & Sokolov, K. Dynamic imaging of molecular assemblies in live cells based on nanoparticle plasmon resonance coupling. *Nano Lett* **9**, 3612-3618 (2009).
27. Weissleder, R. Molecular imaging in cancer. *Science* **312**, 1168-1171 (2006).
28. Gambhir, S.S. Molecular imaging of cancer with positron emission tomography. *Nat Rev Cancer* **2**, 683-693 (2002).
29. Lee, J.-H. et al. Artificially engineered magnetic nanoparticles for ultra-sensitive molecular imaging. *Nature medicine* **13**, 95-99 (2006).
30. Kaufmann, B.A. & Lindner, J.R. Molecular imaging with targeted contrast ultrasound. *Current opinion in biotechnology* **18**, 11-16 (2007).
31. Weissleder, R. & Ntziachristos, V. Shedding light onto live molecular targets. *Nature medicine* **9**, 123-128 (2003).
32. Mallidi, S., Luke, G.P. & Emelianov, S. Photoacoustic imaging in cancer detection, diagnosis, and treatment guidance. *Trends in Biotechnology* **29**, 213-221 (2011).
33. Maeda, H. The enhanced permeability and retention (EPR) effect in tumor vasculature : The key role of tumor-selective macromolecular drug targeting. *Adv. Enzyme Regul.* **41**, 189-207 (2001).
34. Massoud, T.F. & Gambhir, S.S. Molecular imaging in living subjects: seeing fundamental biological processes in a new light. *Genes & development* **17**, 545-580 (2003).
35. Jares-Erijman, E.A. & Jovin, T.M. FRET imaging. *Nature biotechnology* **21**, 1387-1395 (2003).
36. Luke, G., Yeager, D. & Emelianov, S. Biomedical Applications of Photoacoustic Imaging with Exogenous Contrast Agents. *Annals of Biomedical Engineering*, 1-16 (2011).
37. Emelianov, S.Y., Li, P.-C. & O'Donnell, M. Photoacoustics for molecular imaging and therapy. *Physics Today*, 34-39 (2008).

38. Niidome, T. et al. PEG-modified gold nanorods with a stealth character for in vivo applications. *Journal of Controlled Release* **114**, 343-347 (2006).
39. Jain, P.K., Lee, K.S., El-Sayed, I.H. & El-Sayed, M.A. Calculated Absorption and Scattering Properties of Gold Nanoparticles of Different Size, Shape, and Composition: Applications in Biological Imaging and Biomedicine. *The Journal of Physical Chemistry B* **110**, 7238-7248 (2006).
40. Stuckensen, T., Kovács, A.F., Adams, S. & Baum, R.P. Staging of the neck in patients with oral cavity squamous cell carcinomas: a prospective comparison of PET, ultrasound, CT and MRI. *Journal of Cranio-Maxillofacial Surgery* **28**, 319-324 (2000).
41. Kyzas, P.A., Evangelou, E., Denaxa-Kyza, D. & Ioannidis, J.P. 18F-fluorodeoxyglucose positron emission tomography to evaluate cervical node metastases in patients with head and neck squamous cell carcinoma: a meta-analysis. *Journal of the National Cancer Institute* **100**, 712-720 (2008).

Chapter 4: Optimization of Wavelength Selection for Spectroscopic Photoacoustic Imaging

4.1 INTRODUCTION

Photoacoustic (PA) imaging is a rapidly growing biomedical imaging modality.¹⁻⁵ PA imaging offers high contrast derived from differences in optical absorption with excellent resolution at clinically relevant depths. Endogenous chromophores, such as hemoglobin, melanin, and lipids, can all be detected using PA imaging.⁶⁻⁸ This shows great promise for the noninvasive clinical detection and characterization of atherosclerotic plaques^{9, 10} and certain tumors.¹¹ Highly absorbing contrast agents (e.g., dyes or plasmonic nanoparticles) are commonly used in conjunction with PA imaging.¹²⁻¹⁶ These contrast agents are often augmented with molecular targeting agents to observe a specific cellular expression or interaction, allowing for further characterization of the disease.^{15, 17}

The optical absorption spectra of the tissue components and contrast agents vary greatly with optical wavelength. Therefore, spectroscopic methods can be used to unmix the signals from different optical absorbers in a photoacoustic image and provide an estimate of their concentrations.^{8, 13, 18} This technique is known as spectroscopic PA (sPA) imaging. sPA imaging allows for accurate measurement of blood oxygenation saturation (SO₂) or nanoparticle deposition in tissue.^{19, 20}

A number of methods have been proposed to spectrally unmix absorbers in PA images. One simple spectroscopic method uses a ratio of the PA signals acquired at two optical wavelengths. This ratio is then used to estimate either SO₂ or the state of an activatable contrast agent.^{21, 22} The main drawback of using a ratio is that at most two absorbers can be distinguished, limiting the potential applications. Intraclass correlation

(ICC) has been used to simultaneously identify multiple absorbers. ICC correlates the measured PA spectrum at each pixel to the known absorption spectra of the anticipated absorbers and assigns each pixel to one (and only one) absorber.¹³ This method can identify multiple chromophores, but the assumption that each pixel only contains one absorber is not always valid – particularly in the case of blood, where the spectrum is a linear combination of deoxygenated and oxygenated hemoglobin, depending on the level of SO_2 .

An alternative approach, which treats each pixel as a linear combination of absorbers, provides a more realistic model.²⁰ Thus, each pixel can contain multiple absorbers and the relative contribution of each absorber to the overall spectrum can be estimated. A linear model is then used to calculate the absorber concentrations in each pixel while minimizing the mean squared error.

In each aforementioned method, the choice of optical wavelengths is critically important. The unique spectral features of each absorber must be captured by a discrete set of wavelengths. Ideally, a large number of wavelengths spanning a broad spectrum should be used. In practice, the number of wavelengths that can be used is limited by a number of factors, including the linewidth of the laser, the spectral range of the laser, the spectral-dependent attenuation of light in tissue, and the pulse repetition rate of the laser. In PA imaging, the temporal resolution is primarily limited by the pulse repetition rate of the laser, typically 10-20 Hz for a high energy tunable laser system. Each imaging wavelength further decreases the temporal resolution, thereby increasing the overall imaging time and the likelihood of introducing motion artifacts, which can be detrimental to spectral unmixing. Thus, wavelength selection can be used to improve the temporal resolution while maintaining acceptable levels of uncertainty in the estimated chromophore concentrations. Heretofore, the optical wavelengths used in sPA imaging

have typically been chosen heuristically. This chapter introduces a method to select optical wavelengths – termed σ_{\min} -selection – such that the concentration estimation remains robust in the presence of noise.

4.2 MATERIALS AND METHODS

4.2.1 Wavelength Selection Algorithm

The goal of the wavelength selection algorithm was to select a set of optical wavelengths in such a way as to increase the accuracy of existing spectral unmixing algorithms. This set of imaging wavelengths was chosen from a larger set of wavelengths for which accurate values of $\mu_a(\lambda)$ for each of the absorbers in the imaging volume were found from literature or were measured (e.g., via spectrophotometry). Extraneous wavelengths were recursively discarded such that the salient features of each absorber’s spectrum are maintained.

This works builds upon the sPA imaging framework explained in Section 1.1.5. Recall that the estimated absorption coefficient (as obtained from the PA image), $\boldsymbol{\mu}_{\text{est}}$, is the product of the molar absorption matrix, $\boldsymbol{\varepsilon}$, and the absorber concentrations, \mathbf{C} :

$$\boldsymbol{\mu}_{\text{est}} = \boldsymbol{\varepsilon} \mathbf{C}. \quad (4.1)$$

Note that the bold notation indicates a vector/matrix. This set of (typically over-constrained) linear equations can be solved with minimal mean-squared error by using the pseudoinverse of the molar absorption matrix, $\boldsymbol{\varepsilon}^+$:

$$\mathbf{C} \approx \boldsymbol{\varepsilon}^+ \boldsymbol{\mu}_{\text{est}}, \quad (4.2)$$

where $\boldsymbol{\varepsilon}^+$ is defined as²³

$$\boldsymbol{\varepsilon}^+ = (\boldsymbol{\varepsilon}^T \boldsymbol{\varepsilon})^{-1} \boldsymbol{\varepsilon}^T. \quad (4.3)$$

First, the molar absorption matrix, $\boldsymbol{\varepsilon}$, was populated with the absorption spectra with N columns corresponding to individual absorbers and M rows corresponding to the optical wavelengths. Only absorbers that are present in the imaging volume and generate detectable PA signal in the spectral range should be included in $\boldsymbol{\varepsilon}$. The number of rows is limited by a number of factors, including the spectral range of the laser and spectral resolution of the absorption spectra data. It was assumed that the $\text{rank}(\boldsymbol{\varepsilon}) = N$. That is, the concentrations of all N absorbers can be perfectly reconstructed from the M wavelengths in the absence of noise.

The smallest singular value of $\boldsymbol{\varepsilon}$, σ_{\min} , was used as an indication of its stability. As $\sigma_{\min} \rightarrow 0$, $\boldsymbol{\varepsilon}$ becomes unstable and may lose rank in the presence of noise. In other words, the spectrum of one absorber can be approximated by a linear combination of the other absorbers. Thus, multiple combinations of absorber concentrations can represent a single PA spectrum.

Each row was iteratively removed from $\boldsymbol{\varepsilon}$ and σ_{\min} was calculated for the truncated matrix. The row whose removal resulted in the largest σ_{\min} was taken to correspond to the least-critical wavelength and was excluded. This process was recursively repeated until the desired number of wavelengths was reached. In practice, the number of wavelengths will depend on the temporal resolution required, the noise level of the imaging system, and the desired level of accuracy in concentration estimations.

4.2.2 Simulations

In order to show the robustness of the algorithm, it must be evaluated on a large number of unique spectra. To achieve this, artificial absorption spectra were constructed spanning from 680 nm to 970 nm, a common PA imaging range that is achieved with the second harmonic of a Nd:YAG laser coupled to an optical parametric oscillator. The spectra were constructed by creating five points consisting of a random wavelength and random absorption coefficient uniformly distributed between 680-970 nm and 0-1, respectively. Then, spline interpolation was used to create a smooth absorption curve across the entire spectral range. Representative absorption spectra are shown as the solid lines in Figure 4.1a.

Four random spectra were combined into a single optical absorption matrix. A single spectrum was created from a linear combination of the four individual spectra. Ten percent additive white Gaussian noise was added to the spectrum. After pruning wavelengths using the algorithm described in the previous section, a minimum mean squared error estimate of the concentrations was calculated using the pseudoinverse of the absorption matrix. The root mean squared (RMS) error, e_{RMS} , of the estimate of each absorber's concentration, C_{est} , was used as a metric for the performance of the spectral unmixing:

$$e_{\text{RMS}} = \sqrt{\sum_i (C[i] - C_{\text{est}}[i])^2}. \quad (4.4)$$

Thus, an RMS error of 0.1 corresponds to uncertainty in the estimate equivalent to the added noise. This process was repeated 10^5 times for different concentrations of absorbers to acquire an average RMS error, after which the error was correlated to σ_{min} . Next, the process was repeated using either randomly selected wavelengths or evenly

spaced wavelengths and the error was compared for the three methods as a function of number of wavelengths.

Finally, the effect wavelength-dependent attenuation in tissue was evaluated. A decaying exponential (as a function of optical wavelength) was used to simulate the attenuation of light in tissue. The attenuation spectrum was scaled to create relative changes in fluence spanning from 0 to 100 percent (Figure 4.1b). The relative attenuation can be thought of as a depth-dependent effect. That is, as the imaging depth increases, the shorter wavelengths will be preferentially attenuated, and the laser fluence that reaches a deep-seated absorber will likewise be decreased. The absorption spectra were scaled by the resulting fluence spectrum to create a second set of spectra that represent absorbers deep in tissue. The dashed lines in Figure 4.1a show the resulting absorption spectra after a 50% relative attenuation has been applied by multiplying each absorption spectrum by the relative fluence spectrum. The σ_{\min} -selection algorithm was used to select wavelengths for both sets of spectra and the average spectral distance between each wavelength selected for the tissue-attenuated spectra and nearest selected wavelength of original spectra was calculated. This provided an estimate of how tissue attenuation affects the choice of wavelengths. Using the methods described previously, e_{RMS} of the attenuated spectra was calculated using the pseudoinverse of the original absorption matrix decimated to between 4 and 20 wavelengths using the developed method. Thus, an estimate of the error induced by ignoring wavelength-dependent attenuation in tissue was determined.

4.2.3 Phantom Study

An imaging experiment of a gelatin phantom was used to confirm the results observed in the simulations. A phantom containing 8% gelatin (Sigma-Aldrich) and 0.4%

of 30 μm silica particles (U.S. Silica) was used in this imaging study. Six glass pipettes were embedded in the top surface of the gelatin phantom (Figure 4.2a-b). The pipettes were filled with 800 μM indocyanine green (ICG) dye (Sigma-Aldrich), silica-coated gold nanorods (NRs) at a concentration of approximately 5×10^{12} particles/mL, or mixtures of the two solutions containing 20, 40, 60, or 80% NRs. These solutions correspond to 80, 60, 40, and 20% ICG, respectively.

Photoacoustic images (Figure 4.2c) of the samples were collected using a Vevo LAZR photoacoustic imaging system (VisualSonics, Inc.) with a LZ-550 linear array transducer (256 elements, 40-MHz center frequency). Photoacoustic images were acquired across the 680-970 nm spectral range in steps of 2 nm (for a total of 146 images of each sample). The PA signal is constrained to the edges of the pipette. This results from the homogenous distribution of absorbers and the relatively high center frequency of the transducer.²⁴ A region of interest at the top of the sample (white box in Figure 4.2d) was used for further analysis. The PA spectra of the 100% ICG and 100% NR solutions were used as the reference absorption spectra for wavelength selection and served as controls for spectral unmixing (Figure 4.2e). The ICG spectrum indicates that it has assumed its aggregated state.²⁵ The PA images of the region of interest of each sample (Figure 4.2f) were used to estimate the relative concentrations of ICG and NRs (Figure 4.2g). Following imaging, a 3-mm optical and ultrasound attenuation layer containing 8% gelatin, 0.4% silica, and 40 μM ICG was placed above the samples and imaging was repeated. The ICG served as an optical absorber and the silica acted as an acoustic and optical scatterer.

4.2.4 In Vivo Study

In this study, mouse lymph node mapping and characterization was performed. The study was following protocols approved by the Institutional Animal Care and Use Committee at The University of Texas at Austin. The contrast agent (MMPSense 750 FAST, Perkin Elmer) was injected into the tongue of a non-tumor-bearing Nu/Nu mouse (Charles River Laboratories) under anesthesia (Isoflurane, 1.5% in O₂) and was allowed to drain through the lymphatic system to the cervical lymph nodes located on the neck of the mouse (Figure 4.3a). Given the focus of lymph node imaging in this dissertation, this mouse model provided a good platform to study the influence of sPA wavelength selection on a clinically relevant in vivo biomedical application.²⁶ Approximately 30 minutes following the injection of the dye, combined ultrasound and PA imaging was performed using a Vevo LAZR imaging system (VisualSonics, Inc.) in a plane containing the lymph node (Figure 4.3a, red box). An LZ-550 linear array transducer (256 elements, 40 MHz center frequency; VisualSonics, Inc.) was used to collect all images in this study. The PA images were corrected for incident laser fluence and spectral processing was performed offline.

Two methods were used to select the reduced set of imaging wavelengths. First, evenly spaced wavelengths that spanned the entire imaging spectrum were selected. Second, σ_{\min} selection was used.²⁷ The sPA image has been spectrally unmixed from a set of 3 to 30 optical wavelengths spanning 680 nm to 970 nm. A linear least squared error approach was used to identify three dominant optical absorbers: deoxygenated hemoglobin (blue), oxygenated hemoglobin (red), and MMPSense dye (green).²⁰ The root mean squared (RMS) error of each pixel as a function of the number of wavelengths can be used to quantify the effect of wavelength selection on absorber concentration estimation. The concentrations estimated using all 30 wavelengths were taken to be the

“true” concentrations. Figure 4.3b shows the overlaid US and sPA images formed from all 30 wavelengths.

4.3 RESULTS AND DISCUSSION

4.3.1 Simulations

The median error in reconstructed concentrations proved to be inversely proportional to σ_{\min} across a broad range of wavelengths and optical spectra (Figure 4.4a; $R^2 = 0.96$). For large σ_{\min} , the spectra can be unmixed with high accuracy. However, as σ_{\min} approaches 0, ϵ becomes unstable and the RMS error in the reconstructed concentrations becomes much greater than the magnitude of the added noise. Thus, σ_{\min} provides a good criterion for selecting a subset of wavelengths for sPA imaging. Furthermore, because the inverse relationship is linear, σ_{\min} can be used to predict the level of precision with which absorber concentrations can be estimated. Therefore, the imaging wavelengths and contrast agent(s) can be simultaneously optimized for a given application.

The σ_{\min} -selection algorithm was compared to two other methods of wavelength selection: 1) choosing wavelengths randomly and 2) choosing wavelengths that are evenly spaced throughout the optical range (Figure 4.4b). The σ_{\min} -selection algorithm consistently yielded better results than the other two wavelength selection methods. In fact, only half of the wavelengths are needed to reach the input noise level than in the case where evenly spaced wavelengths are used. This improved performance is due to the algorithm’s tendency to preserve the salient spectral characteristics of the absorbers while extraneous wavelengths are discarded.

It should be noted that the optimization method presented in this chapter is closely related to the well-known condition number, which has also been proposed as a wavelength selection method.²⁸ The condition number, κ , is defined as:

$$\kappa = \frac{\sigma_{\max}}{\sigma_{\min}}, \quad (4.5)$$

where σ_{\max} is the largest singular value of $\boldsymbol{\varepsilon}$. In simulations, the σ_{\min} -selection algorithm performed slightly better on average than κ -selection. Furthermore, the correlation between the inverse of σ_{\min} and the RMS error ($R^2 = 0.96$) was much better than the correlation between κ and the RMS error ($R^2 = 0.63$). This can be attributed to the fact that the κ -selection method minimizes the *normalized* uncertainty in the least squares estimate of concentration, whereas the σ_{\min} -selection method minimizes the *overall* uncertainty. Therefore, the former method can lead to greater errors in regions with lower PA signal.

Equation 4.1 relies on four important assumptions: 1) the magnitude of the initial photoacoustic pressure is accurately reconstructed in each pixel, 2) the Grüneisen parameter is constant throughout the image, 3) the photoacoustic signal generation is linear, and 4) the fluence has been accurately estimated in each pixel. Neither the accuracy of the pressure reconstruction nor the Grüneisen parameter depends on the excitation wavelength. Therefore, errors resulting from the first two assumptions will only affect the magnitude of μ_{est} ; the relative absorber concentration estimates will remain unchanged. Nonlinear photoacoustic signal generation (e.g., arising from high laser fluence or aggregated nanoparticles) could lead to a distorted μ_{est} , but these nonlinear effects are not significant in most imaging applications.²⁹⁻³¹

Because the fluence is wavelength-dependent, errors from the fourth assumption will result in spectral changes of μ_{est} . Estimating the laser fluence that reaches the absorber is a complex problem and depends on the distribution of all absorbers and scatterers in the light path. Because of this dependence, the fluence and chromophore concentrations are not separable in general. This leads to an inverse problem where the chromophore concentration, absorption coefficient, scattering coefficient, and laser fluence must be solved for simultaneously.³²

While the four assumptions may introduce small errors into the estimation of absorber concentrations, they have little effect on the choice of sPA imaging wavelengths. Figure 4.5a shows the average minimum spectral distance between wavelengths selected before and after wavelength-dependent optical attenuation. The graph shows that the algorithm is robust to a broad range of relative attenuation. Thus, the wavelengths chosen based on the unattenuated absorption spectra will typically work well even when the absorbers are situated deep in tissue. If the wavelength-dependent attenuation light in tissue is not accounted for (or is incorrectly estimated), the resulting distortion of the photoacoustic spectrum will lead to errors in the absorber concentration estimation. Figure 4.5b shows a scatter plot of the errors resulting from spectral-dependent attenuation of the fluence in the absence of noise. In general, small errors in the fluence estimation result in smaller errors in the estimated concentrations. Indeed, errors greater than 20% in the estimated concentration are not common until the relative attenuation reaches 40%. Although the attenuation spectrum of light was modeled as a decaying exponentially as the optical wavelength increases, similar results were achieved for arbitrary attenuation spectra. This indicates that, while the distribution of light in tissue should be modeled for sPA imaging, small errors in the model will still result in accurate spectral unmixing results.

One particularly useful application of sPA imaging is the measurement of blood oxygen saturation. This is often performed in the absence of an exogenous contrast agent. In this case, only two spectra need to be considered: deoxygenated and oxygenated hemoglobin. In the wavelength range of 680 nm to 970 nm, evenly spaced wavelengths performed as well as the developed algorithm when only these two spectra are considered in the simulation. This can be attributed to the fact that the two spectra are significantly different throughout the spectral range. Indeed, as long as wavelengths greater than and less than 800 nm (the wavelength of equal absorption) are chosen, the oxygen saturation could be estimated with high accuracy. The σ_{\min} -selection algorithm chose wavelengths on the edges of the spectral range (i.e., 680 nm and 970 nm) with additional wavelengths contributing to improved performance mainly through the suppression of uncorrelated noise.

4.3.2 Phantom Validation

The σ_{\min} -selection algorithm was applied to the imaging of a tissue-mimicking phantom. Figure 4.6a shows the estimated relative NR concentration for the sample containing 40% NRs (solid line) when wavelengths are selected using the developed algorithm. It can be seen that sPA imaging provides a good estimate of the NR concentration even when as few as two wavelengths are used. When the optical and ultrasonic attenuating layer was added, the resulting spectrum (Figure 4.6a, dashed line) shows a slight over-estimation of the NRs. This is due to the fact the 3-mm layer preferentially attenuated the shorter wavelengths. Thus, the ICG peak appeared to be smaller in the acquired PA signals. This effect could be corrected by modeling the transmission of light through the attenuation layer. Figure 4.6b shows the relative NR concentration estimated from the same sample using evenly spaced wavelengths across

the 680 – 970 nm range. The concentration estimation is much less stable as wavelengths are removed, and large errors are observed when fewer than five wavelengths are used. When the attenuation layer was added (dashed line), a similar overestimation of the NR concentration is seen as in Figure 4.6a. In addition, the concentration estimation errors are greatly accentuated. Figure 4.6c shows a comparison of the estimated relative NR concentration for each of the samples (in the absence of the attenuation layer) when using evenly spaced wavelengths (black lines) and when using wavelengths selected using the developed algorithm (blue lines). The top and bottom lines represent controls because the PA spectra acquired from these samples were used for spectral unmixing. These results indicate that by carefully selecting imaging wavelengths, significant improvements in sPA imaging can be achieved.

4.3.3 *In vivo* Imaging

Figure 4.7 shows σ_{\min} for each of the two wavelength selection methods where the numbers of wavelength span from three wavelengths (the smallest number that can still be used to estimate the concentrations of all three absorbers) to the entire set of 30 wavelengths. It is clear that σ_{\min} is significantly higher and much more stable σ_{\min} -selected wavelengths than evenly spaced wavelengths as wavelengths are removed. This indicates that images obtained with wavelengths chosen with the σ_{\min} -selection algorithm will have better accuracy in the estimation of absorber concentrations.

The average of the RMS error across all pixels is shown in Figure 4.8, indicating that the sPA images formed from wavelengths selected with σ_{\min} selection (solid line) provide more accurate absorber concentrations than when evenly spaced wavelengths are used (dashed line). Another useful benefit of the σ_{\min} -selection is that the error does not dramatically increase as each individual wavelength is removed. Thus, the removal of a

single wavelength will lead to a predictably small change in the sPA image. It is also important to note that the local minima in Figure 4.7 occur at the same locations as the local maxima in Figure 4.8. This reinforces the observation that σ_{\min} is a good predictor of sPA imaging accuracy.

The decreased accuracy in estimating absorber concentrations as wavelengths are removed also manifests itself as qualitative degradation in sPA image quality. Indeed, by observing the sPA images formed with only a few wavelengths, it becomes more difficult to accurately capture the spectral features of the absorbers. The role that wavelength selection has on the final sPA image was analyzed by comparing the images created from three wavelengths selected by either even spacing or σ_{\min} -selection. Figure 4.9 shows a qualitative comparison of the sPA images produced after applying each of the two wavelength selection methods. When three wavelengths are used – a particularly poor choice for the case of even spacing – σ_{\min} -selection identifies wavelengths near sharp spectral features (Figure 4.9a, circles) while the evenly spaced wavelengths happen to miss these same features (Figure 4.9a, triangles). In this example, the sPA images show that the evenly spaced wavelengths tend to over-predict the presence of deoxyhemoglobin (Figure 4.9b). When the σ_{\min} -selection is used, however, the main features of the sPA image are preserved (Figure 4.9c). Thus, when only a few wavelengths are used, the choice of wavelengths becomes critical. If chosen correctly, the resulting sPA image can be reconstructed very accurately.

In the case where six imaging wavelengths are used (Figure 4.10), the evenly spaced wavelengths come much closer to capturing the spectral features (Figure 4.10a, triangles). The wavelengths chosen by σ_{\min} selection tend to accumulate near the local maxima of deoxyhemoglobin at 760 nm (Figure 4.10a, circles). Despite the fact that both methods appear to represent the spectral features, there are still significant differences in

the sPA images generated from the two wavelength selection methods (Figure 4.10b and Figure 4.10c). In fact, the RMS error in the sPA image generated from six evenly spaced wavelengths is more than twice the error in the sPA image generated from three wavelengths chosen by σ_{\min} -selection (Figure 4.8). This can be seen qualitatively in Figure 4.10b and Figure 4.9c.

The benefits of spectral unmixing and the developed algorithm depend on several factors. The contrast agent(s) must be selected to have desirable spectral characteristics. Contrast agents with distinct spectral features (e.g., a sharp peak or multiple peaks) are ideal. In general, dyes tend to have a narrower absorption peak than plasmonic nanoparticles (owing mainly to the polydispersity which results from commonly-used wet chemistry synthesis methods). Nanoparticles, however, can exhibit a much higher optical absorption than dyes.³³ Light penetration in tissue is also an important factor when choosing contrast agents. Deeper penetration in tissue at longer wavelengths (near 1064 nm), results in an increased signal-to-noise ratio.³⁴ Of course, when in vivo imaging is performed, there are many more important characteristics in determining an appropriate contrast agent. These include toxicity, clearance, circulation time, delivery and molecular specificity. Therefore, choosing one of the myriad PA contrast agents should be deliberate and will depend on the application.

Spectroscopic photoacoustic imaging can be augmented with other methods to help localize contrast agents and estimate their concentrations. One method that can be used is collecting a baseline image before administering the contrast agent. This image can be subtracted from a second image collected after the contrast agent has been injected.³⁵ If it is assumed that the concentration of endogenous absorbers does not change, then the resulting image contains only the signal from the contrast agent. After effectively removing the endogenous absorbers from the image, the sPA unmixing

algorithms can focus on resolving the exogenous contrast agents. Thus, fewer wavelengths can be used and greater accuracy in concentration estimation can be achieved. The main drawback of this method is that it requires two imaging sessions and, furthermore, exact co-registration between the two images, a feat that is often difficult to achieve in vivo.

4.4 CONCLUSIONS

In summary, the choice of optical wavelengths plays a critical role in sPA imaging. By selecting wavelengths based on the spectral characteristics of the absorbers present in the tissue, the number of imaging wavelengths can be significantly reduced without degrading the sPA image. Indeed, this study shows that a contrast agent can be effectively localized in the presence of blood when as few as three wavelengths are used. The end result is that high quality sPA images can be acquired in a fraction of the time. This will aid in the effort for sPA imaging to become a real-time, clinically translatable imaging modality. Instead of a large, expensive tunable pulsed laser, a specific set of pulsed lasers at fixed wavelengths could be used for a given clinical application. Furthermore, by analyzing the spectral features of the absorbers, the tradeoffs between imaging wavelengths, imaging time, and optical absorbers can be considered. In fact, this could be used to optimize contrast agents for a given application. This will help pave the way for effective multiplex sPA imaging with multiple contrast agents.

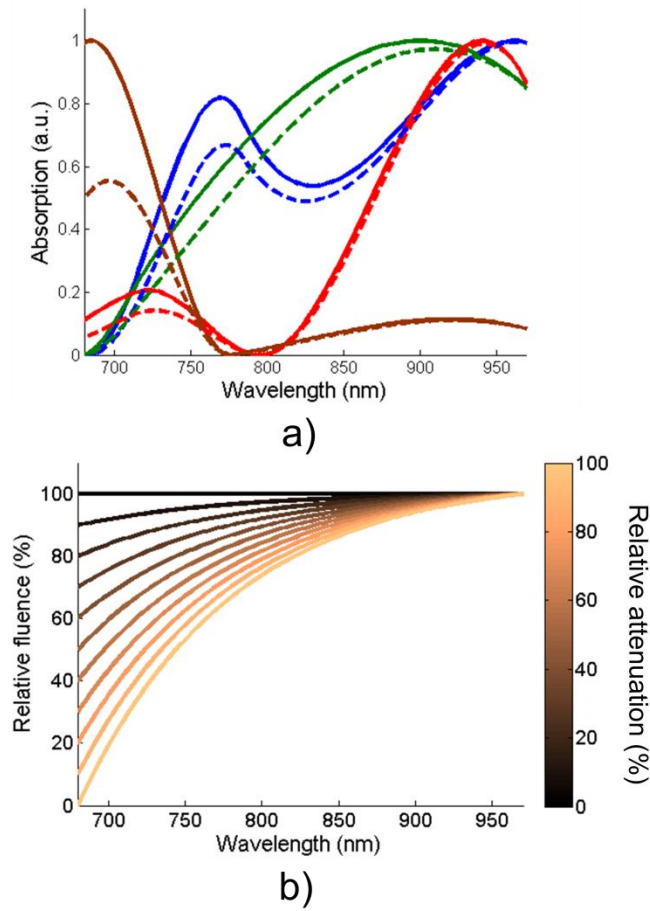


Figure 4.1 a) Representative constructed optical absorption spectra used for algorithm analysis before (solid lines) and after (dashed lines) 50% wavelength-dependent attenuation, and b) a typical attenuation curve with relative changes in laser fluence ranging from 0% to 100%.

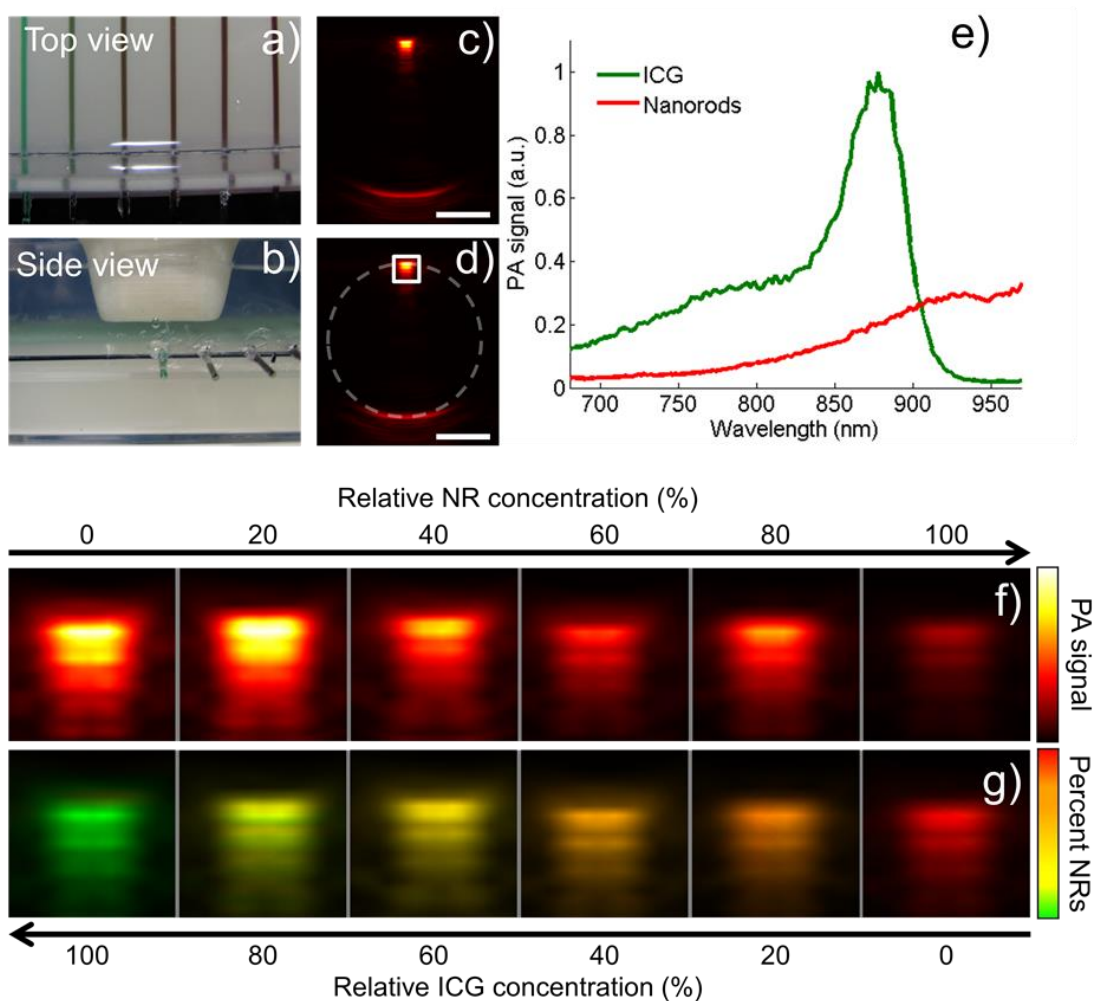


Figure 4.2 a,b) Photographs showing the imaging phantom consisting of pipettes containing ICG dye and silica-coated gold nanorods embedded in a gelatin phantom, c) a representative PA image acquired at 880 nm, d) the same image as in c) with the location of the pipette (dashed circle) and the region of interest used for further analysis (white box) indicated, e) the PA spectra of ICG and silica-coated gold nanorods which were used for spectral unmixing in this experiment, f) PA images of the region of interest of each pipette acquired with an excitation wavelength of 880 nm, and g) the spectrally unmixed sPA images of the same region of interest using PA images from all 146 optical wavelengths. Scale bars are 1 mm.

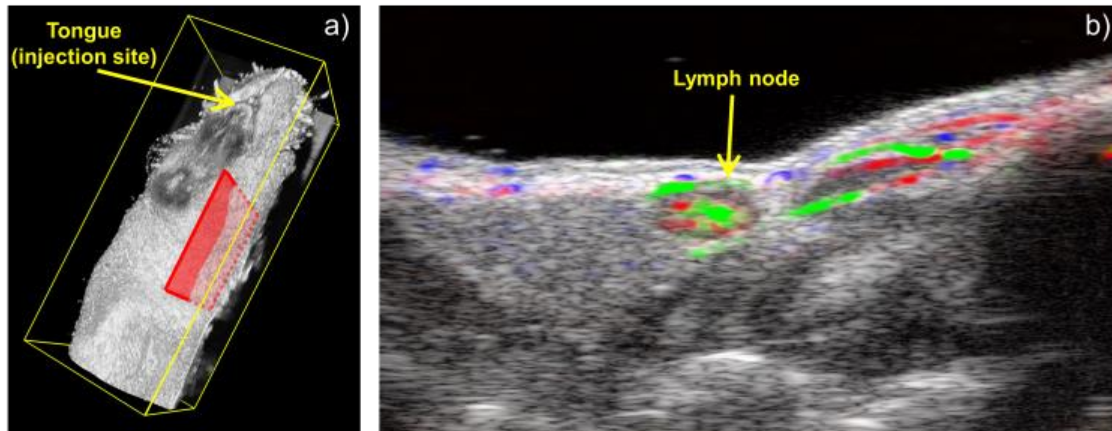


Figure 4.3 a) A three-dimensional ultrasound image of a mouse depicting the dye injection site and imaging plane (red box) and b) overlaid ultrasound and sPA image showing oxyhemoglobin and deoxyhemoglobin (red and blue, respectively) and MMPSense dye (green).

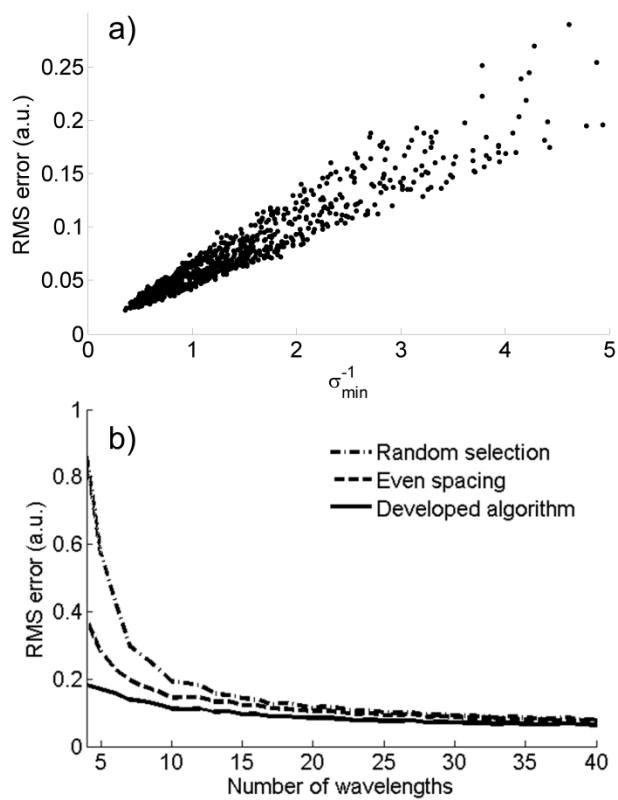


Figure 4.4 a) A scatter plot showing an inverse correlation between σ_{\min} and the RMS error in the concentration estimation, and b) a comparison between three wavelength selection strategies shows the developed algorithm performs significantly better.

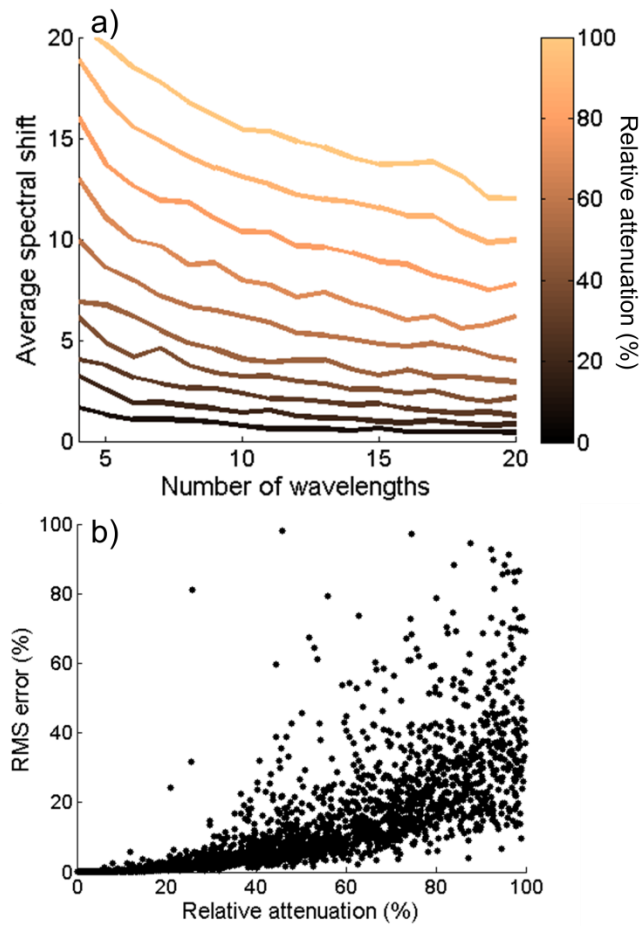


Figure 4.5 a) The average shift in the selected wavelengths after the absorption spectra have been distorted by wavelength-dependent attenuation, and b) a scatter plot of the error in the concentration estimation resulting from these changes in attenuation in the absence of noise.

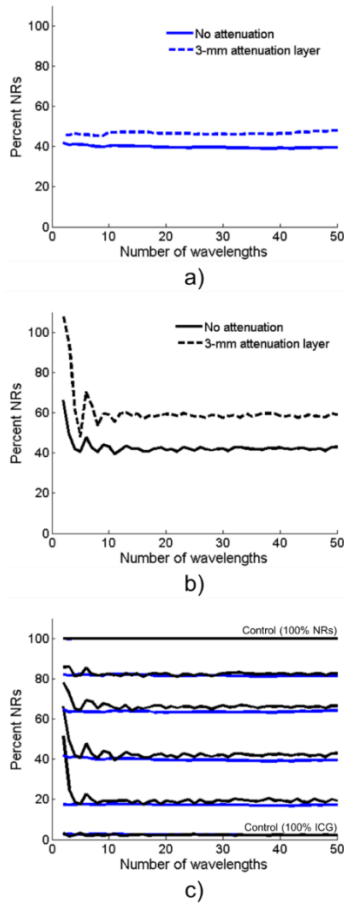


Figure 4.6 a) The relative concentrations of ICG and silica-coated gold nanorods can be accurately estimated from PA images acquired at wavelengths selected by the developed algorithm even when as few as 2 wavelengths are used (solid line). Adding a 3-mm layer of attenuating gelatin leads to a slight over-estimation of the nanorods concentration (dashed line). b) When evenly-spaced wavelengths are used, the concentration estimate becomes unstable when a small number of wavelengths are used (solid line), and this effect becomes more pronounced when the attenuating layer is added (dashed line). c) The developed algorithm (blue lines) produces much more reliable estimates of concentration than even spacing (black lines) in all inclusions. The 0% and 100% lines act as controls since the absorption spectra were derived from these signals.

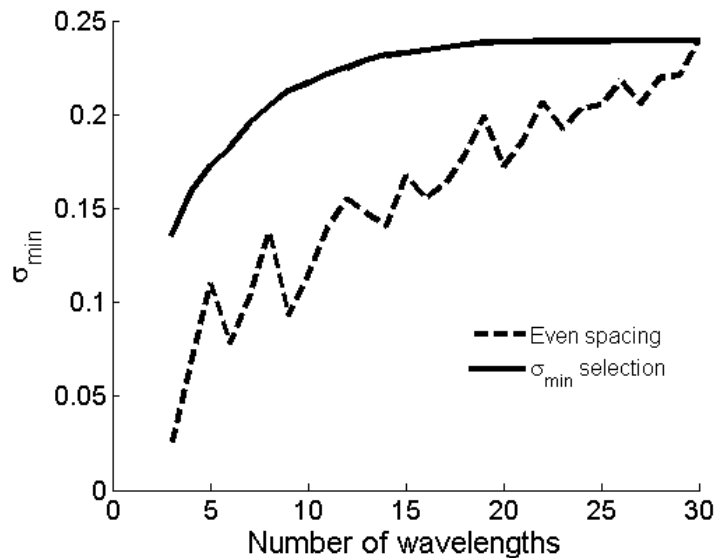


Figure 4.7 Plot demonstrating that σ_{\min} decreases as wavelengths are removed. This decrease is much less drastic and much more predictable when σ_{\min} selection is used (solid line) than when evenly spaced wavelengths are used (dashed line).

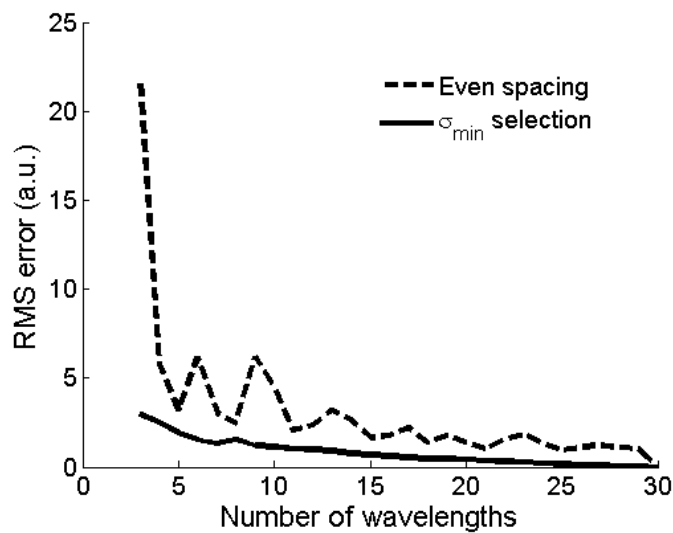


Figure 4.8 The RMS error of the absorber concentrations estimated from between 3 and 30 wavelengths. The wavelengths were selected using either even spacing (dashed line) or σ_{\min} selection (solid line).

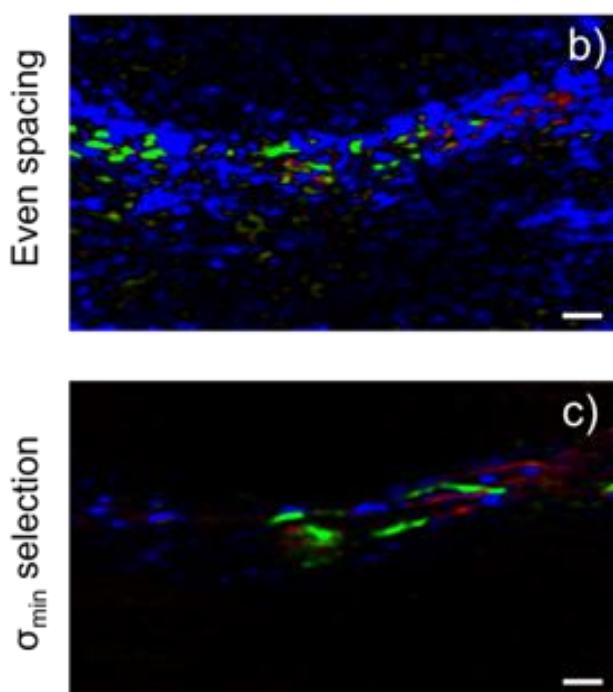
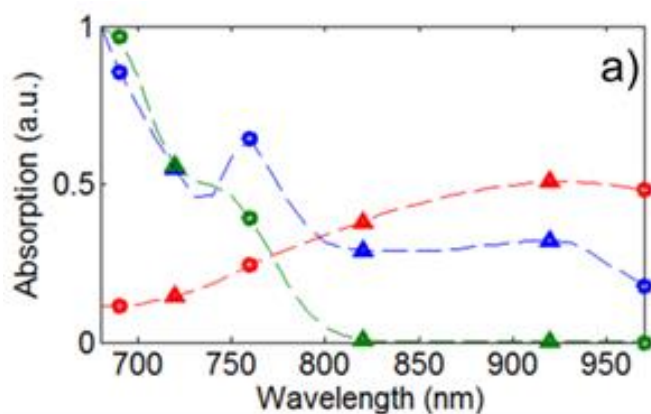


Figure 4.9 a) The spectra of the three absorbers with the three selected wavelengths using even spacing (triangles) and σ_{\min} selection (circles), and the sPA images generated from the evenly spaced wavelengths and from the σ_{\min} -selected wavelengths. Scale bars = 1 mm.

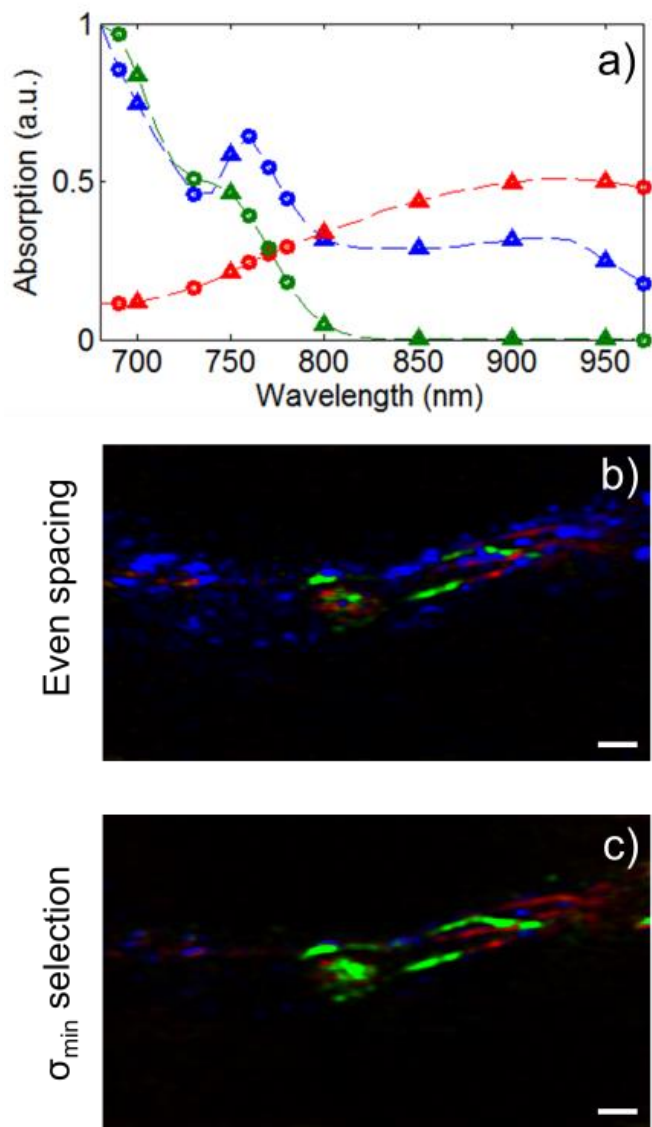


Figure 4.10 a) The spectra of the three absorbers with the six selected wavelengths using even spacing (triangles) and σ_{\min} selection (circles), and the sPA images generated from the evenly spaced wavelengths and from the σ_{\min} -selected wavelengths. Scale bars = 1 mm.

4.5 REFERENCES

1. Emelianov, S.Y., Li, P.-C. & O'Donnell, M. Photoacoustics for molecular imaging and therapy. *Physics Today*, 34-39 (2008).
2. Kruger, R.A., Kiser, W.L., Reinecke, D.R. & Kruger, G.A. Thermoacoustic computed tomography using a conventional linear transducer array. *Medical Physics* **30**, 856-860 (2003).
3. Oraevsky, A.A., Jacques, S.L., Esenaliev, R.O. & Tittel, F.K., Vol. 2134 122 (1994).
4. Wang, X. et al. Noninvasive laser-induced photoacoustic tomography for structural and functional in vivo imaging of the brain. *Nature biotechnology* **21**, 803-806 (2003).
5. Ntziachristos, V., Ripoll, J., Wang, L.V. & Weissleder, R. Looking and listening to light: the evolution of whole-body photonic imaging. *Nature biotechnology* **23**, 313-320 (2005).
6. Hu, S. & Wang, L.V. Photoacoustic imaging and characterization of the microvasculature. *Journal of Biomedical Optics* **15**, 011101-011115 (2010).
7. Oh, J.-T. et al. Three-dimensional imaging of skin melanoma in vivo by dual-wavelength photoacoustic microscopy. *Journal of Biomedical Optics* **11**, 034032-034034 (2006).
8. Wang, B. et al. Detection of lipid in atherosclerotic vessels using ultrasound-guided spectroscopic intravascular photoacoustic imaging. *Opt. Express* **18**, 4889-4897 (2010).
9. Karpiouk, A.B., Wang, B., Amirian, J., Smalling, R.W. & Emelianov, S.Y. Feasibility of in vivo intravascular photoacoustic imaging using integrated ultrasound and photoacoustic imaging catheter. *Journal of Biomedical Optics* **17**, 1 (2012).
10. Wang, B. et al. In vivo intravascular ultrasound-guided photoacoustic imaging of lipid in plaques using an animal model of atherosclerosis. *Ultrasound in Medicine and Biology* **accepted** (2012).
11. Jose, J., Manohar, S., Kolkman, R.G.M., Steenbergen, W. & van Leeuwen, T.G. Imaging of tumor vasculature using Twente photoacoustic systems. *Journal of Biophotonics* **2**, 701-717 (2009).

12. Luke, G., Yeager, D. & Emelianov, S. Biomedical Applications of Photoacoustic Imaging with Exogenous Contrast Agents. *Annals of Biomedical Engineering*, 1-16 (2011).
13. Mallidi, S. et al. Multiwavelength Photoacoustic Imaging and Plasmon Resonance Coupling of Gold Nanoparticles for Selective Detection of Cancer. *Nano Letters* **9**, 2825-2831 (2009).
14. Wang, Y. et al. Photoacoustic Tomography of a Nanoshell Contrast Agent in the in Vivo Rat Brain. *Nano Letters* **4**, 1689-1692 (2004).
15. Homan, K.A. et al. Silver Nanoplate Contrast Agents for in Vivo Molecular Photoacoustic Imaging. *ACS Nano* **6**, 641-650 (2012).
16. Buehler, A., Herzog, E., Razansky, D. & Ntziachristos, V. Video rate optoacoustic tomography of mouse kidney perfusion. *Opt Lett* **35**, 2475-2477 (2010).
17. Mallidi, S., Larson, T., Aaron, J., Sokolov, K. & Emelianov, S. Molecular specific optoacoustic imaging with plasmonic nanoparticles. *Opt Express* **15**, 6583-6588 (2007).
18. Sethuraman, S., Amirian, J.H., Litovsky, S.H., Smalling, R.W. & Emelianov, S.Y. Spectroscopic intravascular photoacoustic imaging to differentiate atherosclerotic plaques. *Opt Express* **16**, 3362-3367 (2008).
19. Li, M.-L. et al. Simultaneous Molecular and Hypoxia Imaging of Brain Tumors In Vivo Using Spectroscopic Photoacoustic Tomography. *Anglais* **96** (2008).
20. Kim, S., Chen, Y.-S., Luke, G.P. & Emelianov, S.Y. In vivo three-dimensional spectroscopic photoacoustic imaging for monitoring nanoparticle delivery. *Biomed. Opt. Express* **2**, 2540-2550 (2011).
21. Levi, J. et al. Design, Synthesis, and Imaging of an Activatable Photoacoustic Probe. *Journal of the American Chemical Society* **132**, 11264-11269 (2010).
22. Razansky, D. et al. Multispectral Optoacoustic Tomography of Matrix Metalloproteinase Activity in Vulnerable Human Carotid Plaques. *Molecular Imaging and Biology*, 1-9 (2011).
23. Penrose, R. & Todd, J.A. On best approximate solutions of linear matrix equations. *Mathematical Proceedings of the Cambridge Philosophical Society* **52**, 17-19 (1956).

24. Guo, Z., Xu, Z. & Wang, L.V. Dependence of photoacoustic speckles on boundary roughness. *Journal of biomedical optics* **17**, 0460091-0460096 (2012).
25. Holzer, W. et al. Photostability and thermal stability of indocyanine green. *Journal of Photochemistry and Photobiology B: Biology* **47**, 155-164 (1998).
26. Myers, J.N., Holsinger, F.C., Jasser, S.A., Bekele, B.N. & Fidler, I.J. An Orthotopic Nude Mouse Model of Oral Tongue Squamous Cell Carcinoma. *Clinical Cancer Research* **8**, 293-298 (2002).
27. Luke, G.P., Nam, S.Y. & Emelianov, S.Y. Optical wavelength selection for improved spectroscopic photoacoustic imaging. *Photoacoustics* **1**, 36-42 (2013).
28. Xiao, J., Yuan, Z., He, J. & Jiang, H. Quantitative multispectral photoacoustic tomography and wavelength optimization. *Journal of X-ray science and technology* **18**, 415-427 (2010).
29. Bayer, C.L., Nam, S.Y., Chen, Y.-S. & Emelianov, S.Y. Photoacoustic signal amplification through plasmonic nanoparticle aggregation. *Journal of biomedical optics* **18**, 016001-016001 (2013).
30. Nam, S.Y., Ricles, L.M., Suggs, L.J. & Emelianov, S.Y. Nonlinear photoacoustic signal increase from endocytosis of gold nanoparticles. *Optics letters* **37**, 4708-4710 (2012).
31. Danielli, A., Maslov, K., Xia, J. & Wang, L.V. in Proc. of SPIE Vol, Vol. 8223 82233H-82231 (2012).
32. Cox, B., Laufer, J.G., Arridge, S.R. & Beard, P.C. Quantitative spectroscopic photoacoustic imaging: a review. *J Biomed Opt* **17**, 061202 (2012).
33. Jain, P.K., Lee, K.S., El-Sayed, I.H. & El-Sayed, M.A. Calculated Absorption and Scattering Properties of Gold Nanoparticles of Different Size, Shape, and Composition: Applications in Biological Imaging and Biomedicine. *The Journal of Physical Chemistry B* **110**, 7238-7248 (2006).
34. Homan, K. et al. Prospects of molecular photoacoustic imaging at 1064 nm wavelength. *Opt Lett* **35**, 2663-2665 (2010).
35. de la Zerda, A. et al. Ultrahigh sensitivity carbon nanotube agents for photoacoustic molecular imaging in living mice. *Nano Lett* **10**, 2168-2172 (2010).

Chapter 5: Single-Wavelength Lymph Node Mapping with Silica-Coated Gold Nanoplates

5.1 INTRODUCTION

Identifying the spread of cancer cells from the primary tumor is a critical factor for diagnosis and treatment planning. The standard of care for detection of cancer cells in the lymphatic system is a sentinel lymph node (SLN) biopsy.¹ In a typical SLN biopsy, a combination of an optically absorbing dye and a radioactive tracer is injected peritumorally and allowed to drain through the lymphatic vessels. The first lymph node to which the dye/tracer drains is known as the SLN. Histology is performed on the entire or part of the SLN to detect the presence of metastatic cancer cells. Although the procedure increases the survival of cancer patients, it often results in nerve damage and lymphedema.^{2,3}

A number of imaging methods, including magnetic resonance imaging, fluorescence imaging, and ultrasound (US) imaging, have been proposed to improve the accuracy and decrease the morbidity of SLN mapping.⁴⁻⁶ These methods, however, lack the resolution, imaging depth, or sensitivity which is desired for SLN mapping. Contrast enhanced photoacoustic (PA) imaging presents an excellent alternative because it is highly sensitive, real-time, and nonionizing.⁷⁻¹⁰ In addition, images can be acquired at clinically relevant depths with excellent resolution.¹¹

The fluid in the lymphatic system is minimally absorbing and thus provides no intrinsic PA contrast. Therefore, a contrast agent, such as a dye or nanoparticle, must be used to map the SLN.^{8, 9} Plasmonic nanoparticles are particularly promising for PA imaging because they are easily synthesized with a tunable peak optical absorption wavelength, are easily conjugated for molecular targeting, and have a molar optical

absorption that is five orders of magnitude greater than dyes.¹²⁻¹⁴ Anisotropic nanoparticles are commonly used in PA imaging applications because they absorb light in the red to near infrared range where the optical attenuation of tissue and endogenous PA signal are at a minimum.¹⁵ Previously, both gold and silver nanoplates have been proposed for PA imaging because of their high optical absorption, simple synthesis, and ability to be easily targeted to cellular receptors.^{13, 16, 17} Indeed, the large size of gold nanoplates means they have a higher per-particle absorption than nanorods and are well suited for drainage through the lymphatic system.¹⁸ These nanoparticles can be differentiated from the background endogenous absorbers either by observing a relative increase in signal or by performing spectroscopic PA imaging.^{8, 15, 16} The methods of localizing contrast agents, however, have limitations which will impede their eventual clinical translation. If the endogenous absorbers in the tissue produce a large PA signal, then measuring signal changes can become unreliable. Conversely, spectroscopic PA imaging requires significant increases in the complexity of the instrumentation and longer image acquisition times.

This chapter presents a new contrast agent for improved PA SLN mapping: silica-coated gold nanoplates (Si-AuNPs). These particles exhibit excellent PA contrast near their peak plasmon resonance. Therefore, the Si-AuNPs can be easily localized using only a single wavelength – 1064 nm – to acquire PA images. Thus, complicated imaging techniques are avoided. Furthermore, the silica coating provides a protective shell that preserves the thermodynamic stability of the particles during sustained PA imaging. By combining all of these useful characteristics, Si-AuNPs enable accurate, real-time visualization of the SLN.

5.2 MATERIALS AND METHODS

5.2.1 Synthesis of Silica-Coated Gold Nanoplates

All chemicals were used as received: chloroauric acid (HAuCl_4 , Sigma), trisodium citrate (TSC, Sigma), sodium borohydride (NaBH_4 , Acros), cetyltrimethylammoniumbromide (CTAB, Amresco), ascorbic acid (AA, Alpha Aesar), potassium iodide (KI, Fisher Scientific), sodium hydroxide (NaOH , JT Baker), methyl poly(ethylene glycol) thiol (mPEG-SH, MW 5000, Laysan Bio), isopropanol (IPA, Acros), tetraethyl orthosilicate (TEOS, Aldrich), ammonium hydroxide (NH_4OH , Fisher Scientific, 29% in water). Prior to synthesis, all glassware and stir bars were cleaned with aqua regia.

The synthesis of AuNPs was adapted from Ha, et al.¹⁹ To synthesize the gold seeds, 5 mL of HAuCl_4 (1 mM) and 5 mL of TSC (1 mM) were added to 10 mL of ultra-filtrated (18 M Ω -cm, Thermo Scientific Barnstead Diamond water purification system) deionized water (DIUF) under vigorous stirring (750 rpm) in a 20 mL glass scintillation vial. Then, 600 μL of ice-cold NaBH_4 (100 mM) was quickly added to the solution which resulted in a reddish-orange solution.

The second step involved preparation of the growth solution and the addition of a small quantity of seed solution to the growth solution. The growth solution began with dissolving 396 mL of CTAB (102 mM) at 30 °C in a 500 mL glass beaker under medium stirring (300 rpm). Then 4 mL of HAuCl_4 (25 mM) was added, causing the solution to turn yellow-orange. Then 400 μL of KI (10 mM) and 240 μL of NaOH (1 M) were added. Afterwards 8 mL of AA (100 mM) was added, which changed the solution from yellow-orange to colorless. The solution was heated to 35 °C and 1 mL of the seed solution was added.¹⁹ After 15 seconds, the beaker was removed from the hot plate and left undisturbed for 1 hour. The solution slowly changed from transparent to a deep violet over the course of approximately 5 minutes. After one hour, the solution was sealed with

Parafilm (Pechiney Plastic Packaging, Inc), placed on a hot plate set to 65 °C, and left overnight to allow for separation of the nanoplates from byproduct nanospheres in the solution. The following day, the solution was carefully aspirated without disturbing the sides and bottom of the glass beaker. The nanoplates, which had adhered to the bottom of the flask, were immediately resuspended in a relatively small volume (~5 mL) of DIUF and briefly sonicated.²⁰ Because the vast majority of the byproduct spheres had been removed, the resuspended solution exhibited a dark-green color.

PEGylation was performed immediately following resuspension of the particles. An equal volume of nanoplates diluted to a peak optical extinction coefficient of 15 cm⁻¹ and mPEG-SH solution (0.2 mM) were combined under vigorous stirring (750 rpm), sonicated for thirty seconds, and allowed to react overnight. The particles were then centrifuged at 20,000 rcf for 12 minutes, resuspended in DIUF and then underwent centrifugation filtration (100 kDa Amicon ultra-15, Millipore) at 2,500 rcf for 5 minutes to remove excess mPEG-SH.

Finally, a thin silica layer was added to the AuNPs using a modified Stöber method.²¹⁻²³ Under vigorous stirring (750 rpm), 1.2 mL of TEOS in IPA (3% by volume) and 1.2 mL of 29% NH₄OH in IPA (1.4% by volume) were added to 5 mL of nanoplates diluted to have a peak optical extinction coefficient of 6 cm⁻¹. The pH of the solution was measured to be approximately 10.9. The mixture was left to react for 2-5 hours. Longer reaction times led to thicker silica layers. Deposition of silica on the surface of the nanoplates could be confirmed through a shift in the peak extinction wavelength towards the near-infrared. The reaction was halted by combining the solution with an equal volume of DIUF and performing centrifugation filtration (100 kDa Amicon ultra-15, Millipore) at 2,500 rcf for 5 minutes. The resulting Si-AuNPs were resuspended in DIUF or Dulbecco's phosphate buffer solution (DPBS).

5.2.2 Characterization of Silica-Coated Gold Nanoplates

The optical properties of the gold nanoplates were characterized through ultraviolet-visible-near-infrared (UV-Vis-NIR) spectrophotometry using a UV-Vis-NIR spectrophotometer (UV-3600, Shimadzu). Morphological properties of the gold nanoplates were observed through transmission electron microscopy (TEM). To prepare the samples, copper-Formvar-carbon TEM grids were submerged in a solution of concentrated gold nanoplates for two minutes and allowed to dry in air. The grids were then imaged using the TEM mode of a Hitachi S-5500 FESEM with a field emission electron source operating at 30 kV.

5.2.3 Cytotoxicity of Si-AuNPs

A human pancreatic cancer cell line, L3.6pl, was incubated with the Si-AuNPs to test for cytotoxicity. The cell line was cultured using Dulbecco's modified eagle medium (DMEM, Sigma) (with 4500 mg glucose/L, L-glutamine, NaHCO₃, and pyridoxine HCl) supplemented with 10% fetal bovine serum (FBS, Sigma) and 1% penicillinstreptomycin (Pen/Strep, Invitrogen) while being maintained at 37 °C and 5% CO₂ in a humidified incubator. The cells were seeded in a 96 well plate (5000 cells in 100 μL of media). After allowing the cells to grow for 48 hours and attach to the plate, the media was removed and replaced with 100 μL of a combination of Si-AuNPs and media (with a peak optical extinction coefficient of 0, 0.2, 2, or 20 cm⁻¹). The cells were incubated with the Si-AuNPs for 48 hours. The media and Si-AuNPs were removed and 100 μL of fresh media was added. The extinction of each well in the plate was measured at 490 nm using a Synergy HT Multimode Microplate Reader (BioTek). Next, 20 μL of (3-(4,5-dimethylthiazol-2-yl)-5-(3-carboxymethoxyphenyl)-2-(4-sulfophenyl)-2H-tetrazolium) phenazine methosulfate (PMS) from the CellTiter 96 Aqueous Non-Radioactive Cell Proliferation Assay (Promega) was added to each well. After 75 minutes, the extinction at

490 nm was again measured. The increase in extinction was proportional to the number of viable cells in each well. A series of t-tests were used to identify statistically significant deviations in the proliferation with respect to the control wells.

5.2.4 Photothermal Stability

The thermal stability of Si-AuNPs and PEGylated AuNPs was studied through exposure to pulsed and continuous wave (CW) laser irradiation to simulate PA imaging and photothermal therapy (Figure 5.1a). Silica coated and uncoated nanoplates were placed in a 96-well plate at a concentration resulting in an optical extinction coefficient of 3 cm^{-1} . All trials were completed in triplicate. All of the wells were irradiated with a pulsed nanosecond laser (Quanta-Ray Pro, Spectra Physics) that was coupled to a tunable OPO laser system (Permiscan, GWU) set at 1064 nm with pulse repetition rate of 10 Hz and pulse duration of 5-7 ns. A control of 0 pulses was compared with both 300 and 1000 pulses at a fluence of 10 mJ/cm^2 . To study the stability of the particles under continuous wave irradiation, a continuous wave diode-pumped solid state laser (Opto Engine) operating at 1064 nm, with a fluence rate of 5 W/cm^2 was used. Each well was irradiated for between 0 and 3 minutes. After irradiation, 250 μL were recovered from each well, diluted with DIUF to a final volume of 2.5 mL, and characterized with UV-Vis-NIR spectrophotometry and TEM.

5.2.5 In Vivo Sentinel Lymph Node Mapping

All animal studies were approved by the Institutional Animal Care and Use Committee (IACUC) at The University of Texas at Austin. Homozygous Nu/Nu female mice, age 57-70 days were purchased from Charles River Laboratories. The mice were imaged using a Vevo 2100 high frequency ultrasound imaging system (VisualSonics) with an MS-550 40-MHz, 256-element linear array transducer (Figure 5.1b). A pulsed

nanosecond laser (Quanta-Ray Pro, Spectra Physics) was coupled to a tunable OPO laser system (Permiscan, GWU) to provide the 1064-nm optical source for imaging. A laser fluence of 10 mJ/cm² was used for all in-vivo imaging. During imaging, the mice were anesthetized with a mixture of isoflurane and oxygen (1.5%). Clear ultrasound gel was used to couple the transducer to the neck of the mouse. USPA images were acquired in a 3-D volume surrounding the cervical lymph nodes. During imaging, the heart rate, respiration rate, and body temperature were monitored.

Following the initial imaging, the mice were injected with 40 μ L of sterile Si-AuNPs (peak optical extinction coefficient of 20 cm⁻¹ in PBS) submucosally in the tongue. USPA images were continuously collected in the same 3-D imaging volume immediately following the injection for up to 4 hours. Imaging was performed again at 24 and 48 hours after the Si-AuNP injection. Immediately following the final imaging session, the mice were sacrificed via an isoflurane overdose (5%) and cervical dislocation.

5.3 RESULTS AND DISCUSSION

5.3.1 Silica-Coated Gold Nanoplate Synthesis and Characterization

The Si-AuNPs were synthesized via procedures adapted from Ha, et al.^{19, 20} and Chen, et al.²² (Figure 5.2a). First, gold seeds (ca. 2 nm) were synthesized by reducing HAuCl₄ with NaBH₄. The seeds were added to a growth solution containing KI, NaOH, HAuCl₄, AA, and CTAB. After 30 minutes, the solution had changed from clear to dark violet and contained a mixture of triangular AuNPs and Au nanospheres. The peak absorption of the AuNPs was centered at 945 nm. After separation of AuNPs from the contaminating nanospheres, the peak shifted to 1035 nm (Figure 5.2b) – the shift was most likely due to the removal of smaller AuNPs with the nanospheres. Transmission

electron microscopy indicated a mean AuNP edge length of 96 ± 5 nm (Figure 5.2c). The Si-AuNPs were made by adding a 20-nm layer of silica to the AuNPs via a modified Stöber method (Figure 5.2d).^{21, 22} This resulted in a spectral shift of approximately 20 nm towards the near infrared (Figure 5.2b). The particles were stable for several weeks in an aqueous solution at room temperature.

5.3.2 Cytotoxicity of Silica-Coated Gold Nanoplates

The cytotoxicity of the Si-AuNPs was evaluated with an MTS assay. The particles were incubated with pancreatic cancer cells for 48 hours at concentrations resulting in peak absorption coefficients ranging from 0.2 to 2 to 20 cm^{-1} . A series of student's t-tests were used to determine that there was no statistically significant loss in viability ($p > 0.1$) in the cells when compared to the control (Figure 5.3). The low amounts of cytotoxicity observed even at high concentrations indicates that the CTAB used in synthesis had been successfully removed and that the Si-AuNPs are well-suited for *in vivo* imaging applications.

5.3.3 Photothermal Stability of Silica-Coated Gold Nanoplates

The stability of PEGylated Si-AuNPs was assessed after exposure to pulsed and continuous wave laser irradiation in order to evaluate their suitability for PA imaging and photothermal therapy. PEGylated AuNPs showed poor stability when irradiated with a 1064-nm nanosecond pulsed laser at a fluence of 10 mJ/cm^2 (Figure 5.4a). Indeed, after 1000 laser pulses the absorption of the AuNPs decreased by 45%. This is a direct result of thermal damage to the particles and a tendency to reform as more thermally stable sphere-like particles (Figure 5.4a, inset). A 20-nm layer of silica, however, stabilized the particles, allowing the Si-AuNPs to withstand the pulsed laser irradiation with little degradation (Figure 5.4b). Very few changes in particle morphology were observed in the

TEM images (Figure 5.4b, inset). These results indicate that Si-AuNPs remain stable when exposed to typical PA imaging conditions. Previous studies have indicated that the improved stability is likely a result of more efficient thermal exchange between the AuNP and the surrounding aqueous environment facilitated by a decreased interfacial heat resistance.²⁴ An added benefit of the more efficient exchange is in enhanced PA signal.²³

A similar trend of improved stability was evident when the particles were exposed to CW laser irradiation (Figure 5.4c-d). After 3 minutes of exposure to a CW 1064-nm laser, the absorption of PEGylated AuNPs decreased by 49%, while virtually no changes were observed in the Si-AuNPs. Thus, the Si-AuNPs show great promise to be used as theranostic agents (i.e., combining PA imaging and photothermal therapy).

5.3.4 *In Vivo* Sentinel Lymph Node Mapping

For SLN imaging, a model of squamous cell carcinoma of the oral cavity was adapted; however, only normal (non-tumor-bearing mice) were used in this study.²⁵ Combined ultrasound and photoacoustic (USPA) imaging was performed on the cervical lymph nodes located near the salivary glands of the mice. The Si-AuNPs were injected into the tongue of the mouse and were allowed to drain to the cervical lymph nodes while the mouse remained immobilized under anesthesia.

The cervical lymph nodes are easily identified with US imaging as a dark, hypoechoic bean-shaped region (Figure 5.5a-b). Thus, US imaging provides an excellent method to guide and provide an anatomical reference for subsequent PA imaging (which provides minimal inherent signal at the chosen optical wavelength and fluence). Photoacoustic images acquired before the injection of Si-AuNPs (Figure 5.5a) show that the endogenous PA signal (originating from the blood and skin in the mouse) is very

small and not detectable with our imaging system. This is due to the low absorption of these components at 1064 nm and the magnitude of laser fluence used in this imaging experiment (10 mJ/cm^2).²⁶ Because there is no discernible PA signal before the injection of Si-AuNPs, any signal after the injection can be attributed to the nanoparticles. As a result, the Si-AuNPs can be tracked with high specificity. Figure 5.5c shows overlaid US and PA images 4 hours after the injection of Si-AuNPs. The location of Si-AuNPs is mapped within the SLN, allowing for high contrast identification of the SLN in the USPA image.

By scanning the transducer in the out-of-plane direction, a three-dimensional (3-D) USPA image was acquired (Figure 5.5d-e). The 3-D image shows the volumetric distribution of the Si-AuNPs in the SLN as well as a lymphatic vessel feeding into the SLN (Figure 5.5e, arrow). Thus, this technology could be used to aid clinicians in identifying and localizing the SLN and visualizing the afferent lymph vessels. The Si-AuNPs resisted major degradation and the signal persisted even after exposure to five hours of pulsed laser light. The strong PA signal indicates that Si-AuNPs are stable in a biological environment and well-suited for in vivo applications.

In order to study the drainage kinetics of the Si-AuNPs, we acquired 3-D USPA images of the region surrounding the SLN continuously for 165 minutes following their injection (Figure 5.6). The results show that the Si-AuNPs are immediately delivered to a localized portion near the top of the SLN, and then they continue to drain to and diffuse one edge of the node. After 2.5 hours following the injection, the Si-AuNPs are distributed throughout approximately 20% of the SLN (Figure 5.6e). The average PA signal in the SLN was highly correlated with the volume of the node that contained detectable PA signal (Figure 5.6e). This suggests that as new Si-AuNPs steadily flowed

into the SLN, they also spread throughout the node at a similar rate (i.e., there was no significant “pooling” of the particles).

There are many benefits of tuning the Si-AuNPs to 1064 nm. The endogenous absorption, and thus the background PA signal, at 1064 nm is much lower than other common PA imaging wavelengths (700-900 nm). Indeed, by simply choosing 1064 as the imaging wavelength, a 38% improvement in contrast can be achieved.²⁶ The low endogenous absorption also removes the need for multi-wavelength imaging and spectral unmixing to accurately differentiate endogenous and exogenous PA signal. In the case of our experiments, the endogenous signal was below the noise level, so the entire PA image can be attributed to Si-AuNPs. The decreased absorption and scattering also allow for higher levels of laser exposure and better penetration in tissue. In fact, the safe level of human skin exposure to a pulsed laser source as determined by the American National Standards Institute is 100 mJ/cm² (versus 20 mJ/cm² in the visible range). Thus, Si-AuNPs could be used for imaging at much greater depths than other particles or dyes commonly used for SLN mapping. Finally, inexpensive, high-energy solid state lasers are available at 1064 nm. This provides a cost-effective method for the eventual clinical translation of this technology.

5.4 CONCLUSIONS

A new contrast agent for PA imaging – Si-AuNPs – have been demonstrated excellent particles for PA image-guided SLN mapping. The Si-AuNPs have proven to be more stable under laser irradiation than PEGylated AuNPs, making them better suited for sustained PA imaging. In addition, the drainage kinetics of Si-AuNPs through the lymphatic system makes them well-suited to act as a contrast agent for PA image-guided

SLN mapping. Furthermore, their long retention in the SLN suggests they may provide an excellent alternative to small-molecule dyes, which quickly drain out of the SLN.

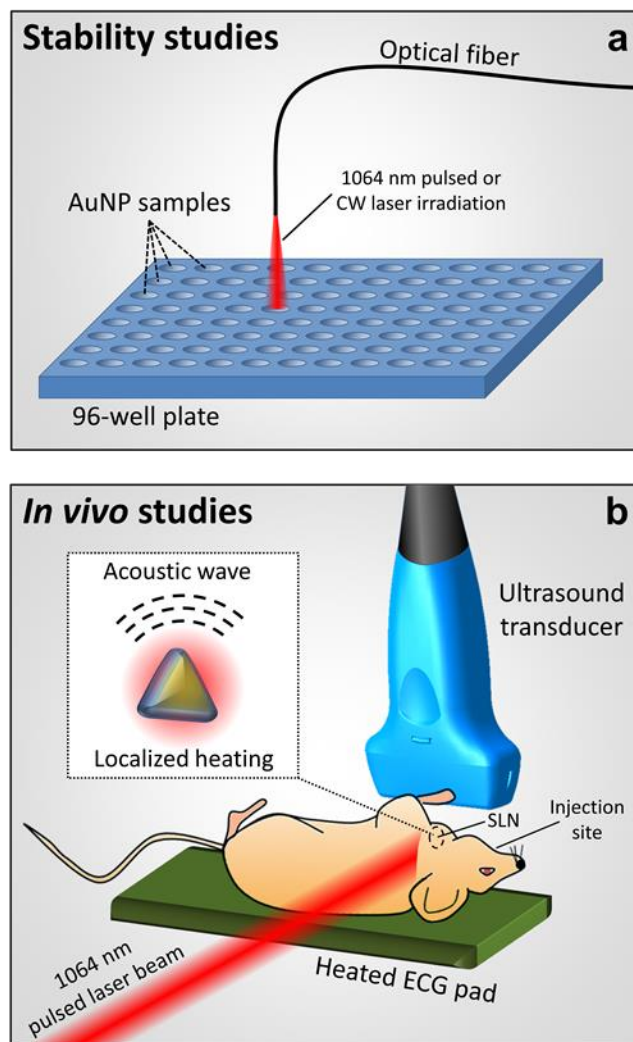


Figure 5.1 a) Experimental setup to study the stability of AuNPs and Si-AuNPs, and b) experimental setup for in vivo studies. The pulsed laser induces localized heating near the Si-AuNPs which results in the generation of acoustic waves centered at the Si-AuNPs (b, inset).

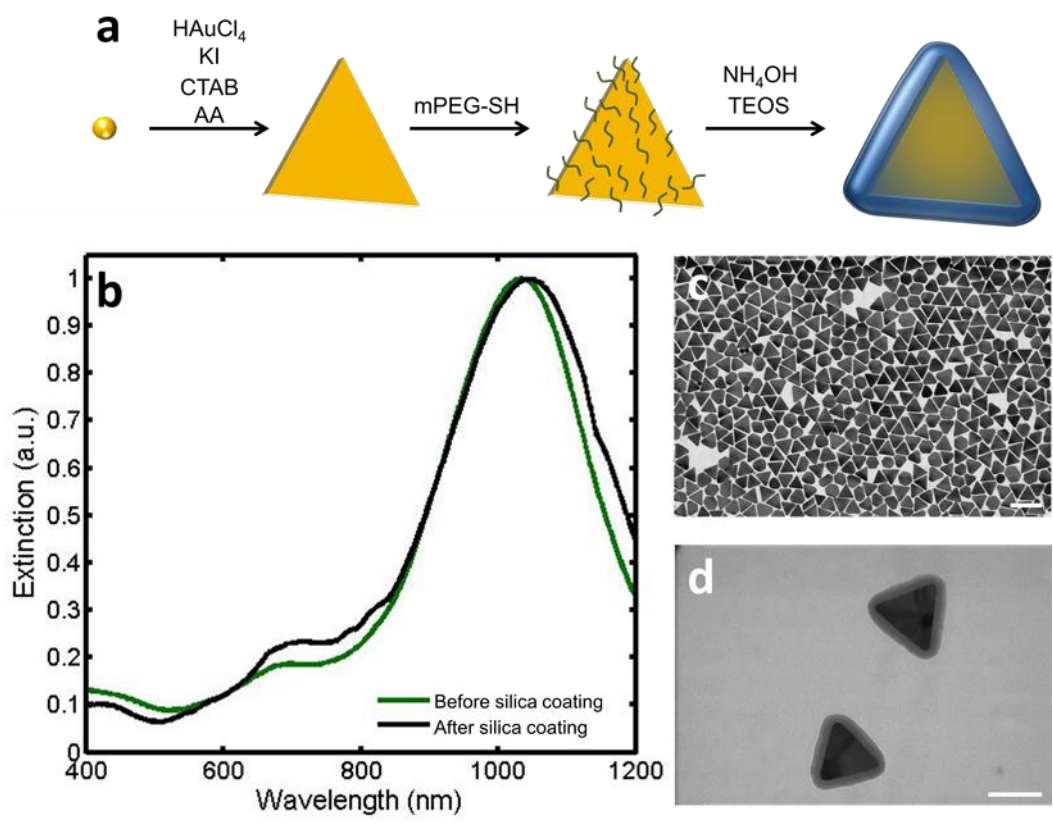


Figure 5.2 a) Schematic showing the synthesis of Si-AuNPs. b) UV-Vis-NIR spectra of NPs before (green) and after silica coating (black). c) A TEM image of AuNPs shows an even size distribution (scale bar = 200 nm). d) A TEM image of Si-AuNPs (scale bar = 100 nm).

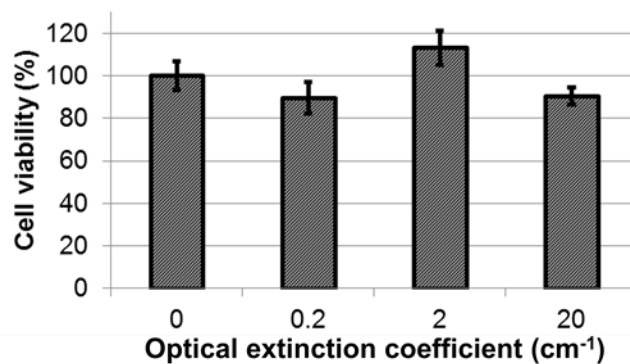


Figure 5.3 An MTS assay shows no significant cytotoxicity of Si-AuNPs at concentrations with optical extinction coefficients up to 20 cm⁻¹ in comparison to control.

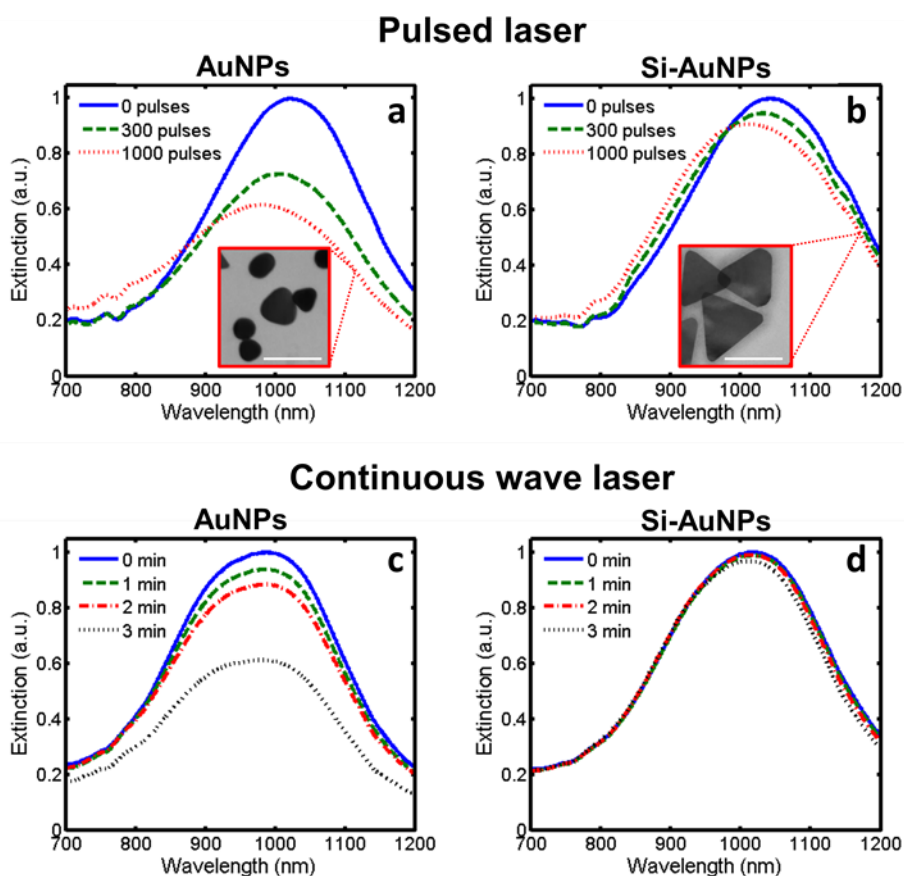


Figure 5.4 UV-Vis-NIR spectra showing the degradation of PEGylated AuNPs and Si-AuNPs to a,b) pulsed laser irradiation at 10 mJ/cm^2 and c,d) continuous wave laser irradiation at 1.3 W/cm^2 . The pulsed laser caused significant changes in the morphology of PEGylated AuNPs (a, inset) while Si-NPs with a 20-nm layer of silica showed few changes in shape (b, inset). Scale bars = 100 nm.

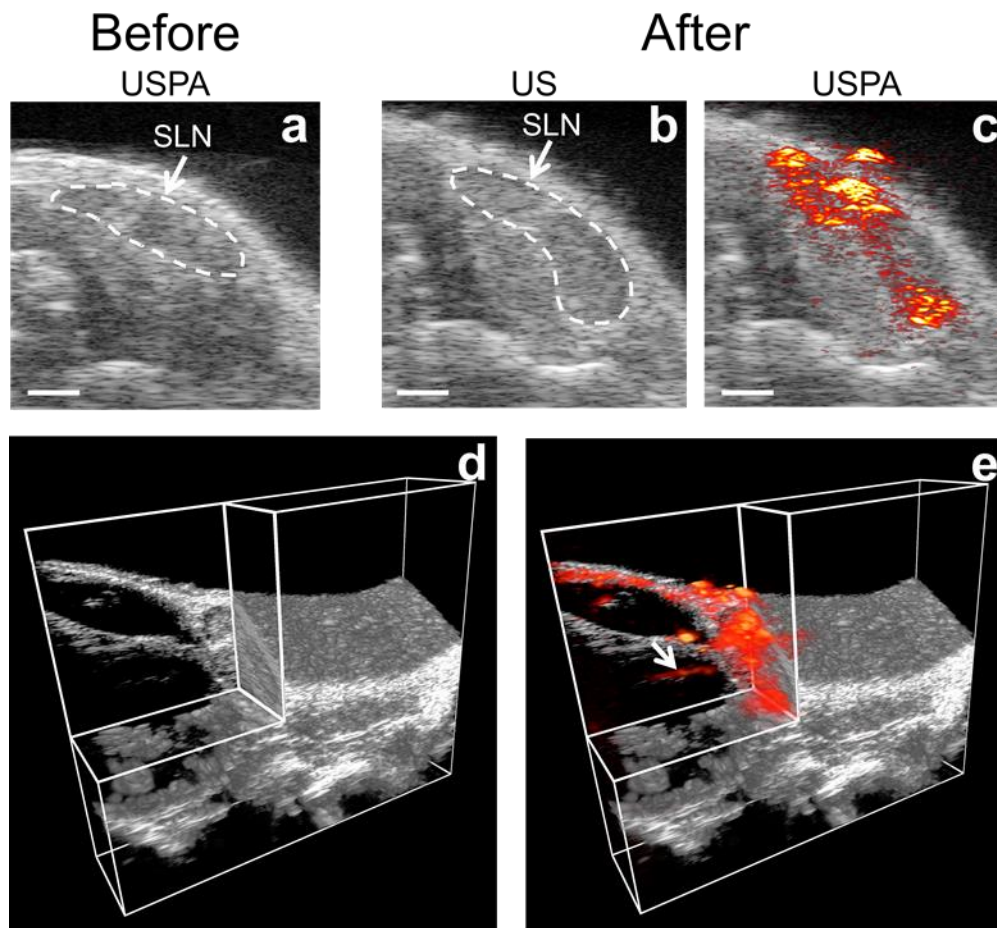


Figure 5.5 a) Overlaid USPA images of a 2-D slice containing the SLN before the injection of Si-AuNPs. The endogenous PA signal is below the noise floor of the system. b) A US image 4 hours after the injection of Si-AuNPs with the SLN identified. c) The same US image as in b) with the PA image overlaid shows a strong PA signal throughout the SLN. d) A 3-D US image with a quadrant removed shows the anatomy surrounding the SLN. e) A 3-D PA image acquired 4 hours after the injection of Si-AuNPs overlaid on the US image shows the distribution of Si-AuNPs in the SLN and reveals an afferent lymph vessel (arrow). Scale bars = 1 mm.

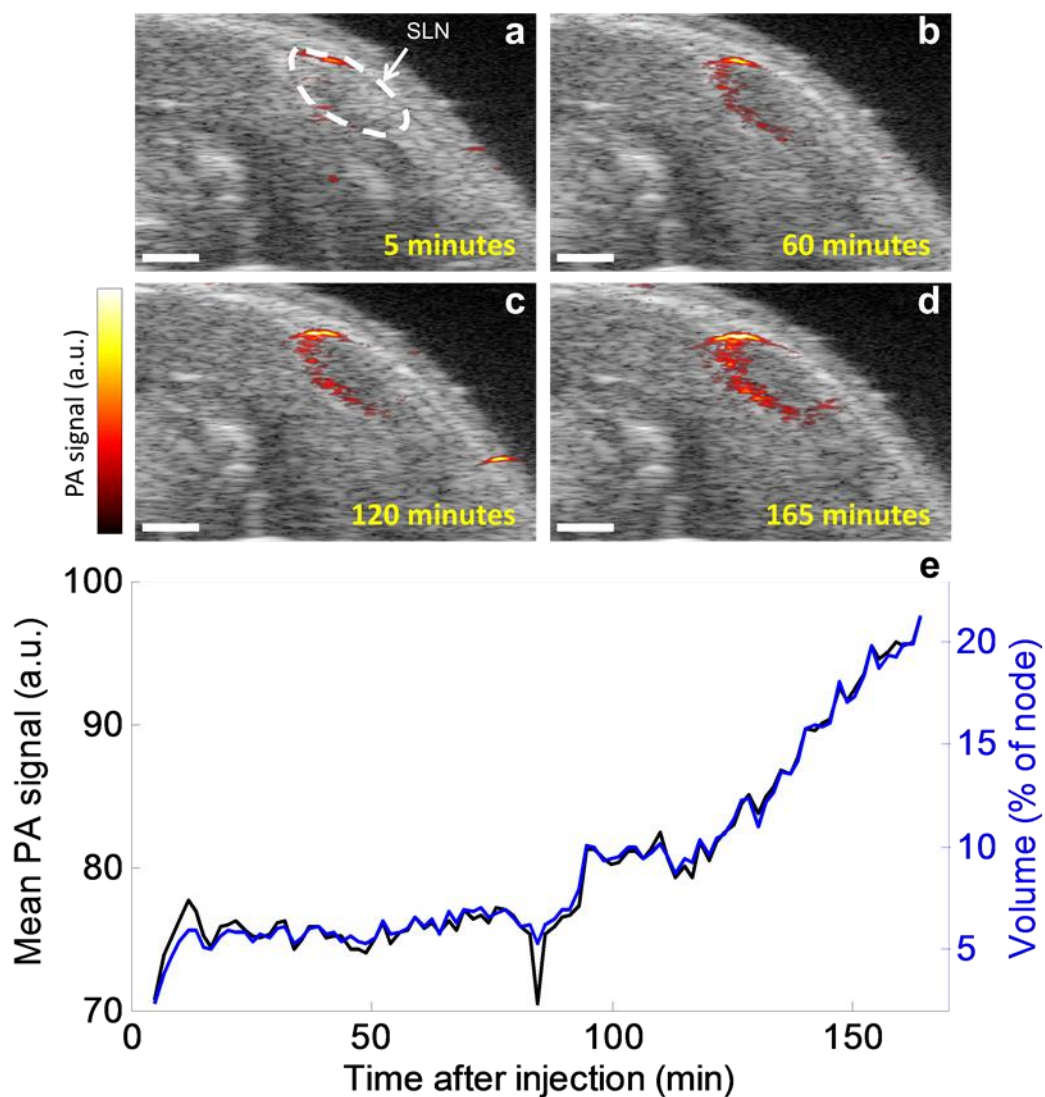


Figure 5.6 a-d) Combined USPA images of a 2-D slice immediately following the injection of Si-AuNPs. After being quickly delivered to the SLN, the signal slowly spreads throughout the node. e) the average PA signal (black) and volume of the lymph node that contained detectable PA signal (blue) in the SLN increase steadily over the course of 165 minutes after the injection. Scale bars = 1 mm.

5.5 REFERENCES

1. Veronesi, U. et al. Sentinel-node biopsy to avoid axillary dissection in breast cancer with clinically negative lymph-nodes. *Lancet* **349**, 1864-1867 (1997).
2. Goldberg, J., Riedel, E., Morrow, M. & Van Zee, K. Morbidity of Sentinel Node Biopsy: Relationship Between Number of Excised Lymph Nodes and Patient Perceptions of Lymphedema. *Annals of Surgical Oncology* **18**, 2866-2872 (2011).
3. Langer, I. et al. Morbidity of Sentinel Lymph Node Biopsy (SLN) Alone Versus SLN and Completion Axillary Lymph Node Dissection After Breast Cancer Surgery: A Prospective Swiss Multicenter Study on 659 Patients. *Annals of Surgery* **245**, 452-461 (2007).
4. Mao, Y.P. et al. The N staging system in nasopharyngeal carcinoma with radiation therapy oncology group guidelines for lymph node levels based on magnetic resonance imaging. *Clinical cancer research* **14**, 7497-7503 (2008).
5. Kim, S. et al. Near-infrared fluorescent type II quantum dots for sentinel lymph node mapping. *Nat Biotechnol* **22**, 93-97 (2004).
6. Richards, P.S. & Peacock, T.E. The role of ultrasound in the detection of cervical lymph node metastases in clinically N0 squamous cell carcinoma of the head and neck. *Cancer Imaging* **7**, 167-178 (2007).
7. Luke, G., Yeager, D. & Emelianov, S. Biomedical Applications of Photoacoustic Imaging with Exogenous Contrast Agents. *Annals of Biomedical Engineering*, 1-16 (2011).
8. Song, K.H., Kim, C., Cobley, C.M., Xia, Y. & Wang, L.V. Near-Infrared Gold Nanocages as a New Class of Tracers for Photoacoustic Sentinel Lymph Node Mapping on a Rat Model. *Nano Letters* **9**, 183-188 (2008).
9. Song, K.H., Kim, C., Maslov, K. & Wang, L.V. Noninvasive in vivo spectroscopic nanorod-contrast photoacoustic mapping of sentinel lymph nodes. *European Journal of Radiology* **70**, 227-231 (2009).
10. Hu, S., Maslov, K., Tsytsarev, V. & Wang, L.V. Functional transcranial brain imaging by optical-resolution photoacoustic microscopy, Vol. 14. (SPIE, 2009).
11. Wang, L.V. Multiscale photoacoustic microscopy and computed tomography. *Nat Photonics* **3**, 503-509 (2009).

12. Hu, M. et al. Gold nanostructures: engineering their plasmonic properties for biomedical applications. *Chemical Society Reviews* **35**, 1084-1094 (2006).
13. Kumar, S., Aaron, J. & Sokolov, K. Directional conjugation of antibodies to nanoparticles for synthesis of multiplexed optical contrast agents with both delivery and targeting moieties. *Nature Protocols* **3**, 314-320 (2008).
14. Jain, P.K., Lee, K.S., El-Sayed, I.H. & El-Sayed, M.A. Calculated Absorption and Scattering Properties of Gold Nanoparticles of Different Size, Shape, and Composition: Applications in Biological Imaging and Biomedicine. *The Journal of Physical Chemistry B* **110**, 7238-7248 (2006).
15. Kim, S., Chen, Y.-S., Luke, G.P. & Emelianov, S.Y. In vivo three-dimensional spectroscopic photoacoustic imaging for monitoring nanoparticle delivery. *Biomed. Opt. Express* **2**, 2540-2550 (2011).
16. Homan, K.A. et al. Silver Nanoplate Contrast Agents for in Vivo Molecular Photoacoustic Imaging. *ACS Nano* **6**, 641-650 (2012).
17. Bao, C. et al. Gold Nanoprisms as Optoacoustic Signal Nanoamplifiers for In Vivo Bioimaging of Gastrointestinal Cancers. *Small* **9**, 68-74 (2013).
18. Cai, X. et al. In vivo quantitative evaluation of the transport kinetics of gold nanocages in a lymphatic system by noninvasive photoacoustic tomography. *ACS Nano* **5**, 9658-9667 (2011).
19. Ha, T.H., Koo, H.-J. & Chung, B.H. Shape-Controlled Syntheses of Gold Nanoprisms and Nanorods Influenced by Specific Adsorption of Halide Ions. *The Journal of Physical Chemistry C* **111**, 1123-1130 (2006).
20. Ha, T.H., Kim, Y.J. & Park, S.H. Complete separation of triangular gold nanoplates through selective precipitation under CTAB micelles in aqueous solution. *Chemical Communications* **46**, 3164-3166 (2010).
21. Stöber, W., Fink, A. & Bohn, E. Controlled growth of monodisperse silica spheres in the micron size range. *Journal of Colloid and Interface Science* **26**, 62-69 (1968).
22. Chen, Y.S. et al. Enhanced thermal stability of silica-coated gold nanorods for photoacoustic imaging and image-guided therapy. *Opt Express* **18**, 8867-8878 (2010).
23. Chen, Y.-S. et al. Silica-coated gold nanorods as photoacoustic signal nanoamplifiers. *Nano letters* **11**, 348-354 (2011).

24. Chen, Y.-S., Frey, W., Aglyamov, S. & Emelianov, S. Environment-Dependent Generation of Photoacoustic Waves from Plasmonic Nanoparticles. *Small* **8**, 47-52 (2012).
25. Myers, J.N., Holsinger, F.C., Jasser, S.A., Bekele, B.N. & Fidler, I.J. An Orthotopic Nude Mouse Model of Oral Tongue Squamous Cell Carcinoma. *Clinical Cancer Research* **8**, 293-298 (2002).
26. Homan, K. et al. Prospects of molecular photoacoustic imaging at 1064 nm wavelength. *Opt Lett* **35**, 2663-2665 (2010).

Chapter 6: Conclusions and Future Outlook

6.1 SUMMARY

With the ever-expanding selection of molecular-based therapies for cancer, the need for accurate identification of molecular expressions in diseased and normal tissue continues to grow. The current standard of care – a biopsy followed by immunohistochemistry – suffers from many limitations, including sampling error, patient side effects, and delayed results.

The work in this dissertation has focused on improving molecular imaging technology – specifically photoacoustic (PA) imaging – and its application to realistic cancer models to enable highly sensitive of molecular expressions *in vivo*. Although much of the work focused on a specific application (i.e., the detection of cervical metastases in oral cancer), the concepts can be generalized to a variety of cancer applications. This dissertation presents a framework that allows for the sensitive and selective detection of micrometastases in the lymphatic system by observing functional changes and molecular expressions with spectroscopic photoacoustic (sPA) imaging. Chapter 1 provided an overall rationale for the need of molecular imaging in oncology, an overview of molecular imaging modalities, and how molecular imaging could be used in the detection of lymph node metastases. Chapter 2 presented results that indicate sPA imaging can detect lymph node metastasis in a mouse model of squamous cell carcinoma of the oral cavity (SCCOC) without the use of exogenous contrast agents. Functional changes in metastatic nodes (i.e., hypoxia) were detected in nodes harboring metastases larger than 150 μm were detected. However, smaller metastases and metastases that were adjacent to the lymph nodes remained occult. Chapter 3 addressed this shortcoming by introducing molecularly-targeted contrast agents: molecularly-activated plasmonic

nanosensors (MAPS). The MAPS, which become visible in sPA imaging only after cancer cells selectively internalize them, were used to detect micrometastatic foci as small as 50 μm . This unprecedented sensitivity suggests that the particles may significantly impact the detection and characterization of small colonies of malignant cells. Chapters 4 and 5 focused on the improvement of spectroscopic techniques and nanoparticle formulations, respectively. These both serve to improve the ability to resolve the exogenous contrast agents in the presence of endogenous tissue.

6.2 THE IMPACT OF MOLECULAR IMAGING OF MICROMETASTASES

A major finding presented in this work is the ability of sPA imaging to detect small colonies of cancerous cells in the lymphatic system. Because accurate determination of the extent of spread of a tumor is necessary for charting the best course of treatment, these results could have a significant impact on cancer staging. In the meantime, sPA imaging of MAPS comprises a useful tool that could be used in preclinical models to identify molecular expressions and response to therapy.

6.2.1 Preclinical Implications

Small animal imaging has become an essential tool in developing an understanding of cancer and its response to emerging therapeutics. Optical imaging techniques have been at the forefront of the field, but PA imaging is beginning to make an impact with its unique set of benefits (e.g., high resolution at depth).¹ As our understanding of the tumor microenvironment becomes more and more complex, there is a need to be able to visualize the dynamics of molecular expression with high resolution.² The work presented in this dissertation has the potential to enable accurate visualization of cell surface receptors in response to disease progression or therapy. The end result will be an improved understanding of cancer and streamlined evaluation of new drugs.

6.2.2 The Clinical Future

The clinical translation of any new technology is a long, arduous process where success is by no means guaranteed. This is especially true when it involves the administration of a new drug or imaging agent. Therefore, label-free sPA imaging would provide the most worthwhile avenue to pursue for rapid clinical acceptance of photoacoustic imaging. Indeed, PA imaging has not yet raised any health concerns; it only uses nonionizing radiation and its laser intensity levels are widely considered to be safe. In fact, preliminary clinical studies of breast cancer detection using PA imaging of elevated hemoglobin are already underway.³ Given the promising preclinical results presented in Chapter 1, a clinical imaging study on a small cohort of patients should be initiated immediately. Because a mouse model of SCCOC was used in Chapter 1, it follows that initial clinical studies should focus on the same disease. That way, conclusions can more readily be drawn between the two results.

Head and neck cancer patients electing to undergo lymph node resection will be recruited to participate in the study. Prior to surgery, combined ultrasound (US) and sPA imaging will be performed of the cervical lymph nodes. Ultrasound imaging will be used to measure morphological parameters, including lymph node volume and shape, and functional parameters, including blood flow. Because US imaging has been used extensively on metastatic cervical lymph nodes, the results from this study could be compared to previous results.⁴ Spectroscopic photoacoustic imaging will add the spatial distribution of tissue oxygenation in the node. Once the nodes are resected, the results of US and sPA imaging will be compared to the histology.

Even though the timescale for clinical translation of the MAPS is longer than label-free photoacoustics, it can potentially lead to a greater impact. Not only did it exhibit higher sensitivity and specificity in the preclinical model, but it also be tailored to

identify molecular targets for a personalized treatment plan. In spite of its promise, more work must be done in the preclinical real before it can be translated to humans. The current formulation of MAPS uses 40-nm gold spheres. However, particles larger than 5 nm tend to accumulate indefinitely in the spleen and liver of mice.⁵ The lack of *in vivo* clearance would severely threaten the success of clinical trials.

To address this problem, the gold nanoparticles could be scaled down to 5 nm to facilitate renal clearance. These small particles have been shown to have a short half-life in the blood. This restricts their applicability to molecular imaging with an intravenous injection, but it is synergistic with the lymph node imaging procedure in Chapter 3. Because the procedure uses direct delivery through the lymphatic system, blood clearance should not severely limit the delivery of the MAPS. Further preclinical studies will aim to show three critical results: 1) the smaller MAPS still result in high sensitivity and specificity with a reasonable dose of gold, 2) the MAPS are effectively cleared from the lymphatic system, and 3) the MAPS show excellent clearance from the body in a reasonable timeframe. Once these results are demonstrated, translational studies can be initiated.

6.3 BEYOND DIAGNOSTICS: IMAGE-GUIDED THERAPY

Although sensitive detection of metastases is critical to the treatment of cancer, the fact remains that the end goal is eradication of the disease. The fact of the matter is that even if molecular imaging were to detect lymph node metastases, the very next step in the clinic today would be the removal of the affected node. Indeed, removal of metastatic nodes leads to increased survival rates.⁶ However, this procedure involves the removal of a great deal of healthy tissue as well and can lead to lymphedema or nerve damage.⁷

Photothermal therapy (PTT) has recently been proposed as an alternative to the surgical resection of primary tumors and is currently undergoing clinical trials.⁸ It works by remotely heating plasmonic nanoparticles with a continuous wave laser. It can be envisioned that immediately following detection of micrometastases with MAPS, PTT could be used to destroy the foci. This could either be done using the exact same MAPS that were used in the detection with a laser in the 700-nm range, or a separate injection of particles absorbing in the near infrared could be used for better efficiency and less heating of healthy tissue.

Photoacoustic imaging provides an excellent tool to guide PTT. The PA signal amplitude is proportional to the temperature in water-based tissue. Therefore, as the particles are heated, the temperature can be tracked in real-time and with high resolution to estimate the thermal dose.⁹ Preliminary results of PTT in the cervical lymph nodes of mice using epidermal growth factor receptor targeted copper sulfide nanoparticles as contrast agents show that significant heating can be achieved in the lymph node when a 1064-nm laser is applied to the region (Figure 6.1). Future studies will focus on optimizing the procedure and determining its therapeutic effect. The end result could be a streamlined diagnosis and treatment that could all be done noninvasively and in real-time.

6.4 IMPROVED MOLECULAR IMAGING WITH OPTIMIZED NANOPARTICLE CONTRAST AGENTS

As is evidenced in this dissertation, plasmonic nanoparticles make excellent contrast agents for PA imaging. This is owing to their large optical absorption, easily functionalized surface, and tunable optical properties. It is generally accepted that tuning these nanoparticles to absorb in the red to near infrared region results in the best contrast, with particles absorbing near 1064 nm resulting in the best contrast, as evidenced in Chapter 5 and in the literature.¹⁰

However, when sPA imaging is used, the optimal wavelength is no longer clear-cut. An interesting correlary of the results in Chapter 5 is that the spectral properties of contrast agents can be optimized to enhance their ability to be differentiated from native tissue. This can be done by monitoring the smallest singular value of the molar absorption matrix while varying the spectrum of the nanoparticles. Initial simulations suggest that when the spectral range of 680 to 970 nm is used, nanoparticles with a narrow absorption peak near 800 nm are easiest to differentiate from hemoglobin, while nanoparticles absorbing near 900 nm are particularly difficult (Figure 6.2). Future studies will confirm this result *in vivo* by imaging drainage of 800-nm or 900-nm absorbing silica-coated gold nanorods to the cervical lymph nodes of mice. Photoacoustic microscopy of the excised nodes will be used to validate the distribution of nanoparticles.

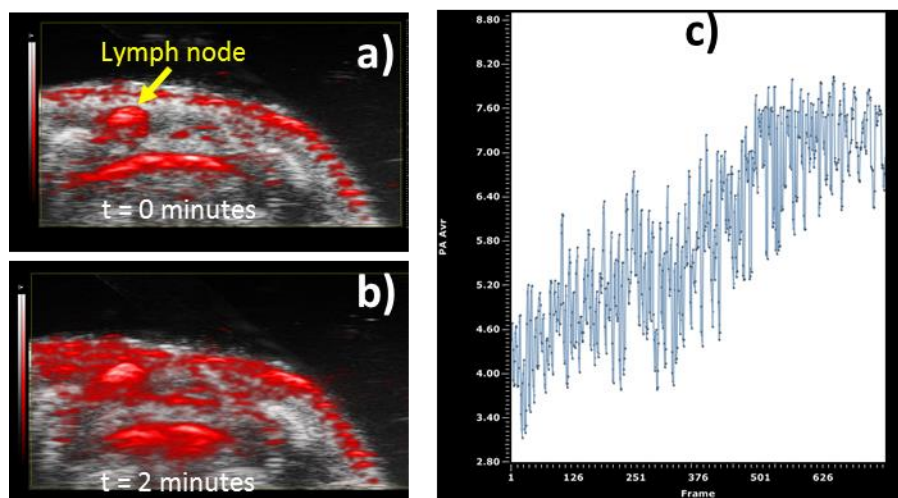


Figure 6.1 A combined US/PA image of a mouse with EGFR-targeted CuS nanoparticles in the lymph node before (a) and after (b) 2 minutes of exposure to 1064 nm continuous wave laser irradiation. The PA signal in the lymph node (c) increases as the temperature rises.

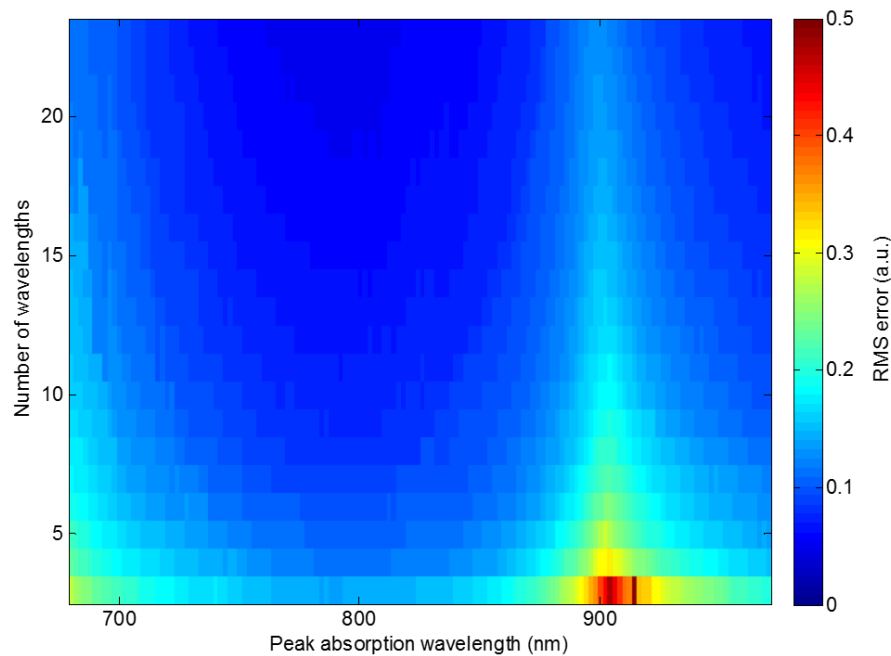


Figure 6.2 The error in unmixing a contrast agent from blood depends on the spectrum of the contrast agent. A peak absorption near 800 nm is best for the given spectral range.

6.5 REFERENCES

1. Ntziachristos, V., Ripoll, J., Wang, L.V. & Weissleder, R. Looking and listening to light: the evolution of whole-body photonic imaging. *Nature biotechnology* **23**, 313-320 (2005).
2. Gerlinger, M. et al. Intratumor heterogeneity and branched evolution revealed by multiregion sequencing. *New England Journal of Medicine* **366**, 883-892 (2012).
3. Manohar, S. et al. Initial results of in vivo non-invasive cancer imaging in the human breast using near-infrared photoacoustics. *Opt. Express* **15**, 12277-12285 (2007).

4. Richards, P.S. & Peacock, T.E. The role of ultrasound in the detection of cervical lymph node metastases in clinically N0 squamous cell carcinoma of the head and neck. *Cancer Imaging* **7**, 167-178 (2007).
5. Khlebtsov, N. & Dykman, L. Biodistribution and toxicity of engineered gold nanoparticles: a review of in vitro and in vivo studies. *Chemical Society Reviews* **40**, 1647-1671 (2011).
6. Morton, D.L. et al. Sentinel-node biopsy or nodal observation in melanoma. *New England Journal of Medicine* **355**, 1307-1317 (2006).
7. Goldberg, J., Riedel, E., Morrow, M. & Van Zee, K. Morbidity of Sentinel Node Biopsy: Relationship Between Number of Excised Lymph Nodes and Patient Perceptions of Lymphedema. *Annals of Surgical Oncology* **18**, 2866-2872 (2011).
8. Kennedy, L.C. et al. A New Era for Cancer Treatment: Gold-Nanoparticle-Mediated Thermal Therapies. *Small* **7**, 169-183 (2011).
9. Kim, S. et al. in Ultrasonics Symposium (IUS), 2010 IEEE 233-236 (2010).
10. Homan, K. et al. Prospects of molecular photoacoustic imaging at 1064 nm wavelength. *Opt Lett* **35**, 2663-2665 (2010).

Appendix A: A Metastatic Mouse Model of Squamous Cell Carcinoma of the Oral Cavity for Photoacoustic Imaging

A.1 INTRODUCTION

Much of the emerging research of cancer is performed in a preclinical setting on animal models. This allows researchers to investigate new therapeutics, imaging techniques, and genetic pathways without seeking regulatory approval or finding willing volunteers. Mice are commonly used as models for various types of cancer. Tumors are either typically formed through an injection of cancer cells or spontaneously in genetically modified strains of mice.

In order to properly evaluate a new diagnostic or therapeutic technique, the mouse model must accurately represent the human disease. Indeed, simply forming a tumor does not accurately mimic the disease of cancer. Metastases, rather than the primary tumor, are what ultimately lead to a patient's death in most cases. Therefore, accurate mouse models of cancer are incredibly important.

The research presented in this dissertation uses a metastatic mouse model of human squamous cell carcinoma of the oral cavity (SCCOC).¹ This model of SCCOC includes a primary tumor which is inoculated via a submucosal injection in the tongue and micrometastases which form in the cervical lymph nodes located on the neck of the mouse. This well-characterized mouse model has been used for the evaluation of new therapeutics and to study the progression of the disease.²⁻⁴

This chapter describes in detail the procedure for inoculation, imaging, and validation of the model. The purpose of this chapter is to provide enough information so that other researchers can use this powerful model of SCCOC for new contrast agents, imaging procedures, or therapeutic strategies.

A.2 TUMOR INOCULATION AND GROWTH

A large number of diverse cell lines can be used in this mouse model.⁴ In these studies, FaDu cells which were transfected with firefly luciferase (FaDu-Luci) were used. FaDu cells were chosen for their high levels of epidermal growth factor receptor (EGFR) expression and high likelihood to metastasize (70-80%).⁴ However, a different cell line could be used for a different application.

The FaDu-Luci cells were generously supplied by the research group of Dr. Jeffrey Myers at The University of Texas MD Anderson Cancer Center. The cells were cultured in media consisting of 500 mL DMEM media (Sigma), 50 mL of fetal bovine serum (Atlanta Biologicals), and 5 mL of Pen-Strep. The cells were prepared for inoculation by first removing media from the flask and washing the cells once with DPBS without magnesium or calcium. Next, 1 mL of 10% trypsin was added and the cells were returned to the incubator for 5 minutes or until all the cells detached. Then, 9 mL of media was added to the flask to quench the trypsinization and the cells were centrifuged at a speed of 500 rcf for 5 minutes. The supernatant was aspirated out and the cells were resuspended in DPBS at a concentration of approximately 20 million cells per mL.

Female immunodeficient Nu/Nu homozygous mice (Charles River, strain code 88) age 57-70 days were used in this mouse model. Prior to inoculation, the mouse was anesthetized using a mixture of isoflurane (2%) and oxygen (1 L/min). Once the mouse showed no response to a light pinch of the hind foot, the mouse was placed in a supine position. The tongue was extracted from the side of the mouth with a pair of blunt forceps. Care was taken to keep the mouse's nose inside the anesthesia tube and the respiration rate was monitored to look for signs of waking up. It is also important to pull the tongue out of the side of the mouth cutting or puncturing the tongue on the teeth. The tongue was gripped by the forceps on the side of the tongue closest to the teeth and pulled

down towards the mouse's chest. With the other hand, a 30- μ L injection of the as-prepared nanoparticles was made in the side of the tongue that the forceps were not gripping. The injection was made with a 30 gauge needle midway between the tip of the fully extended tongue and the opening of the mouth (approximately 5 mm from the tip of the tongue). The tip of the needle was angled approximately 30° with respect to the tongue and was inserted just below the surface. The injection resulted in noticeable swelling of the tongue. The tongue was carefully placed back inside the mouth with the forceps and the mouse was returned to her cage to recover from the isoflurane.

The tumor was allowed to grow for two to three weeks after the inoculation. The size of the primary tumor was monitored at weekly intervals. The mouse was anesthetized and the tongue was extracted as previously described. The best tumor size seemed to be 3-4 mm in diameter. If it greatly exceeded that size, then the mouse could have trouble eating and contrast agent injections proved difficult.

A.3 ULTRASOUND AND SPECTROSCOPIC PHOTOACOUSTIC IMAGING OF THE CERVICAL LYMPH NODES

Once the tumor reached the appropriate size, photoacoustic (PA) imaging was performed. A Vevo LAZR photoacoustic imaging system (VisualSonics, Inc.) with a LZ-550 256-element linear array transducer (40-MHz center frequency) was used to acquire all images. A thick layer of transparent ultrasound gel (Aquasonic) was used to couple the transducer to the neck of the mouse. The transducer was offset from the surface of the mouse so that the top surface of the skin was located at a depth of approximately 9 mm. This ensured that the light emitted from the transducer converged into the imaging plane at the surface of the skin.

The cervical lymph nodes are located directly beneath the skin on top of the salivary glands. They are easily identified in the ultrasound image as dark oval or bean-

shaped regions. They are located near the bottom-most point of the jaw (which creates a bright signal in the ultrasound image). Photoacoustic imaging can be used to confirm the location of the lymph nodes. The nodes contain a large amount of mostly oxygenated blood. Therefore, if a PA image is acquired at approximately 850 nm, then a strong PA signal should correspond to the dark region in the ultrasound image.

After the “before” images were acquired, the contrast agent was injected peritumorally. The transducer was retracted from the mouse and the mouse’s tongue was extracted as previously described. The injection site was immediately behind the tumor, on the same side of the tongue. Between 30 μ L and 50 μ L of the contrast agent were typically injected. Immediately following the injection, the mouse was repositioned under the transducer and imaging was resumed. The contrast agent was typically delivered to the cervical lymph on the same side as the injection immediately, though drainage kinetics varied from contrast agent to contrast agent. Typically, the time it took for a contrast agent to fully fill the node ranged from 5 minutes (for small molecule dyes) to 3-4 hours (for 120-nm silica coated gold nanoplates). The amount of time that the contrast agent persisted in the node also varied. In the case of the small molecule dyes, the contrast agent was typically cleared from the node in one hour. Silica-coated gold nanoplates, however, persisted in the node for two days or more.

A.4 BIOLUMINESCENCE IMAGING

Bioluminescence imaging proved to be an invaluable tool for confirming the presence of metastases and for guiding lymph node dissection. An IVIS Spectrum optical imaging system (Caliper Life Sciences) was used to collect all bioluminescence images. The FaDu-Luci cells expressed a bioluminescent enzyme, luciferase, which, when exposed to the substrate luciferin, emitted light in the yellow optical range.

Each mouse was anesthetized with Isoflurane (2%). Approximately 100 μ L of Luciferin Rediject (Caliper Life Sciences) was injected in the peritoneal cavity using a 27 guage needle. The bioluminescent signal gradually increased over the course of the next 10-15 minutes. In some of the mice, the metastases were large enough to produce a measureable signal through the skin. For most mice, however, the skin needed to be removed to visualize the lymph node metastases.

The mice were euthanized via an overdose of Isoflurane and cervical dislocation. Incisions were made in the skin in a “T” shape that spanned from shoulder to shoulder to the chin of the mouse. The corner of each skin flap was peeled back with forceps while a scalpel was used to separate soft tissue from the skin. The exposed region contained the cervical lymph nodes and salivary glands. Bioluminescence imaging was again performed with the skin removed to locate micrometastases. Subsequent images were collected during dissection to confirm that the metastases were removed for histology. The tongue, the left cervical node(s), and the right cervical node(s) were each preserved. They were fixed in a buffered solution of formalin for 24-48 hours, then transferred to 70% ethanol. Storage in ethanol for more than a couple weeks is not recommended and the tissue samples should be embedded in paraffin as quickly as possible.

A.5 HISTOLOGICAL VALIDATION

The ability to find micrometastases in the lymph nodes using histology initially proved difficult. The fact that a slide of histology only represents a 5- μ m thick slice of the node means that small metastases are easy to miss. Therefore, in order to reliably locate metastases for histological validation, the entire node must be sampled, and the space between slices must be small enough to capture most metastases.

A hematoxylin and eosin (H&E) stain was used to identify the micrometastases. The paraffin-embedded node was sliced at 100 µm levels, with 5-6 slices acquired at each level. Only a single slice at each level was stained with H&E. The others were left unstained for future immunohistochemistry or optical/photoacoustic microscopy. Metastases typically developed on the edge of the node. They were identified by a disorganized structure, large size, and large nucleus. Once a slice with a metastasis was identified, the other slices at the same level were processed for immunohistochemistry, stained with a silver stain (to detect gold or silver nanoparticles), or were left unstained with the paraffin removed for further imaging.

A.6 REFERENCES

1. Myers, J.N., Holsinger, F.C., Jasser, S.A., Bekele, B.N. & Fidler, I.J. An Orthotopic Nude Mouse Model of Oral Tongue Squamous Cell Carcinoma. *Clinical Cancer Research* **8**, 293-298 (2002).
2. Sano, D. et al. The effect of combination anti-endothelial growth factor receptor and anti-vascular endothelial growth factor receptor 2 targeted therapy on lymph node metastasis: a study in an orthotopic nude mouse model of squamous cell carcinoma of the oral tongue. *Archives of Otolaryngology—Head & Neck Surgery* **135**, 411 (2009).
3. Younes, M.N. et al. Concomitant inhibition of epidermal growth factor and vascular endothelial growth factor receptor tyrosine kinases reduces growth and metastasis of human salivary adenoid cystic carcinoma in an orthotopic nude mouse model. *Molecular cancer therapeutics* **5**, 2696-2705 (2006).
4. Sano, D. et al. Disruptive TP53 mutation is associated with aggressive disease characteristics in an orthotopic murine model of oral tongue cancer. *Clinical Cancer Research* **17**, 6658-6670 (2011).

References

1. Hanahan, D. & Weinberg, R.A. The hallmarks of cancer. *cell* **100**, 57-70 (2000).
2. Hanahan, D. & Weinberg, R.A. Hallmarks of cancer: the next generation. *Cell* **144**, 646-674 (2011).
3. Weissleder, R. Molecular imaging in cancer. *Science* **312**, 1168-1171 (2006).
4. Weissleder, R. & Ntziachristos, V. Shedding light onto live molecular targets. *Nature medicine* **9**, 123-128 (2003).
5. Gambhir, S.S. Molecular imaging of cancer with positron emission tomography. *Nat Rev Cancer* **2**, 683-693 (2002).
6. Kaufmann, B.A. & Lindner, J.R. Molecular imaging with targeted contrast ultrasound. *Current opinion in biotechnology* **18**, 11-16 (2007).
7. Mallidi, S., Luke, G.P. & Emelianov, S. Photoacoustic imaging in cancer detection, diagnosis, and treatment guidance. *Trends in Biotechnology* **29**, 213-221 (2011).
8. Harris, A.L. Hypoxia - a key regulatory factor in tumour growth. *Nat Rev Cancer* **2**, 38-47 (2002).
9. Shepp, L.A. & Vardi, Y. Maximum likelihood reconstruction for emission tomography. *Medical Imaging, IEEE Transactions on* **1**, 113-122 (1982).
10. Jaszczak, R.J., Greer, K.L., Floyd Jr, C.E., Harris, C.C. & Coleman, R.E. Improved SPECT quantification using compensation for scattered photons. *Journal of nuclear medicine: official publication, Society of Nuclear Medicine* **25**, 893-900 (1984).
11. Gambhir, S.S. et al. A tabulated summary of the FDG PET literature. *Journal of nuclear medicine* **42**, 1S-93S (2001).
12. Warburg, O. On the origin of cancer cells. *Science* **123**, 309-314 (1956).
13. Been, L.B. et al. [18F] FLT-PET in oncology: current status and opportunities. *European journal of nuclear medicine and molecular imaging* **31**, 1659-1672 (2004).

14. Beheshti, M. et al. Detection of bone metastases in patients with prostate cancer by ¹⁸F fluorocholine and ¹⁸F fluoride PET–CT: a comparative study. *European journal of nuclear medicine and molecular imaging* **35**, 1766-1774 (2008).
15. Koh, W.-J. et al. Imaging of hypoxia in human tumors with [F-18] fluoromisonidazole. *International Journal of Radiation Oncology* Biology* Physics* **22**, 199-212 (1992).
16. Wester, H.-J. Nuclear imaging probes: from bench to bedside. *Clinical cancer research* **13**, 3470-3481 (2007).
17. Jaffer, F.A. & Weissleder, R. Molecular imaging in the clinical arena. *JAMA: the journal of the American Medical Association* **293**, 855-862 (2005).
18. Lauterbur, P.C. Image Formation by Induced Local Interactions - Examples Employing Nuclear Magnetic-Resonance. *Nature* **242**, 190-191 (1973).
19. Meaney, J.F. et al. Diagnosis of pulmonary embolism with magnetic resonance angiography. *New England Journal of Medicine* **336**, 1422-1427 (1997).
20. Sipkins, D.A. et al. Detection of tumor angiogenesis in vivo by $\alpha v\beta 3$ -targeted magnetic resonance imaging. *Nature medicine* **4**, 623-626 (1998).
21. Pearlman, J.D. et al. Magnetic resonance mapping demonstrates benefits of VEGF–induced myocardial angiogenesis. *Nature medicine* **1**, 1085-1089 (1995).
22. Suwa, T., Ozawa, S., Ueda, M., Ando, N. & Kitajima, M. Magnetic resonance imaging of esophageal squamous cell carcinoma using magnetite particles coated with anti-epidermal growth factor receptor antibody. *International Journal of Cancer* **75**, 626-634 (1998).
23. Daldrup-Link, H.E. et al. In vivo tracking of genetically engineered, anti-HER2/neu directed natural killer cells to HER2/neu positive mammary tumors with magnetic resonance imaging. *European radiology* **15**, 4-13 (2005).
24. Ntziachristos, V., Ripoll, J., Wang, L.V. & Weissleder, R. Looking and listening to light: the evolution of whole-body photonic imaging. *Nature biotechnology* **23**, 313-320 (2005).
25. Kim, S. et al. Near-infrared fluorescent type II quantum dots for sentinel lymph node mapping. *Nat Biotechnol* **22**, 93-97 (2004).
26. Montet, X. et al. Tomographic fluorescence imaging of tumor vascular volume in mice¹. *Radiology* **242**, 751-758 (2007).

27. Wang, L., Jacques, S.L. & Zheng, L. MCML--Monte Carlo modeling of light transport in multi-layered tissues. *Computer methods and programs in biomedicine* **47**, 131-146 (1995).
28. Ntziachristos, V., Bremer, C. & Weissleder, R. Fluorescence imaging with near-infrared light: new technological advances that enable in vivo molecular imaging. *European radiology* **13**, 195-208 (2003).
29. Mansfield, J.R., Gossage, K.W., Hoyt, C.C. & Levenson, R.M. Autofluorescence removal, multiplexing, and automated analysis methods for in-vivo fluorescence imaging. *Journal of biomedical optics* **10**, 041207-041207-041209 (2005).
30. Patterson, G.H. & Piston, D.W. Photobleaching in two-photon excitation microscopy. *Biophysical journal* **78**, 2159-2162 (2000).
31. Chan, W.C. & Nie, S. Quantum dot bioconjugates for ultrasensitive nonisotopic detection. *Science* **281**, 2016-2018 (1998).
32. Wu, X. et al. Immunofluorescent labeling of cancer marker Her2 and other cellular targets with semiconductor quantum dots. *Nature biotechnology* **21**, 41-46 (2002).
33. Chan, W.C. et al. Luminescent quantum dots for multiplexed biological detection and imaging. *Current opinion in biotechnology* **13**, 40-46 (2002).
34. Ferrara, K., Pollard, R. & Borden, M. Ultrasound microbubble contrast agents: fundamentals and application to gene and drug delivery. *Annu Rev Biomed Eng* **9**, 415-447 (2007).
35. Kripfgans, O.D., Fowlkes, J.B., Miller, D.L., Eldevik, O.P. & Carson, P.L. Acoustic droplet vaporization for therapeutic and diagnostic applications. *Ultrasound Med Biol* **26**, 1177-1189 (2000).
36. Wilson, K., Homan, K. & Emelianov, S. Biomedical photoacoustics beyond thermal expansion using triggered nanodroplet vaporization for contrast-enhanced imaging. *Nat Commun* **3**, 618 (2012).
37. Needles, A. et al. Nonlinear contrast imaging with an array-based micro-ultrasound system. *Ultrasound Med Biol* **36**, 2097-2106 (2010).
38. Bell, A.G. Upon the production of sound by radiant energy. *Philosophical Magazine Series 5* **11**, 510-528 (1881).
39. Wang, L.V. Photoacoustic Imaging and Spectroscopy, Edn. 1. (CRC Press, 2009).

40. Xu, M. & Wang, L.V. Photoacoustic imaging in biomedicine. *Review of Scientific Instruments* **77**, 041101 (2006).
41. Chen, Y.-S., Frey, W., Aglyamov, S. & Emelianov, S. Environment-Dependent Generation of Photoacoustic Waves from Plasmonic Nanoparticles. *Small* **8**, 47-52 (2012).
42. Shah, J., Aglyamov, S.R., Sokolov, K., Milner, T.E. & Emelianov, S.Y. Ultrasound imaging to monitor photothermal therapy - Feasibility study. *Optics Express* **16**, 3776-3785 (2008).
43. Kim, S. et al. in Ultrasonics Symposium (IUS), 2010 IEEE 233-236 (2010).
44. Chen, Y.S., Frey, W., Walker, C., Aglyamov, S. & Emelianov, S. Sensitivity enhanced nanothermal sensors for photoacoustic temperature mapping. *Journal of biophotonics* (2013).
45. Cox, B., Laufer, J.G., Arridge, S.R. & Beard, P.C. Quantitative spectroscopic photoacoustic imaging: a review. *J Biomed Opt* **17**, 061202 (2012).
46. Cook, J.R., Frey, W. & Emelianov, S. Quantitative Photoacoustic Imaging of Nanoparticles in Cells and Tissues. *ACS nano* (2013).
47. Kim, S., Chen, Y.-S., Luke, G.P. & Emelianov, S.Y. In vivo three-dimensional spectroscopic photoacoustic imaging for monitoring nanoparticle delivery. *Biomed. Opt. Express* **2**, 2540-2550 (2011).
48. Wang, X., Xie, X., Ku, G., Wang, L.V. & Stoica, G. Noninvasive imaging of hemoglobin concentration and oxygenation in the rat brain using high-resolution photoacoustic tomography. *J Biomed Opt* **11**, 024015 (2006).
49. Levi, J. et al. Molecular Photoacoustic Imaging of Follicular Thyroid Carcinoma. *Clinical Cancer Research* **19**, 1494-1502 (2013).
50. Kim, C. et al. In Vivo Molecular Photoacoustic Tomography of Melanomas Targeted by Bioconjugated Gold Nanocages. *ACS Nano* **4**, 4559-4564 (2010).
51. Penrose, R. & Todd, J.A. On best approximate solutions of linear matrix equations. *Mathematical Proceedings of the Cambridge Philosophical Society* **52**, 17-19 (1956).
52. Li, M.-L. et al. Simultaneous Molecular and Hypoxia Imaging of Brain Tumors In Vivo Using Spectroscopic Photoacoustic Tomography. *Anglais* **96** (2008).

53. Keshava, N. & Mustard, J.F. Spectral unmixing. *Ieee Signal Proc Mag* **19**, 44-57 (2002).
54. Luke, G.P., Yeager, D. & Emelianov, S.Y. Biomedical applications of photoacoustic imaging with exogenous contrast agents. *Ann Biomed Eng* **40**, 422-437 (2012).
55. de la Zerda, A. et al. Ultrahigh sensitivity carbon nanotube agents for photoacoustic molecular imaging in living mice. *Nano Lett* **10**, 2168-2172 (2010).
56. De la Zerda, A. et al. Carbon nanotubes as photoacoustic molecular imaging agents in living mice. *Nat Nanotechnol* **3**, 557-562 (2008).
57. Kim, G. et al. Indocyanine-green-embedded PEBBLEs as a contrast agent for photoacoustic imaging. *J Biomed Opt* **12**, 044020 (2007).
58. Buehler, A., Herzog, E., Razansky, D. & Ntziachristos, V. Video rate optoacoustic tomography of mouse kidney perfusion. *Opt Lett* **35**, 2475-2477 (2010).
59. Taruttis, A., Herzog, E., Razansky, D. & Ntziachristos, V. Real-time imaging of cardiovascular dynamics and circulating gold nanorods with multispectral optoacoustic tomography. *Opt Express* **18**, 19592-19602 (2010).
60. Homan, K. et al. Silver nanosystems for photoacoustic imaging and image-guided therapy. *Journal of Biomedical Optics* **15**, 021316 (2010).
61. Homan, K.A. et al. Silver Nanoplate Contrast Agents for in Vivo Molecular Photoacoustic Imaging. *ACS Nano* **6**, 641-650 (2012).
62. Wang, Y. et al. Photoacoustic Tomography of a Nanoshell Contrast Agent in the in Vivo Rat Brain. *Nano Letters* **4**, 1689-1692 (2004).
63. Bayer, C.L., Luke, G.P. & Emelianov, S.Y. Photoacoustic Imaging for Medical Diagnostics. *Acoustics Today* **8**, 15-23 (2012).
64. Cai, X. et al. In vivo quantitative evaluation of the transport kinetics of gold nanocages in a lymphatic system by noninvasive photoacoustic tomography. *ACS Nano* **5**, 9658-9667 (2011).
65. Pan, D. et al. Near infrared photoacoustic detection of sentinel lymph nodes with gold nanobeacons. *Biomaterials* **31**, 4088-4093 (2010).

66. Song, K.H., Kim, C., Cobley, C.M., Xia, Y. & Wang, L.V. Near-Infrared Gold Nanocages as a New Class of Tracers for Photoacoustic Sentinel Lymph Node Mapping on a Rat Model. *Nano Letters* **9**, 183-188 (2008).
67. Song, K.H., Kim, C., Maslov, K. & Wang, L.V. Noninvasive in vivo spectroscopic nanorod-contrast photoacoustic mapping of sentinel lymph nodes. *European Journal of Radiology* **70**, 227-231 (2009).
68. Song, K.H., Stein, E.W., Margenthaler, J.A. & Wang, L.V. Noninvasive photoacoustic identification of sentinel lymph nodes containing methylene blue in vivo in a rat model. *Journal of Biomedical Optics* **13**, 054033-054036 (2008).
69. Razansky, D. et al. Multispectral Optoacoustic Tomography of Matrix Metalloproteinase Activity in Vulnerable Human Carotid Plaques. *Molecular Imaging and Biology*, 1-9 (2011).
70. Jain, P.K., Lee, K.S., El-Sayed, I.H. & El-Sayed, M.A. Calculated Absorption and Scattering Properties of Gold Nanoparticles of Different Size, Shape, and Composition: Applications in Biological Imaging and Biomedicine. *The Journal of Physical Chemistry B* **110**, 7238-7248 (2006).
71. Nikoobakht, B. & El-Sayed, M.A. Preparation and growth mechanism of gold nanorods (NRs) using seed-mediated growth method. *Chemistry of Materials* **15**, 1957-1962 (2003).
72. Niidome, T. et al. PEG-modified gold nanorods with a stealth character for in vivo applications. *Journal of Controlled Release* **114**, 343-347 (2006).
73. Kumar, S., Aaron, J. & Sokolov, K. Directional conjugation of antibodies to nanoparticles for synthesis of multiplexed optical contrast agents with both delivery and targeting moieties. *Nature Protocols* **3**, 314-320 (2008).
74. Longmire, M., Choyke, P.L. & Kobayashi, H. Clearance properties of nano-sized particles and molecules as imaging agents: considerations and caveats. *Nanomedicine* **3**, 703-717 (2008).
75. Connor, E.E., Mwamuka, J., Gole, A., Murphy, C.J. & Wyatt, M.D. Gold nanoparticles are taken up by human cells but do not cause acute cytotoxicity. *Small* **1**, 325-327 (2005).
76. Nicholson, R.I., Gee, J.M. & Harper, M.E. EGFR and cancer prognosis. *Eur J Cancer* **37 Suppl 4**, S9-15 (2001).

77. Menard, S., Tagliabue, E., Campiglio, M. & Pupa, S.M. Role of HER2 gene overexpression in breast carcinoma. *Journal of cellular physiology* **182**, 150-162 (2000).
78. Dassonville, O. et al. Expression of epidermal growth factor receptor and survival in upper aerodigestive tract cancer. *Journal of Clinical Oncology* **11**, 1873-1878 (1993).
79. Pritchard, K.I. et al. HER2 and responsiveness of breast cancer to adjuvant chemotherapy. *New England Journal of Medicine* **354**, 2103-2111 (2006).
80. Bonner, J.A. et al. Radiotherapy plus cetuximab for squamous-cell carcinoma of the head and neck. *New England Journal of Medicine* **354**, 567-578 (2006).
81. Vogel, C.L. et al. Efficacy and safety of trastuzumab as a single agent in first-line treatment of HER2-overexpressing metastatic breast cancer. *Journal of Clinical Oncology* **20**, 719-726 (2002).
82. Mallidi, S., Larson, T., Aaron, J., Sokolov, K. & Emelianov, S. Molecular specific optoacoustic imaging with plasmonic nanoparticles. *Opt Express* **15**, 6583-6588 (2007).
83. Mallidi, S. et al. Multiwavelength Photoacoustic Imaging and Plasmon Resonance Coupling of Gold Nanoparticles for Selective Detection of Cancer. *Nano Letters* **9**, 2825-2831 (2009).
84. Aaron, J. et al. Plasmon resonance coupling of metal nanoparticles for molecular imaging of carcinogenesis in vivo. *J Biomed Opt* **12**, 034007 (2007).
85. Aaron, J., Travis, K., Harrison, N. & Sokolov, K. Dynamic imaging of molecular assemblies in live cells based on nanoparticle plasmon resonance coupling. *Nano Lett* **9**, 3612-3618 (2009).
86. Aaron, J.S. et al. Increased optical contrast in imaging of epidermal growth factor receptor using magnetically actuated hybrid gold/iron oxide nanoparticles. *Optics Express* **14**, 12930-12943 (2006).
87. Sokolov, K. et al. Real-Time Vital Optical Imaging of Precancer Using Anti-Epidermal Growth Factor Receptor Antibodies Conjugated to Gold Nanoparticles. *Cancer Research* **63**, 1999-2004 (2003).
88. Li, P.C. et al. In vivo Photoacoustic Molecular Imaging with Simultaneous Multiple Selective Targeting Using Antibody-Conjugated Gold Nanorods. *Optics Express* **16**, 18605-18615 (2008).

89. Gleysteen, J.P. et al. Fluorescent labeled anti-EGFR antibody for identification of regional and distant metastasis in a preclinical xenograft model. *Head Neck* **30**, 782-789 (2008).
90. Kramer-Marek, G., Kiesewetter, D.O. & Capala, J. Changes in HER2 expression in breast cancer xenografts after therapy can be quantified using PET and (18)F-labeled affibody molecules. *Journal of Nuclear Medicine* **50**, 1131-1139 (2009).
91. Li, P.-C. et al., Vol. 6086. (eds. A.O. Alexander & V.W. Lihong) 60860M (SPIE, 2006).
92. Shah, C. et al. Imaging biomarkers predict response to anti-HER2 (ErbB2) therapy in preclinical models of breast cancer. *Clinical Cancer Research* **15**, 4712-4721 (2009).
93. Chen, T.-J. et al. Targeted herceptin–dextran iron oxide nanoparticles for noninvasive imaging of HER2/neu receptors using MRI. *JBIC Journal of Biological Inorganic Chemistry* **14**, 253-260 (2009).
94. Abe, O. et al. Tamoxifen for early breast cancer: an overview of the randomised trials. *Lancet* **351**, 1451-1467 (1998).
95. Reddy, J.A. & Low, P.S. Folate-mediated targeting of therapeutic and imaging agents to cancers. *Critical Reviews™ in Therapeutic Drug Carrier Systems* **15** (1998).
96. Posey, J.A. et al. A pilot trial of Vitaxin, a humanized anti-vitronectin receptor (anti $\alpha v \beta 3$) antibody in patients with metastatic cancer. *Cancer Biotherapy and Radiopharmaceuticals* **16**, 125-132 (2001).
97. Hurwitz, H. et al. Bevacizumab plus irinotecan, fluorouracil, and leucovorin for metastatic colorectal cancer. *New England journal of medicine* **350**, 2335-2342 (2004).
98. Mintun, M. et al. Breast cancer: PET imaging of estrogen receptors. *Radiology* **169**, 45-48 (1988).
99. Ciana, P. et al. In vivo imaging of transcriptionally active estrogen receptors. *Nature medicine* **9**, 82-86 (2002).
100. Chen, W.-T., Khazaie, K., Zhang, G., Weissleder, R. & Tung, C.-H. Detection of dysplastic intestinal adenomas using a fluorescent folate imaging probe. *Molecular Imaging* **4**, 67 (2005).

101. Choi, H., Choi, S.R., Zhou, R., Kung, H.F. & Chen, I. Iron oxide nanoparticles as magnetic resonance contrast agent for tumor imaging via folate receptor-targeted delivery. *Academic radiology* **11**, 996-1004 (2004).
102. Backer, M.V. et al. Molecular imaging of VEGF receptors in angiogenic vasculature with single-chain VEGF-based probes. *Nature medicine* **13**, 504-509 (2007).
103. Nagengast, W.B. et al. In vivo VEGF imaging with radiolabeled bevacizumab in a human ovarian tumor xenograft. *Journal of Nuclear Medicine* **48**, 1313-1319 (2007).
104. Savariar, E.N. et al. Real-time In Vivo Molecular Detection of Primary Tumors and Metastases with Ratiometric Activatable Cell-Penetrating Peptides. *Cancer research* **73**, 855-864 (2013).
105. Egeblad, M. & Werb, Z. New functions for the matrix metalloproteinases in cancer progression. *Nat Rev Cancer* **2**, 161-174 (2002).
106. Fingleton, B. in *Seminars in cell & developmental biology*, Vol. 19 61-68 (Elsevier, 2008).
107. Levi, J. et al. Design, Synthesis, and Imaging of an Activatable Photoacoustic Probe. *Journal of the American Chemical Society* **132**, 11264-11269 (2010).
108. Ajisaka, H., Yonemura, Y. & Miwa, K. Correlation of lymph node metastases and expression of matrix metalloproteinase-7 in patients with gastric cancer. *Hepatology* **51**, 900-905 (2004).
109. Daniele, A. et al. Expression of Metalloproteinases MMP-2 and MMP-9 in Sentinel Lymph Node and Serum of Patients with Metastatic and Non-Metastatic Breast Cancer. *Anticancer Research* **30**, 3521-3527 (2010).
110. Kurahara, S. et al. Expression of MMPS, MT-MMP, and TIMPs in squamous cell carcinoma of the oral cavity: correlations with tumor invasion and metastasis. *Head Neck* **21**, 627-638 (1999).
111. Zhang, J., Yang, P.L. & Gray, N.S. Targeting cancer with small molecule kinase inhibitors. *Nature Reviews Cancer* **9**, 28-39 (2009).
112. Lievre, A. et al. KRAS mutation status is predictive of response to cetuximab therapy in colorectal cancer. *Cancer research* **66**, 3992-3995 (2006).
113. Wang, Y. et al. Visualizing the mechanical activation of Src. *Nature* **434**, 1040-1045 (2005).

114. Sugahara, K.N. et al. Coadministration of a tumor-penetrating peptide enhances the efficacy of cancer drugs. *science* **328**, 1031-1035 (2010).
115. Mehlen, P. & Puisieux, A. Metastasis: a question of life or death. *Nature Reviews Cancer* **6**, 449-458 (2006).
116. , Vol. 2013 (National Cancer Institute, www.cancer.gov/cancertopics/factsheet/detection/staging).
117. Cochran, A.J., Roberts, A.A. & Saida, T. The place of lymphatic mapping and sentinel node biopsy in oncology. *International journal of clinical oncology* **8**, 139-150 (2003).
118. Stoeckli, S.J., Steinert, H., Pfaltz, M. & Schmid, S. Sentinel Lymph Node Evaluation in Squamous Cell Carcinoma of the Head and Neck. *Otolaryngology - Head and Neck Surgery* **125**, 221-226 (2001).
119. Veronesi, U. et al. Sentinel-node biopsy to avoid axillary dissection in breast cancer with clinically negative lymph-nodes. *Lancet* **349**, 1864-1867 (1997).
120. Gershenwald, J.E. et al. Multi-Institutional Melanoma Lymphatic Mapping Experience: The Prognostic Value of Sentinel Lymph Node Status in 612 Stage I or II Melanoma Patients. *Journal of Clinical Oncology* **17**, 976 (1999).
121. Goldberg, J., Riedel, E., Morrow, M. & Van Zee, K. Morbidity of Sentinel Node Biopsy: Relationship Between Number of Excised Lymph Nodes and Patient Perceptions of Lymphedema. *Annals of Surgical Oncology* **18**, 2866-2872 (2011).
122. Langer, I. et al. Morbidity of Sentinel Lymph Node Biopsy (SLN) Alone Versus SLN and Completion Axillary Lymph Node Dissection After Breast Cancer Surgery: A Prospective Swiss Multicenter Study on 659 Patients. *Annals of Surgery* **245**, 452-461 (2007).
123. Scoggins, C.R. et al. Factors associated with false-negative sentinel lymph node biopsy in melanoma patients. *Annals of surgical oncology* **17**, 709-717 (2010).
124. Cohen, S.M., Fishinghawk, B.G. & Cohen, M.S. Translational imaging of lymphatics in cancer. *Advanced Drug Delivery Reviews* **63**, 956-962 (2011).
125. Wunderbaldinger, P. Problems and prospects of modern lymph node imaging. *European Journal of Radiology* **58**, 325-337 (2006).
126. Kobayashi, H. et al. Lymphatic drainage imaging of breast cancer in mice by micro-magnetic resonance lymphangiography using a nano-size paramagnetic contrast agent. *Journal of the National Cancer Institute* **96**, 703-708 (2004).

127. Goldberg, B.B. et al. Sentinel Lymph Nodes in a Swine Model with Melanoma: Contrast-enhanced Lymphatic US1. *Radiology* **230**, 727-734 (2004).
128. Oh, M.H. et al. Large-scale synthesis of bioinert tantalum oxide nanoparticles for X-ray computed tomography imaging and bimodal image-guided sentinel lymph node mapping. *Journal of the American Chemical Society* **133**, 5508-5515 (2011).
129. Richards, P.S. & Peacock, T.E. The role of ultrasound in the detection of cervical lymph node metastases in clinically N0 squamous cell carcinoma of the head and neck. *Cancer Imaging* **7**, 167-178 (2007).
130. Wagner, J.D. et al. FDG-PET sensitivity for melanoma lymph node metastases is dependent on tumor volume. *Journal of surgical oncology* **77**, 237-242 (2001).
131. Kyzas, P.A., Evangelou, E., Denaxa-Kyza, D. & Ioannidis, J.P. 18F-fluorodeoxyglucose positron emission tomography to evaluate cervical node metastases in patients with head and neck squamous cell carcinoma: a meta-analysis. *Journal of the National Cancer Institute* **100**, 712-720 (2008).
132. Harisinghani, M.G. et al. Noninvasive detection of clinically occult lymph-node metastases in prostate cancer. *New England Journal of Medicine* **348**, 2491-2499 (2003).
133. Sleeman, J. & Steeg, P.S. Cancer metastasis as a therapeutic target. *European Journal of Cancer* **46**, 1177-1180 (2010).
134. Bergkvist, L. & Frisell, J. Multicentre validation study of sentinel node biopsy for staging in breast cancer. *British Journal of Surgery* **92**, 1221-1224 (2005).
135. Morton, D.L. et al. Sentinel-node biopsy or nodal observation in melanoma. *New England Journal of Medicine* **355**, 1307-1317 (2006).
136. Gershenwald, J.E. et al. Patterns of recurrence following a negative sentinel lymph node biopsy in 243 patients with stage I or II melanoma. *Journal of clinical oncology* **16**, 2253-2260 (1998).
137. Myers, J.N., Holsinger, F.C., Jasser, S.A., Bekele, B.N. & Fidler, I.J. An Orthotopic Nude Mouse Model of Oral Tongue Squamous Cell Carcinoma. *Clinical Cancer Research* **8**, 293-298 (2002).
138. Prah, S. (Oregon Medical Laser Center, 2011).
139. Vander Heiden, M.G., Cantley, L.C. & Thompson, C.B. Understanding the Warburg effect: the metabolic requirements of cell proliferation. *Science* **324**, 1029-1033 (2009).

140. Ronka, R. et al. The impact of sentinel node biopsy and axillary staging strategy on hospital costs. *Annals of oncology : official journal of the European Society for Medical Oncology / ESMO* **15**, 88-94 (2004).
141. Van der Hoeven, J.J.M., Hoekstra, O.S., Comans, E.F.I. & al., e. Determinants of diagnostic performance of [F-18]Fluorodeoxyglucose positron emission tomography for axillary staging in breast cancer. *Ann Surg* **236**, 619-624 (2002).
142. Zhang, H.F., Maslov, K., Stoica, G. & Wang, L.V. Functional photoacoustic microscopy for high-resolution and noninvasive in vivo imaging. *Nat Biotech* **24**, 848-851 (2006).
143. Eghtedari, M. et al. High sensitivity of in vivo detection of gold nanorods using a laser optoacoustic imaging system. *Nano Lett* **7**, 1914-1918 (2007).
144. Diebold, G.J., Khan, M.I. & Park, S.M. Photoacoustic "signatures" of particulate matter: optical production of acoustic monopole radiation. *Science* **250**, 101-104 (1990).
145. Wang, L.V. & Hu, S. Photoacoustic tomography: in vivo imaging from organelles to organs. *Science* **335**, 1458-1462 (2012).
146. Beard, P. Biomedical photoacoustic imaging. *Interface Focus* **1**, 602-631 (2011).
147. Khlebtsov, N. & Dykman, L. Biodistribution and toxicity of engineered gold nanoparticles: a review of in vitro and in vivo studies. *Chemical Society Reviews* **40**, 1647-1671 (2011).
148. Lee, J.-H. et al. Artificially engineered magnetic nanoparticles for ultra-sensitive molecular imaging. *Nature medicine* **13**, 95-99 (2006).
149. Maeda, H. The enhanced permeability and retention (EPR) effect in tumor vasculature : The key role of tumor-selective macromolecular drug targeting. *Adv. Enzyme Regul.* **41**, 189-207 (2001).
150. Massoud, T.F. & Gambhir, S.S. Molecular imaging in living subjects: seeing fundamental biological processes in a new light. *Genes & development* **17**, 545-580 (2003).
151. Jares-Erijman, E.A. & Jovin, T.M. FRET imaging. *Nature biotechnology* **21**, 1387-1395 (2003).
152. Luke, G., Yeager, D. & Emelianov, S. Biomedical Applications of Photoacoustic Imaging with Exogenous Contrast Agents. *Annals of Biomedical Engineering*, 1-16 (2011).

153. Emelianov, S.Y., Li, P.-C. & O'Donnell, M. Photoacoustics for molecular imaging and therapy. *Physics Today*, 34-39 (2008).
154. Stuckensen, T., Kovács, A.F., Adams, S. & Baum, R.P. Staging of the neck in patients with oral cavity squamous cell carcinomas: a prospective comparison of PET, ultrasound, CT and MRI. *Journal of Cranio-Maxillofacial Surgery* **28**, 319-324 (2000).
155. Kruger, R.A., Kiser, W.L., Reinecke, D.R. & Kruger, G.A. Thermoacoustic computed tomography using a conventional linear transducer array. *Medical Physics* **30**, 856-860 (2003).
156. Oraevsky, A.A., Jacques, S.L., Esenaliev, R.O. & Tittel, F.K., Vol. 2134 122 (1994).
157. Wang, X. et al. Noninvasive laser-induced photoacoustic tomography for structural and functional in vivo imaging of the brain. *Nature biotechnology* **21**, 803-806 (2003).
158. Hu, S. & Wang, L.V. Photoacoustic imaging and characterization of the microvasculature. *Journal of Biomedical Optics* **15**, 011101-011115 (2010).
159. Oh, J.-T. et al. Three-dimensional imaging of skin melanoma in vivo by dual-wavelength photoacoustic microscopy. *Journal of Biomedical Optics* **11**, 034032-034034 (2006).
160. Wang, B. et al. Detection of lipid in atherosclerotic vessels using ultrasound-guided spectroscopic intravascular photoacoustic imaging. *Opt. Express* **18**, 4889-4897 (2010).
161. Karpouk, A.B., Wang, B., Amirian, J., Smalling, R.W. & Emelianov, S.Y. Feasibility of in vivo intravascular photoacoustic imaging using integrated ultrasound and photoacoustic imaging catheter. *Journal of Biomedical Optics* **17**, 1 (2012).
162. Wang, B. et al. In vivo intravascular ultrasound-guided photoacoustic imaging of lipid in plaques using an animal model of atherosclerosis. *Ultrasound in Medicine and Biology* **accepted** (2012).
163. Jose, J., Manohar, S., Kolkman, R.G.M., Steenbergen, W. & van Leeuwen, T.G. Imaging of tumor vasculature using Twente photoacoustic systems. *Journal of Biophotonics* **2**, 701-717 (2009).

164. Sethuraman, S., Amirian, J.H., Litovsky, S.H., Smalling, R.W. & Emelianov, S.Y. Spectroscopic intravascular photoacoustic imaging to differentiate atherosclerotic plaques. *Opt Express* **16**, 3362-3367 (2008).
165. Guo, Z., Xu, Z. & Wang, L.V. Dependence of photoacoustic speckles on boundary roughness. *Journal of biomedical optics* **17**, 0460091-0460096 (2012).
166. Holzer, W. et al. Photostability and thermal stability of indocyanine green. *Journal of Photochemistry and Photobiology B: Biology* **47**, 155-164 (1998).
167. Luke, G.P., Nam, S.Y. & Emelianov, S.Y. Optical wavelength selection for improved spectroscopic photoacoustic imaging. *Photoacoustics* **1**, 36-42 (2013).
168. Xiao, J., Yuan, Z., He, J. & Jiang, H. Quantitative multispectral photoacoustic tomography and wavelength optimization. *Journal of X-ray science and technology* **18**, 415-427 (2010).
169. Bayer, C.L., Nam, S.Y., Chen, Y.-S. & Emelianov, S.Y. Photoacoustic signal amplification through plasmonic nanoparticle aggregation. *Journal of biomedical optics* **18**, 016001-016001 (2013).
170. Nam, S.Y., Ricles, L.M., Suggs, L.J. & Emelianov, S.Y. Nonlinear photoacoustic signal increase from endocytosis of gold nanoparticles. *Optics letters* **37**, 4708-4710 (2012).
171. Danielli, A., Maslov, K., Xia, J. & Wang, L.V. in Proc. of SPIE Vol, Vol. 8223 82233H-82231 (2012).
172. Homan, K. et al. Prospects of molecular photoacoustic imaging at 1064 nm wavelength. *Opt Lett* **35**, 2663-2665 (2010).
173. Mao, Y.P. et al. The N staging system in nasopharyngeal carcinoma with radiation therapy oncology group guidelines for lymph node levels based on magnetic resonance imaging. *Clinical cancer research* **14**, 7497-7503 (2008).
174. Hu, S., Maslov, K., Tsytsarev, V. & Wang, L.V. Functional transcranial brain imaging by optical-resolution photoacoustic microscopy, Vol. 14. (SPIE, 2009).
175. Wang, L.V. Multiscale photoacoustic microscopy and computed tomography. *Nat Photonics* **3**, 503-509 (2009).
176. Hu, M. et al. Gold nanostructures: engineering their plasmonic properties for biomedical applications. *Chemical Society Reviews* **35**, 1084-1094 (2006).

177. Bao, C. et al. Gold Nanoprisms as Optoacoustic Signal Nanoamplifiers for In Vivo Bioimaging of Gastrointestinal Cancers. *Small* **9**, 68-74 (2013).
178. Ha, T.H., Koo, H.-J. & Chung, B.H. Shape-Controlled Syntheses of Gold Nanoprisms and Nanorods Influenced by Specific Adsorption of Halide Ions. *The Journal of Physical Chemistry C* **111**, 1123-1130 (2006).
179. Ha, T.H., Kim, Y.J. & Park, S.H. Complete separation of triangular gold nanoplates through selective precipitation under CTAB micelles in aqueous solution. *Chemical Communications* **46**, 3164-3166 (2010).
180. Stöber, W., Fink, A. & Bohn, E. Controlled growth of monodisperse silica spheres in the micron size range. *Journal of Colloid and Interface Science* **26**, 62-69 (1968).
181. Chen, Y.S. et al. Enhanced thermal stability of silica-coated gold nanorods for photoacoustic imaging and image-guided therapy. *Opt Express* **18**, 8867-8878 (2010).
182. Chen, Y.-S. et al. Silica-coated gold nanorods as photoacoustic signal nanoamplifiers. *Nano letters* **11**, 348-354 (2011).
183. Gerlinger, M. et al. Intratumor heterogeneity and branched evolution revealed by multiregion sequencing. *New England Journal of Medicine* **366**, 883-892 (2012).
184. Manohar, S. et al. Initial results of in vivo non-invasive cancer imaging in the human breast using near-infrared photoacoustics. *Opt. Express* **15**, 12277-12285 (2007).
185. Kennedy, L.C. et al. A New Era for Cancer Treatment: Gold-Nanoparticle-Mediated Thermal Therapies. *Small* **7**, 169-183 (2011).
186. Sano, D. et al. The effect of combination anti-endothelial growth factor receptor and anti-vascular endothelial growth factor receptor 2 targeted therapy on lymph node metastasis: a study in an orthotopic nude mouse model of squamous cell carcinoma of the oral tongue. *Archives of Otolaryngology—Head & Neck Surgery* **135**, 411 (2009).
187. Younes, M.N. et al. Concomitant inhibition of epidermal growth factor and vascular endothelial growth factor receptor tyrosine kinases reduces growth and metastasis of human salivary adenoid cystic carcinoma in an orthotopic nude mouse model. *Molecular cancer therapeutics* **5**, 2696-2705 (2006).

188. Sano, D. et al. Disruptive TP53 mutation is associated with aggressive disease characteristics in an orthotopic murine model of oral tongue cancer. *Clinical Cancer Research* **17**, 6658-6670 (2011).